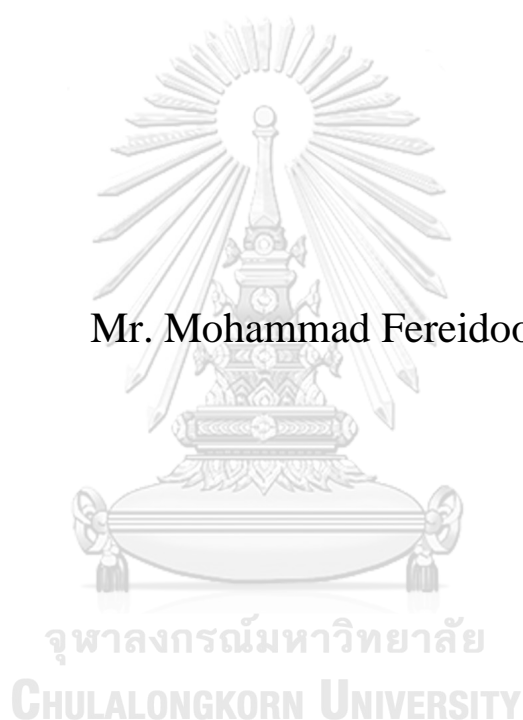


Photocatalytic films for efficient gas phase CO₂ reduction into
value-added chemicals

Mr. Mohammad Fereidooni



A Dissertation Submitted in Partial Fulfillment of the Requirements
for the Degree of Doctor of Engineering in Chemical Engineering
Department of Chemical Engineering
FACULTY OF ENGINEERING
Chulalongkorn University
Academic Year 2022
Copyright of Chulalongkorn University

ฟิล์มตัวเร่งปฏิกิริยาที่ใช้แสงช่วยสำหรับการรีดิวซ์คาร์บอนไดออกไซด์ในวัฏภาคแก๊สอย่างมีประสิทธิภาพเพื่อเป็นสารเคมีที่มีมูลค่าเพิ่มสูง



วิทยานิพนธ์นี้เป็นส่วนหนึ่งของการศึกษาตามหลักสูตรปริญญาวิศวกรรมศาสตรดุษฎีบัณฑิต
สาขาวิชาวิศวกรรมเคมี ภาควิชาวิศวกรรมเคมี
คณะวิศวกรรมศาสตร์ จุฬาลงกรณ์มหาวิทยาลัย
ปีการศึกษา 2565
ลิขสิทธิ์ของจุฬาลงกรณ์มหาวิทยาลัย

Thesis Title	Photocatalytic films for efficient gas phase CO ₂ reduction into value-added chemicals
By	Mr. Mohammad Fereidooni
Field of Study	Chemical Engineering
Thesis Advisor	PIYASAN PRASERTHDAM
Thesis Co Advisor	SUPAREAK PRASERTHDAM

Accepted by the FACULTY OF ENGINEERING, Chulalongkorn University
in Partial Fulfillment of the Requirement for the Doctor of Engineering

..... Dean of the FACULTY OF
ENGINEERING
(SUPOT TEACHAVORASINSKUN)

DISSERTATION COMMITTEE

..... Chairman
(Okorn Mekasuwandumrong)
..... Thesis Advisor
(PIYASAN PRASERTHDAM)
..... Thesis Co-Advisor
(SUPAREAK PRASERTHDAM)
..... Examiner
(BUNJERD JONGSOMJIT)
..... Examiner
(JOONGJAI PANPRANOT)
..... Examiner
(TAWATCHAI CHARINPANITKUL)

จุฬาลงกรณ์มหาวิทยาลัย
CHULALONGKORN UNIVERSITY

โมฮัมหมัด เฟเรดูนิ : ฟิล์มตัวเร่งปฏิกิริยาที่ใช้แสงช่วยสำหรับการรีดิวซ์คาร์บอนไดออกไซด์ในวัฏภาคแก๊สอย่างมีประสิทธิภาพเพื่อเป็นสารเคมีที่มีมูลค่าเพิ่มสูง. (Photocatalytic films for efficient gas phase CO₂ reduction into value-added chemicals) อ.ที่ปรึกษาหลัก : ปิยะสาร ประเสริฐธรรม, อ.ที่ปรึกษาร่วม : ศุภฤกษ์ ประเสริฐธรรม

การลดปริมาณของคาร์บอนไดออกไซด์ในชั้นบรรยากาศสามารถทำได้โดยผ่านกระบวนการสังเคราะห์แสงของพืชซึ่งสามารถเปลี่ยนคาร์บอนไดออกไซด์และน้ำไปเป็นแป้งและน้ำตาล แต่สำหรับงานวิจัยนี้จะใช้ตัวเร่งปฏิกิริยาที่ใช้แสงช่วยที่เคลือบบนแผ่นฟิล์มบาง ในการเร่งปฏิกิริยาระหว่างคาร์บอนไดออกไซด์และน้ำเพื่อให้เกิดแก๊สมีเทนและคาร์บอนมอนอกไซด์ โดยใช้เครื่องปฏิกรณ์แบบกะและเตาปฏิกรณ์แบบท่อไหล นอกจากการศึกษาเชิงทดลองแล้วยังมีการวิเคราะห์เชิงทฤษฎีในการศึกษากลไกของการเกิดปฏิกิริยาระหว่างตัวเร่งปฏิกิริยาไทเทเนียมไดออกไซด์ชนิดอนันติชั้นที่อุณหภูมิต่ำ (AM-TiO₂-SiO₂) และตัวเร่งปฏิกิริยาเชิงแสงอินเดียมทินออกไซด์ (ITO) ในกรณีของ AM-TiO₂-SiO₂ พบว่าที่พื้นผิวของตัวเร่งปฏิกิริยาที่มีปริมาณ SiO₂ ต่ำ จะมีปฏิสัมพันธ์ที่สูงกว่าในการเจาะจงกับโมเลกุลเป้าหมาย (T-M) โดยปฏิสัมพันธ์ดังกล่าวจะเร่งกระบวนการดูดซับและกระบวนการเกิดปฏิกิริยา แต่อาจจะก่อให้เกิดกระบวนการเสื่อมสภาพของตัวเร่งปฏิกิริยาได้ง่ายเช่นกัน จากการวิเคราะห์ผลเชิงทฤษฎีโดยใช้ DFT พบว่าช่องว่างของออกซิเจน (Ov) เป็นตำแหน่งการเกิดปฏิกิริยารีดักชันสำหรับกระบวนการ CO₂ รีดักชันไปเป็น CO ด้วยอัตราการเกิดปฏิกิริยาที่ 2760±10% μmol.g_{cat}⁻¹.hr⁻¹ และมีความจำเพาะในการเกิดปฏิกิริยาที่สูงบนตัวเร่งปฏิกิริยา ITO ซึ่งจากผลดังกล่าวทำให้ทราบว่า การสูญเสีย Ov เป็นสาเหตุหนึ่งของการเสื่อมสภาพของตัวเร่งปฏิกิริยา ITO นอกจากนี้ผลการนำไฟฟ้าที่แตกต่างกันบนพื้นผิวทั้งสามรูปแบบของตัวเร่งปฏิกิริยา ที่มีต่อการถ่ายเทประจุและความว่องไวในการเกิดปฏิกิริยารีดักชันเชิงแสงของ CO₂ จะคำนวณผ่านทฤษฎีฟังก์ชันนัลความหนาแน่น (DFT) โดยจะมีการวิเคราะห์ผลเชิงแสง และ เคมีไฟฟ้าที่ใช้แสงช่วย ทั้งนี้จากการศึกษาดังกล่าวแสดงให้เห็นว่าพื้นผิวที่สามารถนำไฟฟ้าได้ดีจะสามารถเพิ่มความว่องไวในการเร่งปฏิกิริยาเชิงแสงของปฏิกิริยารีดิวซ์ที่มีการถ่ายเทอิเล็กตรอนหลายตัว เช่น การรีดักชันของ CO₂ ดังนั้น งานวิจัยนี้จึงมีความสำคัญสำหรับการออกแบบตัวเร่งปฏิกิริยาเชิงแสงที่มีประสิทธิภาพและประสิทธิผลสำหรับการรีดักชันของ CO₂ ในสถานะแก๊ส



สาขาวิชา วิศวกรรมเคมี
ปีการศึกษา 2565

ลายมือชื่อนิสิต
ลายมือชื่อ อ.ที่ปรึกษาหลัก
ลายมือชื่อ อ.ที่ปรึกษาร่วม

6273019421 : MAJOR CHEMICAL ENGINEERING

KEYWORD DFT, conductivity, oxygen vacancy, multielectron transfer
D:

Mohammad Fereidooni : Photocatalytic films for efficient gas phase CO₂ reduction into value-added chemicals. Advisor: PIYASAN PRASERTHDAM Co-advisor: SUPAREAK PRASERTHDAM

A viable method to lower the atmospheric CO₂ concentration is artificial photosynthesis, which converts CO₂ and H₂O into products with added value. Herein, the catalytic activity of thin photocatalytic films was examined in water vapor, batch, and flow reactor configurations for CO₂ reduction. In addition to the experimental study, a theoretical analysis of the reaction mechanism over silica-modified amorphous TiO₂ (AM-TiO₂-SiO₂) and indium tin oxide (ITO) photocatalysts is conducted. In the case of AM-TiO₂-SiO₂, the research shows that surfaces with low loading of SiO₂ groups have a higher affinity for certain target molecules (T-M). This affinity accelerates adsorption and reaction but it may hinder the proceed of the reaction and lead to the deactivation of the catalyst. The oxygen vacancy (O_v) was identified as the primary reaction site for CO₂ reduction to CO with a production rate of $2760 \pm 10\% \mu\text{mol.g}_{\text{cat}}^{-1}.\text{hr}^{-1}$ and high selectivity in the DFT modeling of the reaction mechanism for ITO catalyst. According to the proposed reaction mechanism, the loss of O_v could be one of the causes of the ITO catalyst's deactivation. Furthermore, the effect of three different substrates with various conductivities on charge transfer and activity in the photocatalytic CO₂ reduction was investigated using density functional theory (DFT) calculations, and optical and photo-electrochemical analyses. We demonstrated that a conductive substrate could enhance the photocatalytic activity of multielectron transfer reduction reactions such as CO₂ reduction. Our research has implications for the design of an efficient and effective photocatalyst for gas-phase CO₂ reduction.

จุฬาลงกรณ์มหาวิทยาลัย
CHULALONGKORN UNIVERSITY

Field of Study: Chemical Engineering

Student's Signature

Academic Year: 2022

.....
Advisor's Signature

Year:

.....
Co-advisor's Signature

.....

ACKNOWLEDGEMENTS

Before all else, I would like to thank God. He has provided me with strength and support throughout the difficult phases of my research. I also appreciate my family's unconditional love and support.

I'd also like to express my gratitude to the following persons, without whom I would not have been able to carry out this study and finish my Ph.D. program.

Prof. Piyasan Prasethdam, my advisor, has been very kind in allowing me to work in his prestigious research group. The success of this research was made possible by his continuous guidance, optimism, encouragement, and patience during my Ph.D. studies.

I'd also like to extend my gratitude to my co-advisor, Prof. Dr. Supareak Prasertthdam, for his insightful comments and feedbacks.

Prof. Oswaldo Núñez, Victor Márquez, Mohammad Yazdanpanah, Mohammad Rahim Pour, Dr. Christian Paz, Dr. Janaina Santos, Dr. Tinakorn, Dr. Meena, and many more in the center of excellence in catalysis, have all been immense sources of support and inspiration to me throughout my research, and I am grateful to them all.

In particular, I'd want to thank the members of my thesis committee for taking the time to review my work and provide insightful feedback that helped me refine my manuscript.

At last, I'd want to express my gratitude to the graduate program for ASEAN or Non-ASEAN countries at Chulalongkorn University, where I was granted a scholarship and research support.

Mohammad Fereidooni

TABLE OF CONTENTS

	Page
ABSTRACT (THAI)	iii
ABSTRACT (ENGLISH).....	iv
ACKNOWLEDGEMENTS	v
TABLE OF CONTENTS.....	vi
LIST OF TABLES	x
LIST OF FIGURES	xi
CHAPTER I:.....	1
INTRODUCTION.....	1
1.1 Objective	2
1.2 Scope of the research.....	3
CHAPTER II:.....	4
BACKGROUND AND LITERATURE REVIEW	4
2.1 General principles of photocatalytic CO ₂ reduction.....	4
2.2 Photocatalytic films	5
2.3 TiO ₂ photocatalyst.....	7
2.4 ITO photocatalyst.....	8
CHAPTER III:.....	10
EXPERIMENTAL SECTION	10
3.1 Catalyst preparation.....	10
3.1.1 Preparation of chemically attached amorphous TiO ₂ catalyst on the ITO-PET substrate.....	10
3.1.2 Synthesis of AM-TiO ₂ -SiO ₂ and P25-SiO ₂ photocatalysts and preparation of films by spin coating method on the PET, ITO-PET, and Ti substrates	11
3.1.3 Specifications of ITO-PET and ITO-Glass photocatalytic films....	11
3.2 Characterization.....	12

3.2.1 SEM-EDX	12
3.2.2 X-ray diffraction (XRD).....	12
3.2.3 X-ray photoelectron spectroscopy (XPS).....	12
3.2.4 Fourier transformed Infra-red (FT-IR).....	13
3.2.5 Photoluminescence spectroscopy (PL).....	13
3.2.6 Diffuse reflectance UV–Vis spectra (UV–Vis DRS).....	13
3.2.7 Raman spectroscopy.....	13
3.2.8 Electrochemical measurements.....	13
3.2.9 Open circuit potential decay (OCPD) measurement	14
3.2.10 Kelvin probe force microscope (KPFM).....	14
3.3 Computational method.....	14
3.3.1 Computational method for AM-TiO ₂ -SiO ₂ /ITO-PET catalyst	14
3.3.2 Computational method used to calculate the projected density of states (DOSs) for different catalysts and substrates	17
3.4 Photocatalytic CO ₂ reduction tests and measurement of products.....	19
CHAPTER IV:	21
RESULTS AND DISCUSSION	21
4.1 PCO ₂ R on the AM-TiO ₂ -SiO ₂ /ITO-PET	21
4.1.1 Yields of produced CH ₄ , CO, and H ₂ in PCO ₂ R in water vapor	21
4.1.2 Characterization	22
4.1.2.1 XRD	22
4.1.2.1 Raman spectrum of the catalyst.....	23
4.1.2.3 FTIR spectrum of AM-TiO ₂ -SiO ₂ /ITO-PET	25
4.1.2.4 Photoluminescence spectroscopy (PL)	25
4.1.2.5 UV-Vis DRS and band gap estimation	26
4.1.2.6 EDX elemental mapping of AM-TiO ₂ -SiO ₂ /ITO-PET catalyst	27
4.1.3 Affinity trends by MD simulation.....	27
4.1.4 Simulated PCO ₂ R mechanism of AM-TiO ₂ -SiO ₂ /ITO-PET catalyst	34

4.2 effect of substrate conductivity on AM-TiO ₂ -SiO ₂ and P25-SiO ₂ for water vapor PCO ₂ R	36
4.2.1 Characterization	36
4.2.1.1 XRD and FTIR	36
4.2.1.2 UV-Vis DRS, Band gap, and band edge position.....	38
4.2.1.3 Photoluminescence (PL) analysis	40
4.2.1.4 Cyclic voltammetry and relation between the divergence from Mott-Schottky behavior and the dynamics of trapping and untrapping	42
4.2.1.5 SEM/EDAX analysis of AM-TiO ₂ -SiO ₂ and P25-SiO ₂ catalysts.....	43
4.2.1.6 XPS analysis of synthesized AM-TiO ₂ -SiO ₂ and P25-SiO ₂ photocatalysts	44
4.2.1.7 Open circuit potential decay (OCPD) and KPFM analysis	45
4.2.2 PCO ₂ R results for catalysts on different substrates	49
4.2.3 Discussion on the effect of various substrates in PCO ₂ R.....	51
4.3 Experimental and theoretical study on ITO thin films for PCO ₂ R.....	54
4.3.1 Characterization	54
4.3.1.1 UV-Vis DRS, PL, and band edge measurement.....	54
4.3.1.2 XRD	56
4.3.1.3 XPS analysis of ITO-Glass and ITO-PET films.....	57
4.3.2 Photocatalytic CO ₂ reduction on ITO-PET and ITO-Glass thin films	59
4.3.2.1 Batch reactor.....	59
4.3.2.2 Flow reactor.....	61
4.3.3 Simulation of CO ₂ reduction mechanism on In ₂ O ₃ and ITO	63
CHAPTER V:.....	69
CONCLUSIONS AND RECOMMENDATIONS.....	69
5.1 Conclusions	69
5.2 Recommendations	69

REFERENCES..... 71
VITA..... 89



LIST OF TABLES

	Page
<i>Table 1. Composition of simulated media.....</i>	30
<i>Table 2. The quantity and variety of molecules present in each environment for surface affinity trend simulations.</i>	60



LIST OF FIGURES

	Page
Figure 1. The General mechanism of photocatalytic CO ₂ reduction(PCO ₂ R)[22].	5
Figure 2. a) comparison between XRD-theoretical and XRD-experimental, b) polyhedron and ball-stick visualization.	15
Figure 3. The models constructed for the DOS simulation.	18
Figure 4. a) Simulated XRD of the ITO and measured XRD of ITO-Glass catalyst, (b) Simulated XRD of In ₂ O ₃ .	19
Figure 5. The yield of produced (a) CH ₄ , (b) H ₂ , and (c) CO.	22
Figure 6. XRD patterns of AM-TiO ₂ , and AM-TiO ₂ -SiO ₂ .	23
Figure 7. Raman spectra of (a) AM-TiO ₂ , and (b) AM-TiO ₂ -SiO ₂ .	24
Figure 8. Embedded silicate ions and silanol groups on the AM-TiO ₂ surface.	24
Figure 9. FTIR spectrum of AM-TiO ₂ -SiO ₂ /ITO-PET.	25
Figure 10. AM-TiO ₂ -SiO ₂ /ITO-PET PL spectrum. The PL emission spectra of AM-TiO ₂ and AM-TiO ₂ -SiO ₂ powders are shown in the inset.	26
Figure 11. a) UV-Vis DRS, and b) Tauc's plot of AM-TiO ₂ -SiO ₂ powder and AM-TiO ₂ -SiO ₂ /ITO-PET film.	27
Figure 12. EDX elemental mapping shows the presence of (a) Ti, (b) In, (c) Si, and (d) Sn.	27
Figure 13. AM-TiO ₂ , AM-TiO ₂ -LLSiO ₂ , and AM-TiO ₂ -HLSiO ₂ simulation boxes. The following colors indicate the atoms: H-white, O-red, Ti-pink, and Si-green.	29
Figure 14. E _{binding} in the high-humid medium.	31
Figure 15. E _{binding} in the low-humid medium.	32
Figure 16. Low humidity simulation medium boxes for AM-TiO ₂ and AM-TiO ₂ -LLSiO ₂ . C-gray, H-white, O-red, Ti-pink, and Si-green are the colors used to symbolize the atoms.	33
Figure 17. The ΔG profile of AM-TiO ₂ catalyst. C-gray, H-white, O-red, and Ti-pink are the colors that depict the atoms.	34
Figure 18. The proposed reaction pathway of the ZI. C-gray, H-white, O-red, and Ti-pink are the colors that represent the atoms.	35

<i>Figure 19. The ΔG profile of Z2.</i>	36
<i>Figure 20. The proposed reaction pathway of the Z2. C-gray, H-white, O-red, Si-green, and Ti-pink are the colors that represent the atoms.</i>	36
<i>Figure 21. a) AM-TiO₂-SiO₂ and P25-SiO₂ XRD patterns, b) AM-TiO₂-SiO₂ and P25-SiO₂ FTIR spectra</i>	38
<i>Figure 22. (a) UV-vis diffuse reflectance spectra of AM-TiO₂-SiO₂ and P25-SiO₂, (b) Mott-Schottky plots of AM-TiO₂-SiO₂, P25-SiO₂, and ITO-PET obtained at different frequencies, (c) Tauc's plot of the AM-TiO₂-SiO₂ and P25-SiO₂ catalysts, (d) The band edge positions of the AM-TiO₂-SiO₂ and P25-SiO₂ catalysts with respect to the water oxidation and reduction potentials.</i>	40
<i>Figure 23. PL spectra of a) AM-TiO₂-SiO₂ and P25-SiO₂ powders, b) Catalysts on Ti substrate, c) ITO-PET substrate and catalyst films on the substrate, and d) PET substrate and catalyst film on the substrate.</i>	42
<i>Figure 24. Mott-Schottky behavior divergence and trapping/untrapping dynamics by surface states for (a) P25-SiO₂-ITO-PET, and (b) AM-TiO₂-SiO₂-ITO-PET.</i>	43
<i>Figure 25. (a) – (e) SEM/EDAX images of AM-TiO₂-SiO₂, and (f) – (j) SEM/EDAX images of P25-SiO₂.</i>	44
<i>Figure 26. High-resolution XPS spectrum of Ti 2p, Si 2p, and O 1s in both AM-TiO₂-SiO₂ and P25-SiO₂ catalysts.</i>	45
<i>Figure 27. OCPD of AM-TiO₂-SiO₂ and P25-SiO₂ catalyst on ITO-PET and Ti substrates.</i>	47
<i>Figure 28. Work function images in 3D for (a) AM-TiO₂-SiO₂, and (b) P25-SiO₂, (c) histogram of work function, (d) average work function, (e) position of fermi level of catalysts (E_v = energy of vacuum, $e\Phi$ = average work function).</i>	48
<i>Figure 29. KPFM images and film thickness of a) AM-TiO₂-SiO₂-ITO-PET, and b) P25-SiO₂-ITO-PET.</i>	49
<i>Figure 30. Yields of produced CH₄ and CO for catalysts on different substrates.</i>	50
<i>Figure 31. The yield of produced CH₄ for AM-TiO₂ and P25-TiO₂ on different substrates.</i>	51
<i>Figure 32. Projected density of states for different catalysts and substrates.</i>	53
<i>Figure 33. (a) – (e) proposes charge transfer mechanism between substrate and catalyst, (f) schematic representation of CO₂ reduction over photocatalyst.</i>	54

<i>Figure 34. a) UV-Vis spectra with embedded Tauc's plot, b) PL spectra at the excitation wavelength of 300 nm, c) Mott-Schottky plots, and d) Schematic of the band structure for ITO-PET and ITO-Glass.</i>	56
<i>Figure 35. XRD patterns of ITO-PET and ITO-Glass films.</i>	57
<i>Figure 36. XPS spectra of a) In 3d, b) Sn 3d, and c) O 1s for ITO-PET, XPS spectra of d) In 3d, e) Sn 3d, and f) O 1s for ITO-Glass, and (g)-(i) high-resolution XPS for In 3d, Sn 3d, and O 1s of ITO-Glass under 365 nm light irradiation.</i>	58
<i>Figure 37. (a) and (b) CH₄ and CO yields from photocatalytic CO₂ reduction on ITO-PET and ITO-Glass, respectively. (c) ITO-PET and ITO-Glass stability during photocatalytic CO₂ reduction.</i>	60
<i>Figure 38. Images of simulation boxes used to compute $E_{binding}$ for the environments (a) ENV-1, (b) ENV-2, (c) ENV-3, (d) ENV-4, and (e) the environments' estimated $E_{binding}$.</i>	61
<i>Figure 39. Yields of (a) CH₄ and (b) CO production from photocatalytic CO₂ reduction in the flow system.</i>	62
<i>Figure 40. Study of external mass transfer effect on the rate of CO₂ conversion to CH₄ over ITO-Glass catalyst.</i>	63
<i>Figure 41. The ΔG profiles for CO₂ reduction on (a) lattice oxygen (O_L) of In₂O₃, (b) oxygen vacancy (O_V) of In₂O₃.</i>	64
<i>Figure 42. The ΔG profile of CO₂ reduction on O_V site between In atoms.</i>	65
<i>Figure 43. The ΔG profile of CO₂ reduction on O_V site between In atoms close to Sn atom.</i>	66
<i>Figure 44. The ΔG profile for CO₂ reduction into CO and CH₄ on the O_L site close to Sn atom.</i>	68

CHAPTER I:

INTRODUCTION

In October 2022, the amount of carbon dioxide (CO₂) in our atmosphere surpassed 415 ppm [1]. Unquestionably, this gas is the principal driver of the greenhouse effect, which has led to climate change mostly as a result of emissions from the transportation, manufacturing, and residential sectors. Fossil fuel combustion and industrial processes including the production of iron, steel, and cement as well as petrochemical refining are the primary sources of CO₂ emissions. Presently, carbon capture and storage[2] and carbon capture and utilization[3] are the two methods being used to counter the steadily rising CO₂ levels in our atmosphere. In order to permanently store CO₂ in a geological body, carbon capture and storage depends on CO₂ collection, including its separation, compression, and transport. In any regard, it does not incorporate CO₂ conversion, and its technological and financial viability on a wide scale has not been established. In comparison, carbon capture and utilization may directly utilize CO₂ or convert it through chemical and/or biological processes into value-added products[3,4]. As a chemical precursor, CO₂ has the potential to reduce the usage of hydrocarbon-based fuels like gasoline, which are currently made from petroleum[5] and are significant contributors to the emission of greenhouse gases. The production of chemical compounds and fuels from CO₂ can improve the carbon and energy efficiency of current technologies and promote the invention of new, and green industrial processes[6,7].

One of the most promising methods for reducing atmospheric CO₂ emissions and producing renewable fuels at the same time is the light-induced conversion of CO₂ and water into chemicals and fuels with the help of a photocatalyst, simulating the natural photosynthetic process[8–11]. Artificial photosynthesis is the term used to describe the process of employing solar light, water as a reducing agent, and a photocatalyst[12,13]. However, artificial photosynthesis's present light-to-fuel efficiency is less than 1%, and in the majority of situations, it has to be raised. For artificial photosynthesis to be commercially viable, light efficiency rates of 10% or more are reportedly needed. This is because commercial solar photovoltaic systems

have solar energy conversion efficiencies of $>20\%$ [14]. Before artificial photosynthesis can be taken into consideration as a prospective large-scale process, it must also be carried out under continuous flow. The majority of research on heterogeneous photocatalysts is conducted in slurry systems, which not only makes the separation of catalysts difficult and costly but also introduces secondary pollution[15]. Consequently, supporting the catalyst on a substrate will enhance its practicality and makes efficient use of the catalyst in a flow system. On account of the superiority of photocatalyst films over powders, photocatalyst films may be utilized in the gas phase reduction of CO_2 , which increases the light-harvesting capability of the catalyst in comparison to slurry systems. While the CO_2 reduction process is complex, the gas phase CO_2 reduction mechanism is simpler and more selective for CH_4 , CO , and H_2 [16]. In addition, the issue of CO_2 solubility in the liquid phase does not present in the gas phase [15].

In this study, films of crystalline or amorphous TiO_2 with or without SiO_2 modification on various substrates were prepared and studied for photocatalytic CO_2 reduction in water vapor. In the same procedure, ultrathin films of indium tin oxide (ITO) were also examined. Using density functional theory (DFT) and molecular dynamics (MD) simulations, the possible mechanism of CO_2 reduction, the effect of substrate on the activity of the catalyst, and the surface affinity of the catalyst towards the constituent molecules of the reaction medium were investigated. This study's results have the potential to lead to the development of more effective photocatalytic systems for CO_2 reduction.

1.1 Objective

Study the effect of defects in metal oxide films and substrate's conductivity on activity, selectivity, and stability of photocatalyst in vapor phase CO_2 reduction.

1.2 Scope of the research

- Preparation of amorphous TiO_2 modified with SiO_2 film on the indium tin oxide coated polyethylene terephthalate substrate (AM- TiO_2 - SiO_2 /ITO-PET) for CO_2 reduction in water vapor.
- Study the mechanism of CO_2 reduction on AM- TiO_2 - SiO_2 /ITO-PET photocatalyst via DFT simulation.
- Examine the deactivation of the AM- TiO_2 - SiO_2 /ITO-PET catalyst by MD simulation.
- Fabrication of photocatalytic films of amorphous and crystallized TiO_2 on different substrates with various conductivity for CO_2 reduction in the vapor phase.
- Study the effect of the substrate's conductivity on the activity of the photocatalyst in the CO_2 reduction reaction.
- Evaluate the activity and stability of the ITO-PET and ITO-Glass thin photocatalytic films for CO_2 reduction in batch and continuous reactors.
- Study the mechanism of CO_2 reduction over ITO photocatalyst by DFT simulation.

CHAPTER II:

BACKGROUND AND LITERATURE REVIEW

2.1 General principles of photocatalytic CO₂ reduction

The following three key phases are part of the general photocatalytic CO₂ reduction process: (1) generation of e⁻/hole pairs upon absorption of light with equal or greater energy than the band gap of the catalyst, (2) separation and migration of e⁻/hole pairs to the active sites where the CO₂ molecule is adsorbed, (3) interfacial charge transfer to the adsorbed CO₂. At the same time, photogenerated holes are used in the oxidation of water into O₂. During migration, a significant proportion of e⁻/hole pairs may be lost through recombination. Recombination of e⁻/holes can be somewhat prevented by rational active site design, such as defect creation, facet engineering, and loading the catalyst with organic or inorganic components. Otherwise, the accumulation of charge carriers could either lead to photo-corrosion of the catalyst or decrease the efficiency of the photocatalytic reaction[17,18].

The CO₂ molecule that has been adsorbed could act as an electron acceptor and donor[19]. While the carbon atom may take an electron from the Lewis base sites, unpaired oxygen electrons may be transferred to the Lewis acid sites. Therefore, altering the active sites' electronic properties may improve CO₂ adsorption. After the CO₂ molecule adsorbs on the active sites, it can be polarized, leading to electron-repulsion-inducing bent bonding. The resulting reduced LUMO (lowest unoccupied molecular orbital) level of the bent CO₂ molecule makes electron acceptance easier[20]. Ultimately, the combination of multi-electron transfer and the multi-step reduction of CO₂, involving the breaking of C=O bonds and generation of C-H bonds, results in the formation of several distinct products[21]. The general mechanism of photocatalytic CO₂ reduction is shown in **Error! Reference source not found.**

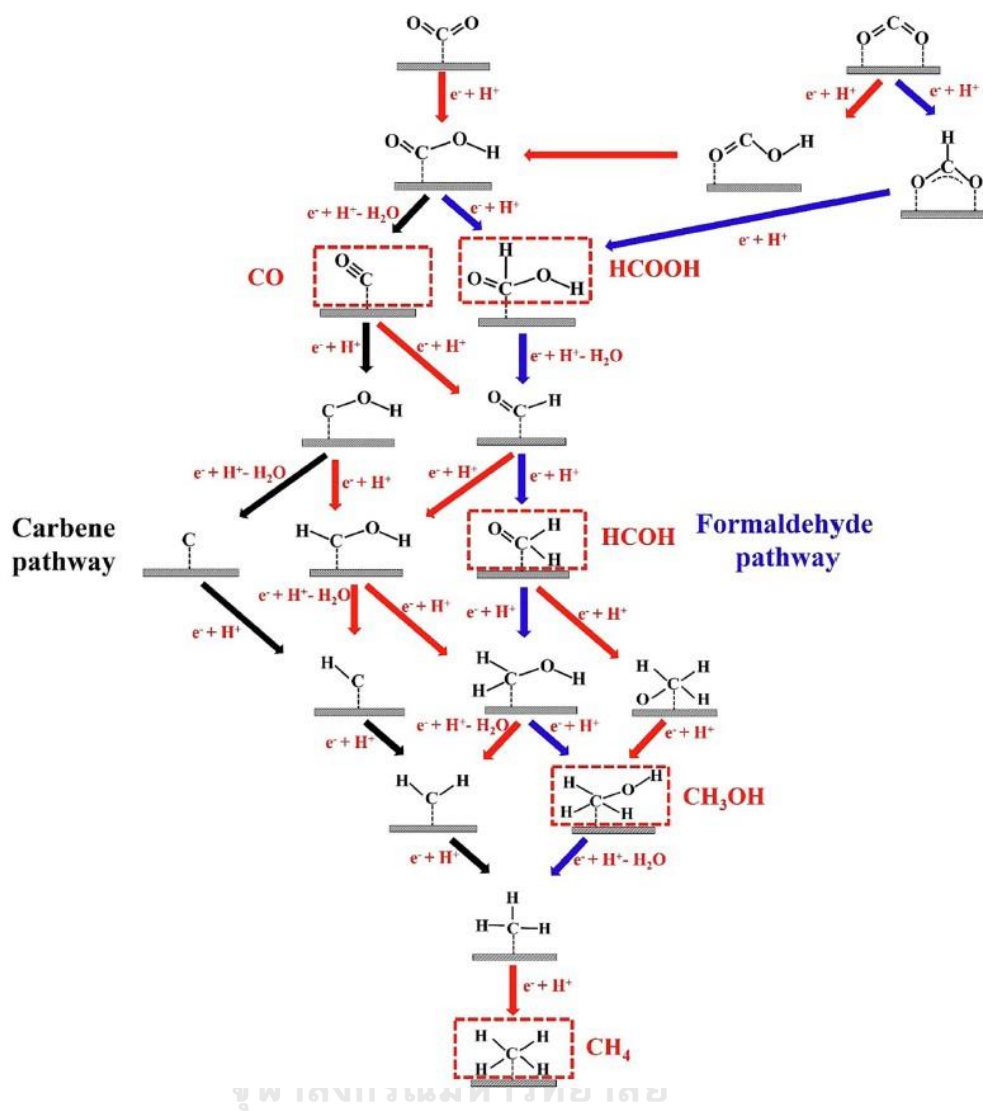


Figure 1. The General mechanism of photocatalytic CO₂ reduction(PCO₂R)[22].

2.2 Photocatalytic films

The majority of heterogeneous photocatalysts for CO₂ reduction are studied in slurry systems, which raises the danger of secondary pollution from the catalyst leaching into the liquid phase as well as making catalyst separation challenging and expensive[15]. Therefore, positioning the catalyst on a substrate will increase its applicability and the substrate itself could also improve the overall photocatalytic activity of the catalyst (a subject that has been less studied in the field of photocatalyst). Numerous studies have been conducted on the formation of

photocatalyst films on a variety of soft or hard substrates, including glass[23–27], activated carbon[28,29], polymers[30–32], silica gel[33–35], metal foams[36–40], etc. The flexibility, thermal stress, and substrate-catalyst adhesion were among the physical characteristics of the substrate on which the research concentrated. For instance, flexible photocatalytic active films of $\text{TiO}_2/\text{SiO}_2$ composite for bacterial disinfection in solar light were prepared by Levchuk et al. in 2019[41]. The flexible substrate in their study was made of polyethylene terephthalate (PET), but the photocatalytic activity was only attributed to the catalyst, and the influence of the substrate on the mobility of the charge carriers was not factored. While organic semiconductors (polymers like PET) have received a lot of attention in the development of flexible electronics, such as flexible solar cells and transparent thin-film transistors (TTFTs). It has been demonstrated that different polymer substrates have varied charge carrier mobility in flexible electronics[42]. Additionally, the preparation of both doped and bare TiO_2 nanotube films (TNTFs) (films over titanium substrate) using electrochemical anodization is well-researched. This method allows for high control over TNTF properties such as tube diameter, wall thickness, length, decoration, and filling of dopants, and density of the nanotubes[43]. But without considering the function of the titanium substrate, the photocatalytic activity of the TNTFs is attributed to the shape and crystal structure of the oxide layer. More studies have been conducted on amorphous photocatalysts for reduction reactions after the work of Zywitzki et. al. 2017[44] on photocatalytic H_2 evolution over amorphous TiO_2 , and the findings demonstrated the crucial significance of numerous defects for electron transport in photocatalytic reduction reactions. In this line, Santos et al. 2021[45] reported the synthesis of amorphous TNTF for gas phase photocatalytic CO_2 reduction with high methane generation yield using the anodization approach. The defects and many OH groups on the surface of the amorphous TiO_2 oxide layer, which has been the subject of recent studies, were thought to be responsible for the catalyst's activity in their work. Additionally, one-dimensional nanomaterials like TNT are regarded as the best candidates for lithium-ion battery applications due to their large surface area and short lithium diffusion path (LIBs). With the benefit of removing the requirement for an additional conductive substance in the LIBs, the Ti

substrate of the anodized TNTFs in the LIBs may serve as the optimal electron collector[46].

The utilization of surface plasmon resonance (SPR) is one method to improve the light absorption efficiency of photocatalysts, which has drawn growing interest. The collective oscillation of free electrons in conducting materials is referred to as SPR. Energy-rich hot carriers may be created when the incident light's frequency coincides with the plasmon's natural frequency. These hot carriers can take part in photochemical processes. As a result, adding plasmonic materials to photocatalytic devices may greatly enhance the absorption and conversion of light[47–49]. Regarding this, Zakaria et al. (2019)[50] reported the SPR of a fiber that had been side-polished and coated in Ti of various thicknesses. The Ti films showed SPR in the visible region of the light spectrum, regardless of their thickness. The SPR of ITO-coated fiber optics of various thicknesses for use as hydrogen gas sensors was also studied by Mishra et al. (2012)[51]. It was found that the resonance wavelength and ITO film thickness were linearly correlated. The ITO layer's resonance wavelength varied from almost 500 nm at a thickness of 50 nm to almost 760 nm at a thickness of 110 nm.

2.3 TiO₂ photocatalyst

TiO₂ is the most researched photocatalyst that has been employed for CO₂ photoreduction [52]. TiO₂ primarily has three crystallographic phases, rutile, anatase, and brookite, with band gaps between 3.0 eV and 3.2 eV. The efficiency of CO₂ photoreduction is significantly influenced by the phases of TiO₂. In contrast to rutile and anatase, brookite is proposed to have high activity for CO₂ reduction to CO and CH₄, whereas mixed phases of anatase and rutile are active for CO₂ photoreduction to CH₄. The heterojunction between rutile and anatase, which effectively separates charges, was the cause of the improvement of the mixed phase[53]. In order to minimize excessive recombination of charge carriers, crystallization is typically regarded as a necessary step in the preparation of highly active photocatalysts. There appear to be exceptions to this rule with artificial photosynthesis. Recent discoveries on photocatalytic hydrogen evolution or CO₂ reduction over amorphous TiO₂ imply

that surface characteristics, which dominate interfacial charge transfer rates, may play a greater role than bulk crystallinity in the activity of the photocatalyst for CO₂ reduction[54]. As a result, amorphous photocatalysts have recently drawn increased interest in photocatalytic reduction. Furthermore, TiO₂ is chosen for CO₂ photoreduction because the position of the bands is suitable for both oxidation of water and the reduction of CO₂ into different products[55].

Numerous techniques have been used to enhance the TiO₂ photocatalyst's properties, including surface modification[56], doping[57], non-metal doping[58], coupling with other semiconductors[59], and others. Due to their thermal and mechanical stability as well as their remarkable photocatalytic characteristics, there has been an increasing interest in the synthesis of TiO₂-SiO₂ composites during the past several years. TiO₂-SiO₂ composites have been employed extensively for photocatalytic contamination degradation and self-cleaning coating production [60]. According to the proposal of Halin et al. 2017 [61] on the function of SiO₂ in TiO₂-SiO₂ films made by spin coating, it improves the light transmission, mechanical strength, and thermal stability of titania nanocomposites. Fu et al. 1996 [62] also studied the photocatalytic activity of a TiO₂-SiO₂ composite for the oxidation of ethylene, attributing the enhanced activity to an increase in Bronsted-type surface acidity generated by SiO₂, which might potentially be advantageous for the CO₂ reduction[54].

2.4 ITO photocatalyst

Indium tin oxide (ITO) has received less attention in the field of heterogeneous photocatalysis, although it has unique characteristics such as non-toxicity, simplicity of production, physical and chemical stability, and the presence of defect levels[63,64]. Doping indium oxide (In₂O₃) with tin oxide (SnO₂), two materials with wide band gaps, yields a material with a band gap of around 3.6 eV. The resultant indium tin oxide (ITO) becomes "rich in defects," and significant sub-bandgap defect levels begin to emerge. These sub-bandgap defect levels can absorb visible light as well as trap photogenerated electrons and holes. Trapping of charge carriers could enhance photocatalytic activity[65]. In this regard, oxygen vacancy (O_v) and surface

hydroxyl groups (O_H) as significant defects for CO_2 reduction[54] are present in the structure of the ITO catalyst[66]. In the absence of light, thermodynamically unstable O_v s are extremely reactive and can activate CO_2 and even break the molecule[67]. OH groups, on the other hand, as Lewis bases, not only improve CO_2 adsorption but also provide protons for hydrogenation[68,69]. Therefore, ITO could be considered a good candidate for photocatalytic CO_2 reduction.



CHAPTER III:

EXPERIMENTAL SECTION

3.1 Catalyst preparation

3.1.1 Preparation of chemically attached amorphous TiO₂ catalyst on the ITO-PET substrate

50 ml of ethanol and 5 ml of acetic acid were poured into a beaker, then 6 ml of titanium (IV) isopropoxide was drip-fed. At the same time, the solution was stirred over a magnetic stirrer. This solution was labeled A. In a separate beaker, 35 ml ethanol and 35 ml deionized water were mixed over a magnetic stirrer, and the pH of the solution was adjusted to 3 with HCl. Next, 1 ml of tetraethyl orthosilicate was added dropwise to the solution. This solution was labeled B. Both solutions were stirred overnight. Next, solution A was slowly added to solution B while being vigorously stirred. After one hour, the resulting gel was used for the preparation of the amorphous TiO₂ modified with SiO₂ on the ITO-PET substrate (AM-TiO₂-SiO₂/ITO-PET) film.

In preparing the chemically attached AM-TiO₂-SiO₂ on the ITO-PET substrate, the desired size of the ITO-PET substrate was cut and placed on the bottom of a laboratory tray; therefore, only the ITO-coated side of the film was exposed to the gel. Then the as-prepared gel was poured on the substrate. After 15 min, the film was removed from the gel, washed with abundant deionized water, and dried in the oven at 100 °C for 20 min. Finally, the remaining gel was collected and dried over a hotplate at 100 °C overnight. The weight of the chemically attached catalyst to the substrate was evaluated by the difference in the weight of the substrate before and after coating.

3.1.2 Synthesis of AM-TiO₂-SiO₂ and P25-SiO₂ photocatalysts and preparation of films by spin coating method on the PET, ITO-PET, and Ti substrates

The synthesis procedure for the AM-TiO₂-SiO₂ catalyst is explained in detail in section 3.1.1.

For the synthesis of P25 modified with SiO₂ (P25-SiO₂), 35 ml of ethanol and 35 ml of DI water were mixed in a beaker, and the pH was lowered to 3 using HCl. The solution was mixed continuously for five hours after 1 ml of tetraethyl orthosilicate was added to it. The solution was then mixed with 2 grams of P25 and stirred for two hours. The resulting gel was dried in an oven at 100 °C overnight.

The substrates were cleaned before the catalysts were spin-coated. The Ti plate was mechanically polished on all surfaces, including the edges, and then washed with DI water. The polished Ti plate was then cleaned once again by being submerged in a 10% wt. HCl solution while being sonicated for 10 min. The Ti plate was then subjected to 10 minutes of sonication in ethanol, followed by 10 minutes of sonication in DI water. The Ti plate was finally air-dried[45]. The ITO-PET and PET substrates were sonicated in ethanol and DI water for 10 min, followed by air drying.

For the preparation of spin-coated films, the catalysts were dispersed in 2-propanol for 15 min using ultrasonication. The substrates were placed on the spin coater's rotating disk, and the solutions were drop-wisely dispensed to the substrates as they rotated (1500 rpm). The coated substrates were then exposed to air for 30 min before being dried in an oven at 80 °C for 30 min. The weight of the catalyst was adjusted for each film preparation by employing the same volume of ink (catalyst suspended in isopropyl alcohol) and spin rate.

3.1.3 Specifications of ITO-PET and ITO-Glass photocatalytic films

Both the indium tin oxide coated glass film (ITO-Glass) and the polyethylene terephthalate (ITO-PET) film were acquired from the Sigma-Aldrich Company and utilized as is. The ITO layer's thickness on the glass substrate is between 30 and 60 nm, whereas it is 130 nm on the PET substrate, according to information from the manufacturer.

3.2 Characterization

3.2.1 SEM-EDX

Energy-Dispersive X-ray spectroscopy (EDX) and Scanning Electron Microscopy (SEM) were employed to either determine the attachment of the catalyst to the substrate or analyze the composition and dispersion of the catalyst's constituent elements.

3.2.2 X-ray diffraction (XRD)

By employing a Bruker D8 Advance with a Cu anode, K α 1 (1.544 Å) irradiation, a 2θ range of 10° to 80°, and a scan rate of 0.02°/min, the crystalline structure of the materials was examined.

3.2.3 X-ray photoelectron spectroscopy (XPS)

X-ray photoelectron spectroscopy (XPS) for analyzing the oxidation state of the elements was carried out using a Thermo Scientific K-alpha equipped with a monochromatic small-spot X-ray source and a 180° double-focusing hemispherical analyzer with a 128-channel detector. Due to the active argon charge compensation dual beam source, the starting pressure of 8×10^{-8} mbar or less increased to 2×10^{-7} mbar throughout the measurement. A common sample preparation was pressing fresh catalyst onto carbon tape resting on an aluminum sample plate. Spectra were collected using an AlK α X-ray source (1486.6 eV, 72 W) with a 400 μ m spot size. While the constant pass energy for region scans was 50 eV with a step size of 0.1 eV, it was 200 eV with a step size of 0.5 eV for survey scans.

3.2.4 Fourier transformed Infra-red (FT-IR)

Using a Nicolet 6700 FT-IR with a single point Attenuated Total Reflectance (ATR) accessory, Fourier transform infrared spectroscopy is used to examine the surface species and chemical bonding.

3.2.5 Photoluminescence spectroscopy (PL)

To investigate the separation of photo-induced charge carriers, photoluminescence spectroscopy (PL) study utilizing a Horiba 4P-Fluoromax spectrofluorometer was carried out.

3.2.6 Diffuse reflectance UV-Vis spectra (UV-Vis DRS)

A LAMDA 650 UV/Vis spectrophotometer was used to acquire diffuse reflectance spectra (UV-Vis DRS) with wavelengths ranging from 200 to 800 nm. The resultant spectra were used to examine the catalysts' ability to absorb light and their band gap.

3.2.7 Raman spectroscopy

With the sample at room temperature, Raman spectra were acquired using a HORIBA spectrometer (MicroHR Raman) equipped with a 532 nm Nb/YAG laser of 100 mW power. After passing through a grating (1800 groove/mm) with an edge filter to eliminate backscattered light, the signal was detected by an open electrode CCD detector with an accuracy of 1 cm^{-1} .

3.2.8 Electrochemical measurements

To locate the conduction band (CB) for the catalysts, electrochemical impedance measurements were made in a three-electrode cell using an Autolab(R) model M280 fitted with a FRA module. A platinized titanium mesh and Ag/AgCl (KCl 3 M) were utilized as the counter and reference electrodes in this measurement, respectively,

with the catalyst operating as the working electrode. The measurements were conducted between 1.1 and -1.1 V by applying a sinusoidal perturbation of 10 mV in the range of 1 kHz to 1 Hz, and the pH of the solution was maintained at 7 by employing a phosphate solution (0.1M).

3.2.9 Open circuit potential decay (OCPD) measurement

Using a commercial 1.75 ml R/T/A spectro-electrochemical cell (Redox.me) with a Pt wire as the counter electrode, Ag/AgCl as the reference electrode, and the catalyst film as the working electrode, OCPD measurements were carried out to determine the stability of the photo-generated electrons. A 1000W Xe Lamp was used to illuminate the sample until the open circuit potential was steady (30 min). After then, the light was switched off, and the open circuit potential was monitored until it stabilized (in the dark) (30 min). The experiments were carried out using either N₂ or CO₂-saturated 0.1M phosphate buffer (pH=7).

3.2.10 Kelvin probe force microscope (KPFM)

The NX10 atomic force microscope (AFM) from Park Systems Corporation was used under ambient settings to perform Kelvin probe force microscopy (KPFM). Before the AFM experiment, the samples were individually coated on conductive indium tin oxide substrates.

3.3 Computational method

3.3.1 Computational method for AM-TiO₂-SiO₂/ITO-PET catalyst

With the BIOVIA Materials Studio 0.7 program, all of the theoretical computations were carried out. The melt-quench process [70] was used to initially build amorphous TiO₂ crystals, and density functional theory (DFT) was then used to reoptimize the molecular dynamic cell(MD-cell). The Forcite module was used in the MD melt-quench process while employing a Universal forcefield [71]. A TiO₂ Anatase phase

supercell with 48 atoms heated up to 4726.85 °C and maintained for 40 ps at a rate of 117.5 K/ps. After that, it was cooled at a rate of 0.235 K/ps to room temperature while holding for 10 ps. In an isobaric ensemble, the time step for the MD melt-quench approach was 2 fs (NPT). A barostat and No se-Hoover-Langevin (NHL) thermostat with time constants of 0.1 and 0.4 ps were used. The Generalized Gradient Approximation (GGA), the Perdew-Burke-Ernzerhof Function (PBE), and a plane-wave cut-off of 500 eV were used by the CASTEP module to perform the DFT re-optimization[72]. The layers were multiplied using the SuperCell tool after the generation of amorphous TiO₂, and then a vacuum was added. The size of the simulation boxes were $a = 34.273 \text{ \AA}$, $b = 18.224 \text{ \AA}$, $c = 27.886 \text{ \AA}$, $\alpha = \beta = 90^\circ$, and $\gamma = 117.21^\circ$. In this phase, the constructed crystal structure's XRD was simulated, and the results were compared to the measured XRD of the AM-TiO₂ to ensure that the simulation of the catalyst's structure was accurate (*Figure 2*). After that, the exposed surfaces were modified by silicon dioxide OH groups. Finally, 100 molecules overall, at various loads of target molecules (T-M), and water, were placed into systems.

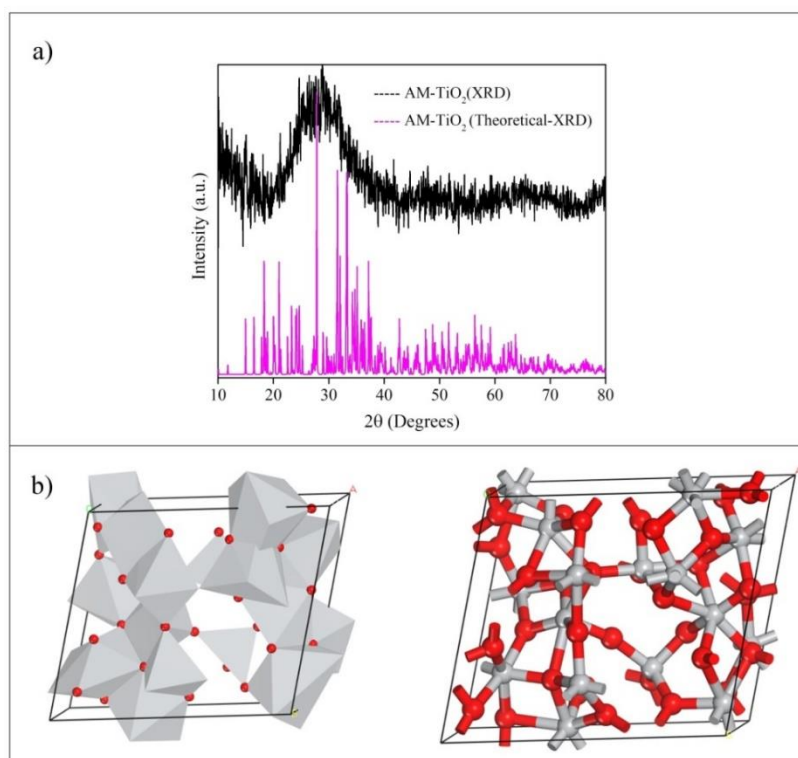


Figure 2. a) comparison between XRD-theoretical and XRD-experimental, b) polyhedron and ball-stick visualization.

Prior to MD, all simulation boxes had been fully optimized using the Ye Tian method[73]. With the use of the Forcite module, MD simulation was performed on the canonic ensemble NVT [74] at 39 °C with a 0.1 fs time step, 100 ps total simulation duration, 1,000,000 steps, and NHL thermostat.

The DFT optimization was carried out by the DMol3 module using the functional generalized gradient approximation (GGA) based on Perdew Wang (PW-91)[75,76], with the condition in the electronic exchange being double-numeric quality basis set DND 3.5. All the molecules that make up the medium in the interface (Mx molecules) were built and afterward optimized by Ye Tian method[73]. The convergence criteria utilized were as follows: difference in total energies of 1×10^{-5} Ha, maximum force per atom of 0.002 Ha/Å, and maximum displacement between cycles of 0.005 Å[77].

DFT calculations have been used to evaluate the photocatalytic CO₂ reduction(PCO₂R) by AM-TiO₂-SiO₂/ITO-PET. Using the DMol3 algorithm and GGA with PBE, the structural optimization of each mechanism step and the computation of Gibbs free energy (ΔG) were accomplished. The relativistic effect of transition atoms was evaluated using the DFT semi-core pseudopotential (DSPP) approach and double numerical plus polarization (DNP) basis set[78]. For an accurate description of the weak interactions between species participating in the PCO₂R reaction and the catalyst, the PBE + D2 method with the Grimme Van der Waals corrections was used. The convergence conditions for structure optimization were as follows: total energy difference of 1×10^{-5} Ha, maximum force per atom of 0.002 Ha/Å, a maximum displacement between cycles of 0.005 Å, and Monkhorst–Pack k-point sampling of $1 \times 2 \times 1$ [78]. The ΔG for each step was calculated using Equation 1:

$$\Delta G = \Delta E + \Delta E_{ZPE} - T\Delta S \quad \text{Equation (1)}$$

In **Equation (1)**, ΔE represents the total electronic and ionic energy as calculated by DFT (catalyst total energies), ΔE_{ZPE} represents the change in zero-point energy, T represents the temperature (298.15 K), and ΔS represents the change in entropy. Calculations of zero-point energy and entropies were based on the vibrational frequencies of PCO₂R intermediates[78].

3.3.2 Computational method used to calculate the projected density of states (DOSs) for different catalysts and substrates

All density functional theory (DFT) calculations were performed with the Cambridge Sequential Total Energy Package (CASTEP). The cut-off energy for the exchange-correlation functional was set at 450 eV, and the generalized gradient approximation (GGA) of Perdew-Burke-Ernzerhof (PBE) was employed. The valence electrons' Kohn-Sham orbitals were described by a planewave basis set, while the interactions between electrons and ions were described by an ultrasoft pseudo-potential. The energy, maximum stress, maximum pressure, and maximum displacement distance convergence limits were 2×10^{-5} eV/atom, 0.05 eV/Å, 0.1 GPa, and 0.002 Å, respectively. The lattice constants and atomic positions were optimized in geometry optimization [79–83]. For simulation, slab systems of Ti(101), ITO(110), PET, rutile and anatase TiO₂ (110) modified with SiO₂ were constructed (*Figure 3*). For the computation of density of state (DOS), a 6×6×1 k-point sample grid was employed for the Brillouin zone[82].

Melt-quench was employed to generate the ITO crystal, which was subsequently optimized with DFT. Using the Forcite module and the Universal forcefield, the melt-quench method [71] was executed. The optimized In₂O₃ cell was then utilized to produce a supercell with a Sn/In ratio of 0.01. At a rate of 117.5 K/ps, the 120-atom supercell was heated to 4726.85 °C and then held for 40 ps. It was then cooled to room temperature at a rate of 0.235 K/ps and kept at that temperature for 10 ps. The time step of the ITO melt-quench method in an isobaric ensemble was 2 fs (NPT). Utilized were a Nosé-Hoover-Langevin (NHL) thermostat and barostat with respective time constants of 0.1 and 0.4 ps. In this stage, the XRD of the In₂O₃ and ITO was simulated to ensure the correct construction of the structures(*Figure 4*). The CASTEP module re-optimized the DFT using the Generalized Gradient Approximation (GGA), the Perdew-Burke-Ernzerhof Function (PBE), and a plane-wave cut-off of 500 eV[72].

Moreover, the mechanism of CO₂ reduction on In₂O₃ and ITO was simulated by the DFT calculation at the conditions described in section 3.3.1.

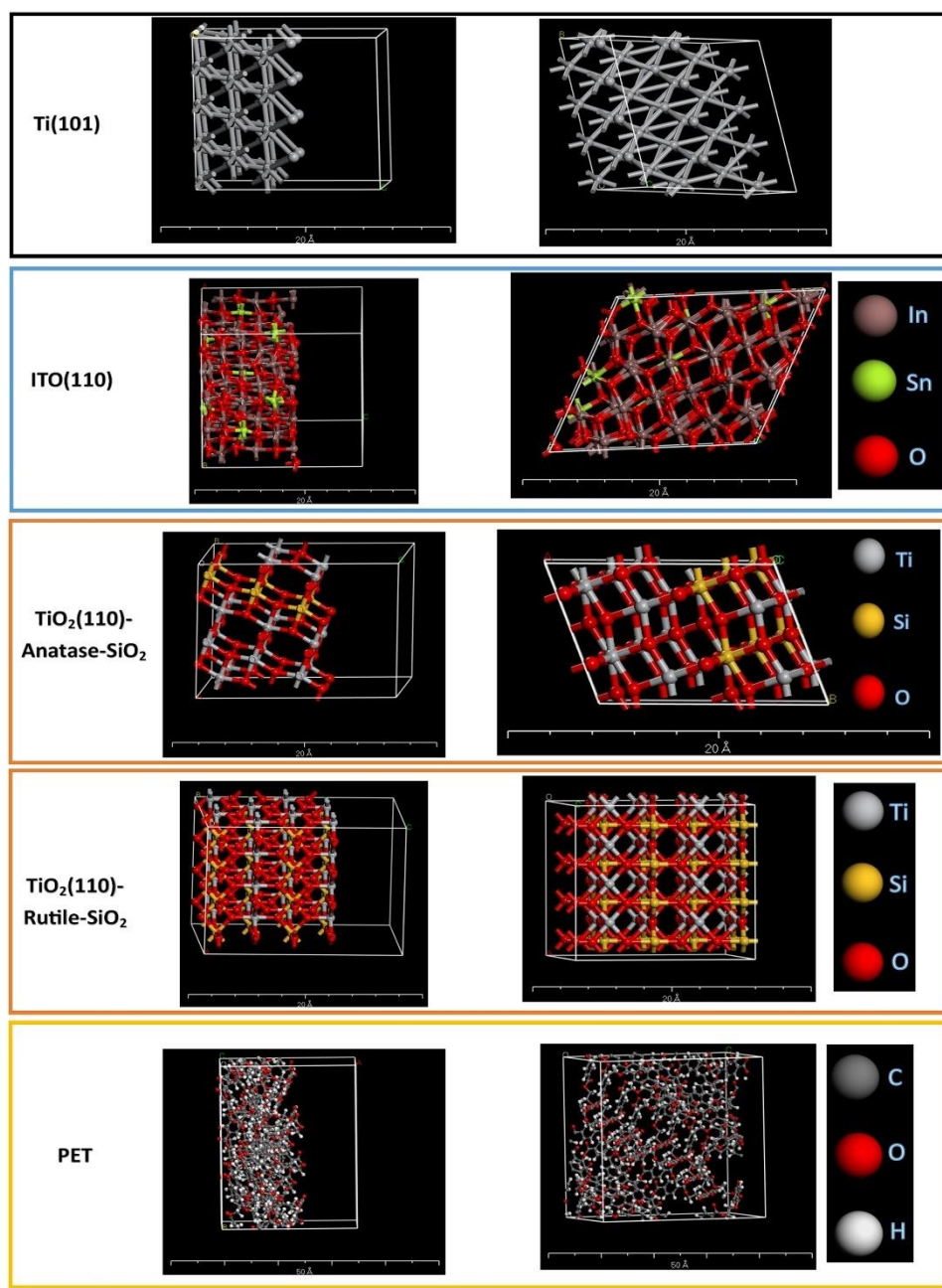


Figure 3. The models constructed for the DOS simulation.

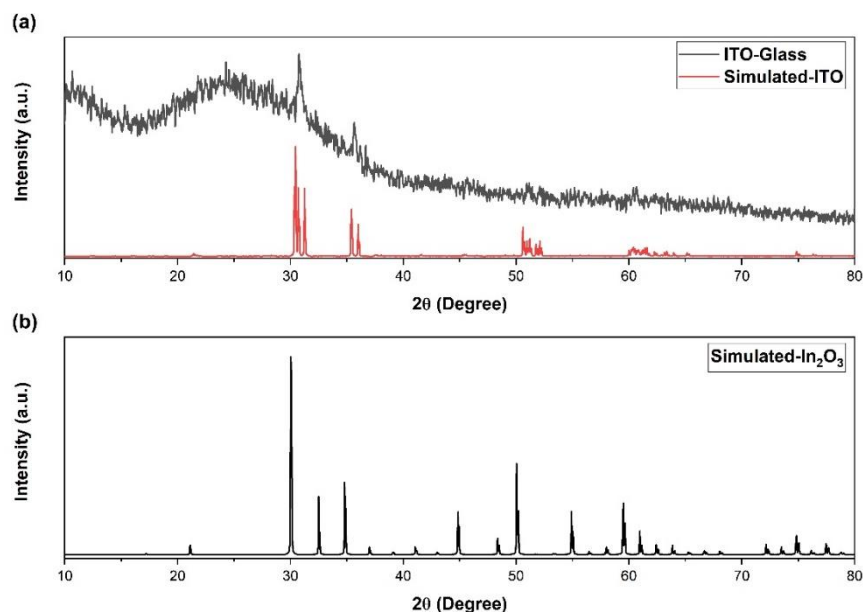


Figure 4. a) Simulated XRD of the ITO and measured XRD of ITO-Glass catalyst, (b) Simulated XRD of In_2O_3 .

3.4 Photocatalytic CO_2 reduction tests and measurement of products

Experiments on PCO_2R were conducted in both batch and continuous systems. In the batch system, a piece of catalyst film with the desired size was placed in the headspace of a three-way quartz reactor with a total capacity of 250 ml. Next, 10 ml of deionized water was added to the reactor. The reactor was then sealed firmly using rubber septums. Following this, CO_2 gas was purged into the reactor for 30 min in a dark atmosphere. The reactor was then kept in the dark for a further 30 min. Before light irradiation, a headspace sample was collected and the composition of the gas was determined using GC-FID and GC-TCD. The light source in the PCO_2R experiment was six UV-light bulbs (Philips Germicidal Ozone UV Quartz Glass UVC Bulb: 16 W) with a UV light intensity of $0.187 \text{ mW}\cdot\text{cm}^{-2}$ and a visible light intensity of $0.444 \text{ mW}\cdot\text{cm}^{-2}$. The UV and visible light intensities were obtained using a SOLAR LIGHT radiometer model PMA2200 equipped with UV and visible light sensors. The catalytic film received no further treatment all through the stability tests other than being taken out of the reactor and allowed to air dry.

The identical reactor configuration was employed in the flow system. The CO_2 gas bubbled in a water saturator outside the reactor, and the humid gas was supplied into

the reactor, with the reaction products collected in an accumulator outside the reactor. The gas samples' composition was determined using GC-FID and GC-TCD.

Three control experiments were carried out to confirm that CO and CH₄ evolved from CO₂: (i) an experiment with catalyst, CO₂, and water but no light illumination; (ii) an experiment with CO₂, water, and light illumination but no catalyst; and (iii) an experiment with water, catalyst, light illumination, and Helium gas rather than CO₂. In the control experiments, no significant amounts of CH₄ were detected.

GC-FID (Shimadzu, GC-14A) and GC-TCD (Shimadzu, 2014C) were used to determine the composition of the PCO₂R products, as stated earlier. Methane concentration was measured using GC-FID using the following conditions: Packed column: Shincarbon ST; carrier gas: He (HP grade, 99.99 vol%); make-up gas: air (UHP grade, 100 vol%); column temperature: 70 °C; injector temperature: 150 °C; detector temperature: 150 °C; analysis time: 10 min. Carbon monoxide and hydrogen concentrations were measured using GC-TCD with the following parameters: packed column: Shincarbon ST; carrier gas: argon (HP grade, 99.99 vol%); column temperature: 50 °C; injector temperature: 100 °C; detector temperature: 120 °C; analysis time: 10 min.

CHAPTER IV:

RESULTS AND DISCUSSION

The discussion and results are organized into three sections. In the first section, experimental results and simulations of AM-TiO₂-SiO₂/ITO-PET surface phenomena in PCO₂R are presented. In the second section, the effect of substrate conductivity on AM-TiO₂-SiO₂ and P25-SiO₂ for water vapor PCO₂R will be presented. PCO₂R on ITO-Glass and ITO-PET will be discussed using both experiment and DFT modeling in the last section.

4.1 PCO₂R on the AM-TiO₂-SiO₂/ITO-PET

4.1.1 Yields of produced CH₄, CO, and H₂ in PCO₂R in water vapor

The yields of PCO₂R products in the batch system, water vapor, and two cycles are presented in Figure 5. The yield of products in the first cycle and after 4 hr of reaction were 1×10^6 , 1.26×10^6 , and 2.42×10^6 nmol/gr_{cat} for CH₄, H₂, and CO, respectively. In the second cycle, Figure 5 (a) and (b) show a decrease in the yield of produced CH₄ and H₂, but the yield of CO is nearly constant. The reused AM-TiO₂-SiO₂/ITO-PET gas production behavior demonstrates the existence of two simultaneous reaction pathways since after the catalyst was employed once, CH₄ and H₂ gas production is obviously impacted, although CO production is essentially unaffected. After the catalyst has been employed once, the CH₄ and H₂ mechanism was constrained. The decrease in production rate in crystalline TiO₂ catalysts is mostly ascribed to blockage by surface water layers [84,85], molecular competitive adsorption on adsorption sites [86], and the loss of the equilibrium between radical consumption and absorption on the surface [87–89]. The decrease in CH₄ and H₂ gas generation in our PCO₂R system with an AM-TiO₂ catalyst may be ascribed to certain target molecules(T-M) having a high affinity for Si(O₂)⁻² groups (on the AM-TiO₂ surface), whilst other T-M will have a higher affinity for the AM-TiO₂ surface (surface lacking Si(O₂)⁻² groups). As a result, molecules that are affine to certain

zones can act as blockings when UV light radiation stops because they may be embedded by second-order linkages due to their proximity to the surface. When the PCO₂R process is complete and the catalyst returns to its initial condition, the intermolecular forces (Van der Waals and hydrogen bonds) would be solidified.

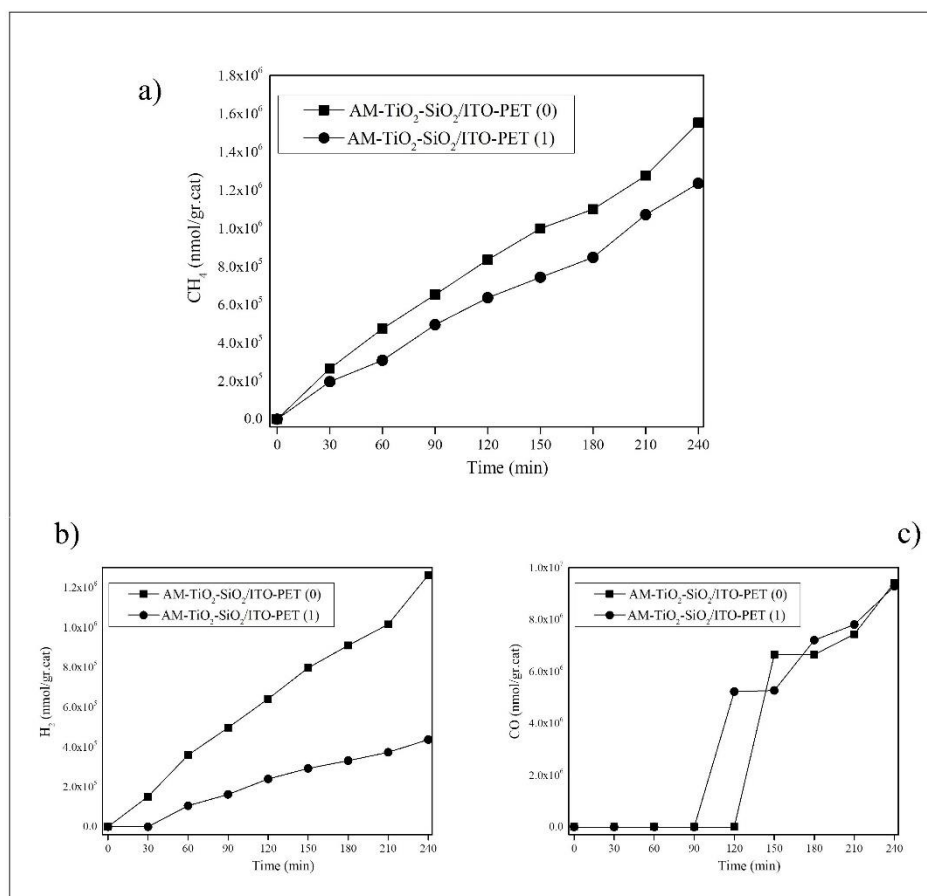


Figure 5. The yield of produced (a) CH₄, (b) H₂, and (c) CO.

4.1.2 Characterization

4.1.2.1 XRD

The XRD pattern of AM-TiO₂ and AM-TiO₂-SiO₂ are presented in Figure 6. The distinct signal locates around $2\theta = 25^\circ$ indicates that both materials display XRD patterns similar to TiO₂ amorphous materials. The signal is associated with the TiO₂ anatase phase's [101] plane [85,90]. After studying the AM-TiO₂ unit cell, Prasai et al.

2012 [91] concluded that the majority of Ti and O atoms typically had six and three coordinates, respectively. The XRD patterns don't exhibit any signs of SiO₂-induced morphologic change. The AM-TiO₂-SiO₂ and AM-TiO₂ XRD patterns imply that the atomic arrangement of AM-TiO₂-SiO₂/ITO-PET is a combination of various atomic arrangements since it doesn't have a well-defined crystallinity.

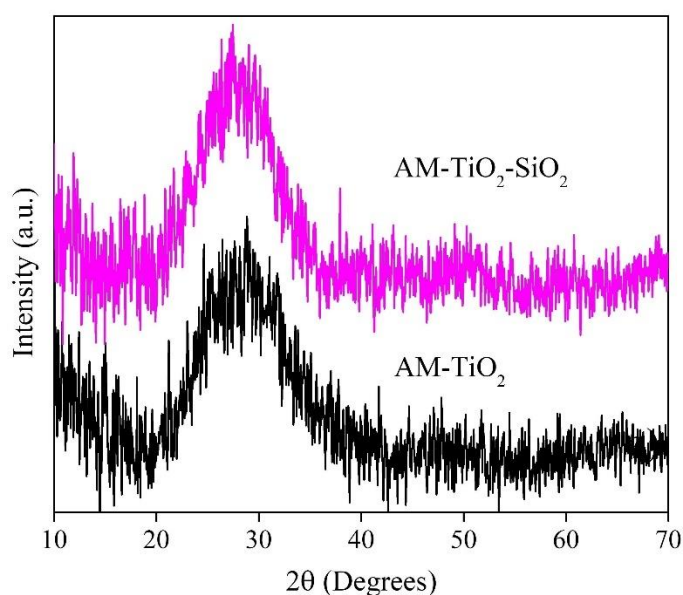


Figure 6. XRD patterns of AM-TiO₂, and AM-TiO₂-SiO₂.

4.1.2.1 Raman spectrum of the catalyst

The RAMAN spectra of AM-TiO₂ and AM-TiO₂-SiO₂ are shown in Figure 7. The 166 cm⁻¹ and 604 cm⁻¹ signals, which are typical of AM-TiO₂, are related to the symmetric stretching vibration of Ti-O-Ti in AM-TiO₂. The peak at 2939 cm⁻¹ is a part of a triplet signal that is attributed to the isopropoxy groups' CH bond (i-Pro). The i-Pro signal occurs as a result of the drying procedure (below 182 °C)[92,93]. The low SiO₂ load, lack of SiO₂ agglomeration, and high SiO₂ dispersion within AM-TiO₂ can be used as explanations for the absence of SiO₂ signals in AM-TiO₂-SiO₂ RAMAN spectra. According to other studies, the photocatalytic activity increased when SiO₂ agglomerations were absent [60]. The silanol groups (Si-O-H) and silicate ions (Si-O⁻) that are generated as a result of the silicon dioxide groups (Si(O₂)⁻²) connected to the oxygen atoms on the TiO₂ surface are related to surface active sites.

However, there are two different ways that the $\text{Si}(\text{O}_2)^{-2}$ groups might bind to the surface (*Figure 8*): first, by forming formal bonds between the silicate ions and Ti atoms; second, by forming hydrogen bonds between the silanol groups and OH-Ti surface groups. Therefore, the low SiO_2 load and high dispersion of these groups on the surface might prevent $\text{Si}(\text{O}_2)^{-2}$ groups from becoming embedded and promote the PCO_2R process.

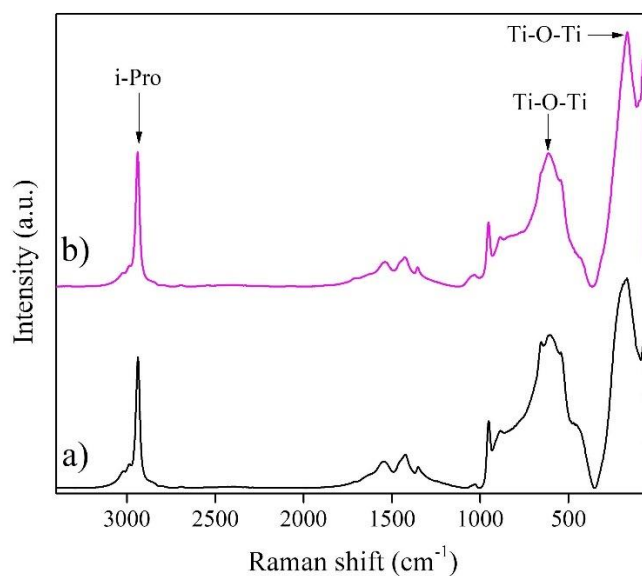


Figure 7. Raman spectra of (a) AM-TiO₂, and (b) AM-TiO₂-SiO₂.

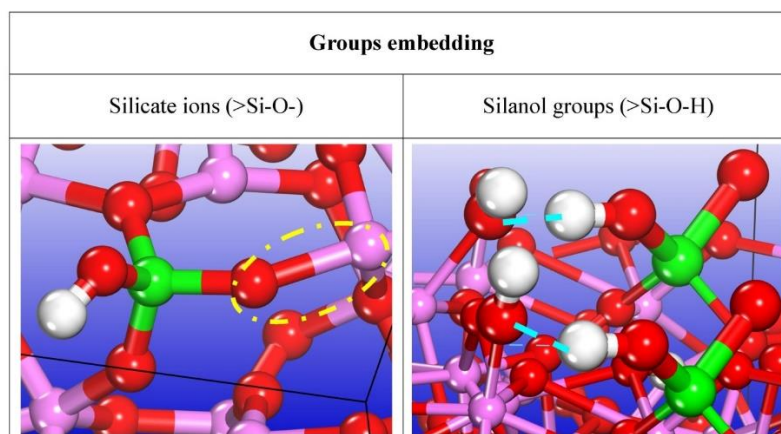


Figure 8. Embedded silicate ions and silanol groups on the AM-TiO₂ surface.

4.1.2.3 FTIR spectrum of AM-TiO₂-SiO₂/ITO-PET

The FTIR spectrum of the AM-TiO₂-SiO₂/ITO-PET film is shown in *Figure 9*. The FTIR spectrum is overloaded with overlapping signals that are hard to distinguish. Due to the amorphous nature of TiO₂, the support (ITO-PET), and i-Pro, the spectrum is crowded. However, a broad absorption band associated with Ti-O bonding may be seen in the range of 500 cm⁻¹ to 900 cm⁻¹. Additionally, the band (900-1300 cm⁻¹) attributed to the longitudinal optical (LO) and transverse optical (TO) absorptions associated with the Si-O bonds in the tetrahedral network related to agglomerations is absent[94].

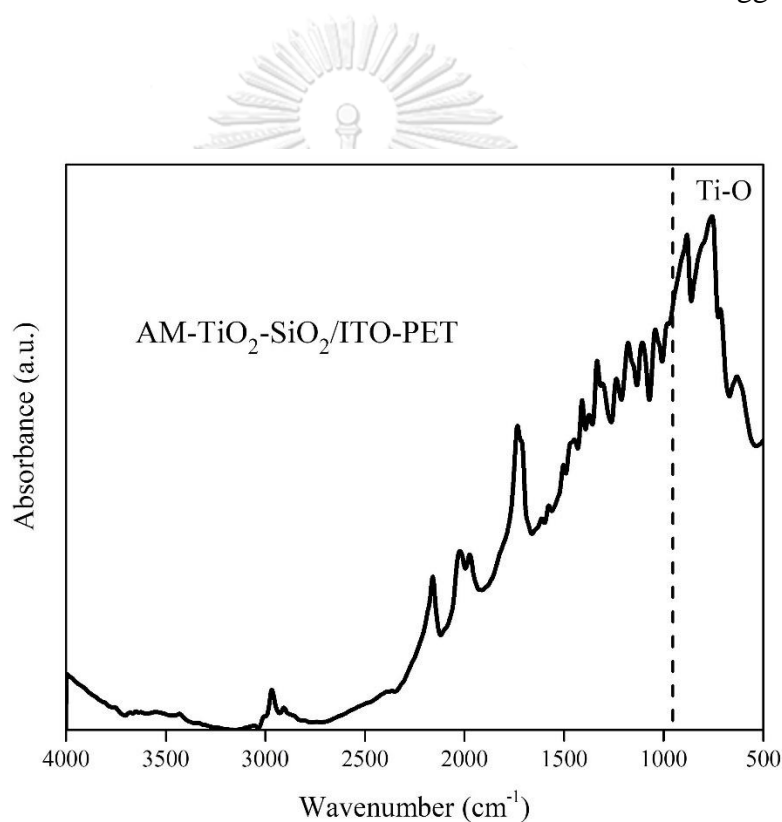


Figure 9. FTIR spectrum of AM-TiO₂-SiO₂/ITO-PET

4.1.2.4 Photoluminescence spectroscopy (PL)

Through its investigation of charge carrier trapping, photoluminescence spectroscopy (PL) is used to examine the surface characteristics of catalysts. The PL emission is caused by the recombination of electron-hole pairs in the surface and bulk of the catalyst. Surface chemistry has a significant effect on the TiO₂ PL. Furthermore, it has been shown that AM-TiO₂ lacks fluorescence emission [87]. Due to the effect of ITO-

PET support, the AM-TiO₂-SiO₂/ITO-PET spectrum (*Figure 10*) displays a greater emission signal at 365 nm (3.4 eV). The PL emission spectra of AM-TiO₂ and AM-TiO₂-SiO₂ materials are shown in *Figure 10*-inset. While the other signals are ascribed to deep traps, the emission signal at 396 nm is attributed to radiative band-to-band recombination. Due to the low load and good dispersion of SiO₂, the morphological characterization (XRD, Raman, and FTIR) did not show the impact of SiO₂ on the catalyst. The AM-TiO₂-SiO₂ PL spectrum, however, shows the SiO₂ effect. Lower photogenerated charge carrier recombination rates are related to declining PL intensity in AM-TiO₂-SiO₂ [95].

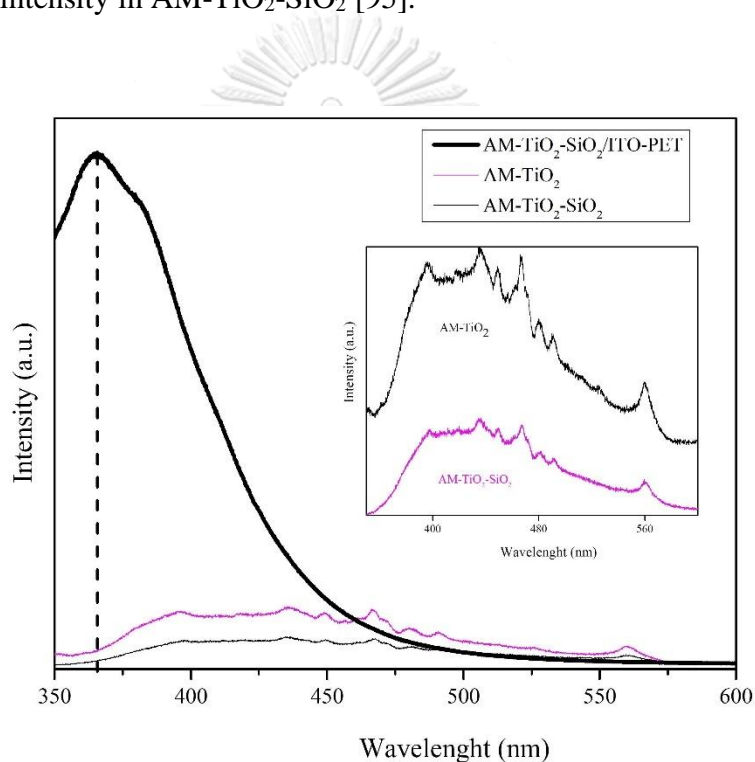


Figure 10. AM-TiO₂-SiO₂/ITO-PET PL spectrum. The PL emission spectra of AM-TiO₂ and AM-TiO₂-SiO₂ powders are shown in the inset.

4.1.2.5 UV-Vis DRS and band gap estimation

Using the UV-Vis DRS data (*Figure 11* (a)), the optical band gaps (E_g) of AM-TiO₂-SiO₂ and AM-TiO₂-SiO₂/ITO-PET were computed. The E_g was calculated by graphing $(\alpha h\nu)^2$ against $h\nu$ [96]. (*Figure 11* (b)). *Figure 11* demonstrates that both samples mostly absorb UV light. AM-TiO₂-SiO₂ powder and the AM-TiO₂-SiO₂/ITO-PET film show a similar band gap of 3.24 eV.

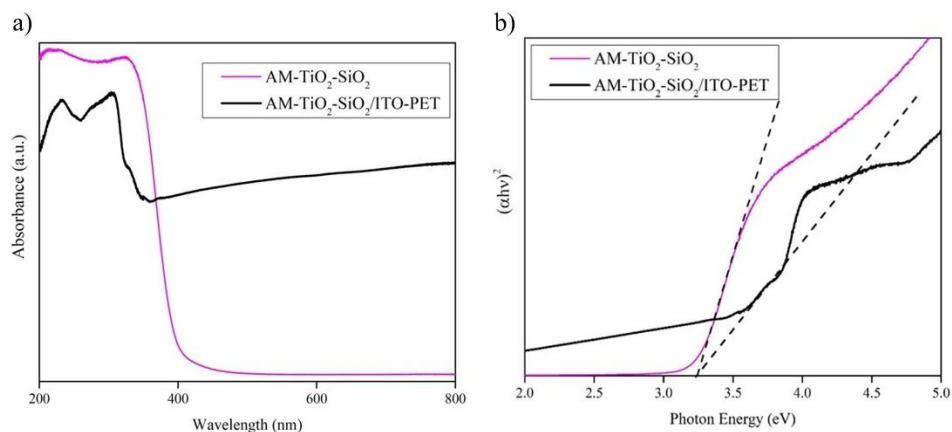


Figure 11. a) UV-Vis DRS, and b) Tauc's plot of AM-TiO₂-SiO₂ powder and AM-TiO₂-SiO₂/ITO-PET film.

4.1.2.6 EDX elemental mapping of AM-TiO₂-SiO₂/ITO-PET catalyst

EDX elemental mapping of the prepared film is presented in Figure 12. The formation of the film is confirmed by this analysis.

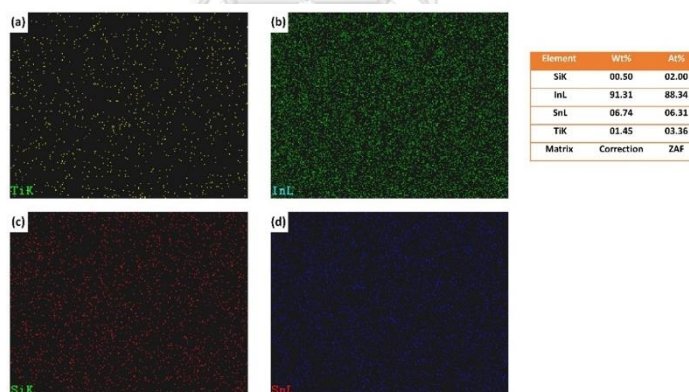


Figure 12. EDX elemental mapping shows the presence of (a) Ti, (b) In, (c) Si, and (d) Sn.

4.1.3 Affinity trends by MD simulation

The MD is an effective tool for comprehending systems with complex adsorption dynamics and systems where there is a significant competitive relationship between physisorption and chemisorption [97,98]. Media (such as aqueous, acidic, or basic), catalytic surfaces, functional groups on the surfaces (such as OH groups, and SiO₂

groups), reactants, products, and by-products can all be included in the systems that are evaluated using MD. The specific binding density values of the systems can be estimated using MD. Van der Waals and hydrogen bonds combine to provide the systems' specific binding density, which can be used to define affinity tendencies, such as the surfaces' affinity for attraction and attachment[99]. To create AM-TiO₂ unit cells using the melt-quench method, the XRD spectrum of AM-TiO₂ was a key guideline. The AM-TiO₂ unit cell used in this investigation demonstrated the highest degree of consistency with the experimental XRD spectrum. Experimental estimates by Y. Shiraishi et al. 2005 [100] of the diffusion distance of hydroxyl radicals ([•]OH) revealed that it is around 1.3–2.4 nm; molecules outside of the [•]OH reach range (1.3–2.4 nm) would not react with [•]OH. This suggests that the radical anion of CO₂ ([•]CO₂⁻) may have a reach range comparable to that of [•]OH (1.3-2.4 nm) and that the catalyst-medium contact may be restricted to 2.4 nm (24 Å) in light of these findings. Therefore, the simulation boxes were built with a≈c axis of 28 Å (catalyst surface and medium) to study a hypothetical catalyst-medium contact of 24 Å. H₂O, CO₂, HCOOH, HCOH, CH₃OH, CH₄, and CO are some of the potential molecules involved in PCO₂R as reagents, products, and by-products[54,101]. The PCO₂R mechanism on TiO₂ surfaces (whether anatase, rutile, or amorphous) has not yet been fully identified. In this way, the catalyst-medium interface of AM-TiO₂-SiO₂/ITO-PET may be studied using a binding density calculation and simulation boxes including molecules that potentially make up the reaction media (H₂O, CO₂, HCOOH, HCOH, CH₃OH, CH₄, and CO). Since CH₃OH was not detected in this work, the target molecules (T-M) in this analysis are CO₂, HCOOH, HCOH, CH₄, and CO.

AM-TiO₂, AM-TiO₂ low load of SiO₂ (AM-TiO₂-LLSiO₂), and AM-TiO₂ high load of SiO₂ (AM-TiO₂-HLSiO₂) were the surfaces utilized in the simulation boxes (to investigate AM-TiO₂-SiO₂/ITO-PET attracting or attaching behavior (*Figure 13*)).

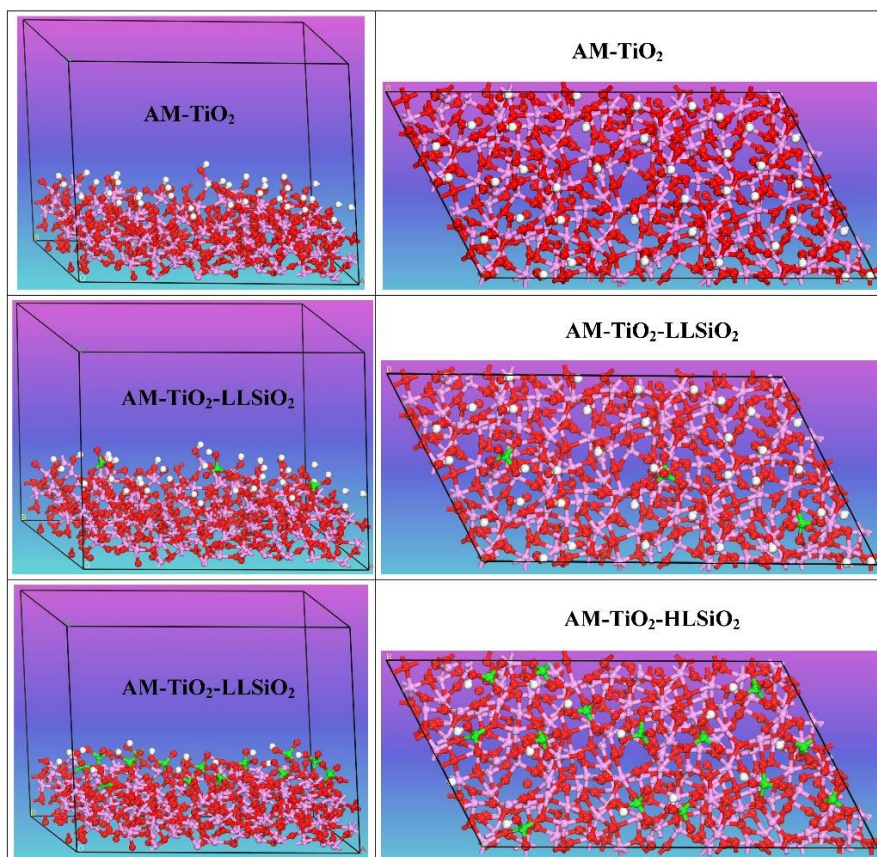


Figure 13. AM-TiO₂, AM-TiO₂-LLSiO₂, and AM-TiO₂-HLSiO₂ simulation boxes. The following colors indicate the atoms: H-white, O-red, Ti-pink, and Si-green.

The exposed surface of AM-TiO₂ was hydroxylated, the exposed surface of AM-TiO₂-LLSiO₂ was hydroxylated and modified with a small number of Si(O₂)⁻² groups, and the exposed surface of AM-TiO₂-HLSiO₂ was solely modified with a large number of Si(O₂)⁻² groups. According to the AM-TiO₂-SiO₂ material characterization (section 4.2), it can be determined that the catalytic surfaces in AM-TiO₂-SiO₂/ITO-PET are similar to simulation boxes of AM-TiO₂ and AM-TiO₂-LLSiO₂ because Si(O₂)⁻² signals are unnoticeable (due to the dispersion and low load of the Si(O₂)⁻² groups on the surface). AM-TiO₂-HLSiO₂ was added, however, to examine the impact of the high loading of Si(O₂)⁻². Since some surfaces are more affine to H₂O molecules, the trend of surface affinity is directly affected by the H₂O in the medium. This water attraction results in high-affinity energies for water-based media. To detect the H₂O impacts in the media, low and high-humidity theoretical systems were executed.

Error! Reference source not found. details the molecular compositions of the media.

Table 1. Composition of simulated media

T-M	Medium	Molecule loads	
		Mx	H ₂ O
CO ₂	Low humidity	75	25
HCOOH	Low humidity	75	25
HCOH	Low humidity	75	25
CH ₃ OH	Low humidity	75	25
CH ₄	Low humidity	75	25
CO	Low humidity	75	25
CO ₂	High humidity	25	75
HCOOH	High humidity	25	75
HCOH	High humidity	25	75
CH ₃ OH	High humidity	25	75
CH ₄	High humidity	25	75
CO	High humidity	25	75

The binding energy (E_{binding}), which is determined by the MD of simulation boxes, serves as a quantitative measure of the specific binding density. At equilibrium conditions, the E_{binding} of the systems AM-TiO₂/medium, AM-TiO₂-LLSiO₂/medium, and AM-TiO₂-HLSiO₂/medium was estimated [50]. The interaction energy ($E_{\text{interaction}}$) was first estimated using the formula shown in **Equation (2)** [102]:

$$E_{\text{interaction}} = E_{\text{T}} - (E_{\text{surface}} + E_{\text{T-M}}) \quad \text{Equation (2)}$$

E_{T} is the total energy of the system surface/T-M/H₂O, E_{surface} is the total energy of the (hydroxylated and/or modified) surfaces, and $E_{\text{T-M}}$ is the total energy of the medium (T-M/H₂O). E_{binding} is the negative value of the $E_{\text{interaction}}$ (Equation (3)):

$$E_{\text{binding}} = - (E_{\text{interaction}}) \quad \text{Equation (3)}$$

Figure 14 displays the E_{binding} values of the AM-TiO₂, AM-TiO₂-LLSiO₂, and AM-TiO₂-HLSiO₂ systems at high humidity. Negative E_{binding} values indicate that there is

no affinity between the surfaces and aqueous media. For all high-humidity mediums, the E_{binding} values of AM-TiO₂ and AM-TiO₂-HLSiO₂ systems are positive. However, AM-TiO₂-LLSiO₂ is significantly anti-affine with respect to the aqueous media, particularly when HCOH and CO molecules are present. It is evident that the amount of Si(O₂)⁻² groups on the AM-TiO₂ surface considerably modifies the surface affinity. The E_{binding} values of AM-TiO₂-LLSiO₂ and AM-TiO₂-HLSiO₂ demonstrate that the surface affinity depends not only on the variety of surface groups but also on the amount of these groups that are dispersed on the surface.

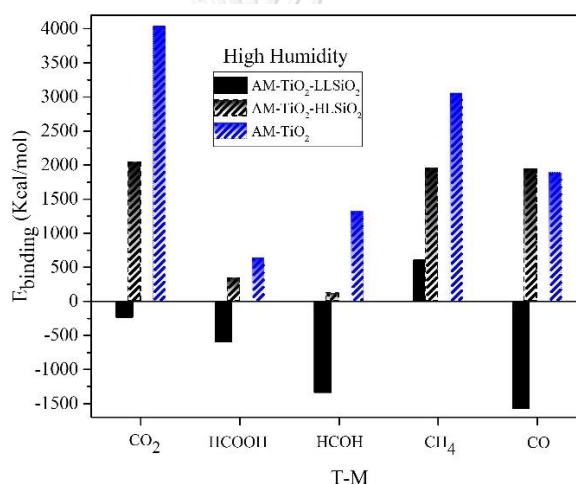


Figure 14. E_{binding} in the high-humid medium.

Figure 15 shows the E_{binding} of AM-TiO₂, AM-TiO₂-LLSiO₂, and AM-TiO₂-HLSiO₂ in low humidity conditions. For the majority of the T-M, the low humidity systems display positive values. The strong affinity that the AM-TiO₂ surface has for all T-M molecules may be attributed to the high rate of reaction. The E_{binding} values of AM-TiO₂ (low humidity with CO molecules) also show that due to the high surface affinity (4734.587 Kcal/mol), CO molecules generated on the surface would take longer to overcome the surface attraction and release into the medium.

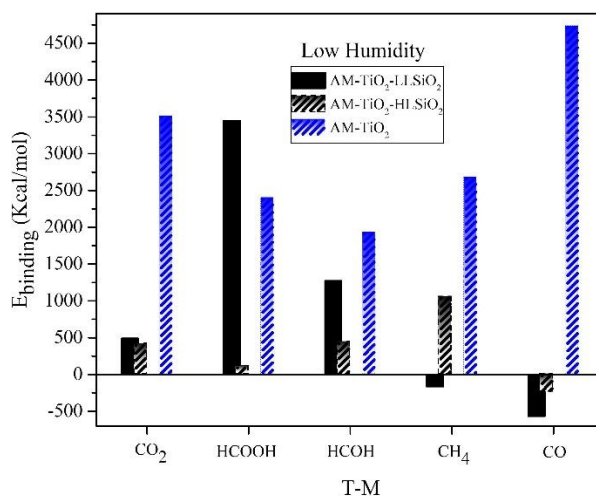


Figure 15. E_{binding} in the low-humid medium.

Two zones might be used to conduct the photoreduction of CH₄, H₂, and CO. In the second stage of the catalytic process, when the concentration of T-M is high, the simulation boxes for zone 1 (Z1) and zone 2 (Z2) are shown in Figure 16. Because the T-M with high affinity will be anchored on the surface by intermolecular interactions (Van der Waals and Hydrogen bonds) and solidified after the photoreduction process is complete, it is possible to assess the T-M molecules that may obstruct the reaction processes at this point (meaning when the catalyst returns to its fundamental state). Due to the high E_{binding} values of 4734.587 Kcal/mol and 3511.027 Kcal/mol, respectively, the reaction mechanism in Z1 could be inhibited primarily by CO and CO₂ molecules. In contrast, the Z2 mechanism route is mostly inhibited by HCOOH and HCOH molecules, whose E_{binding} values are 3446.635 and 1275.937 Kcal/mol, respectively. The experimental results (Section 4.1.1) imply that there are two PCO₂R routes, one occurring in Z1 and the other in Z2. After a single use of the photocatalyst, the reactions on Z2 may be impeded by HCOOH and HCOH molecules fixed on the surface. The MD analysis indicates that the production of CH₄ can be attributed to Z2 because Z2 exhibits a negative E_{binding} value toward CH₄ (-169.041 Kcal/mol); these negative values imply that the CH₄ molecules formed on the surface of AM-TiO₂-LLSiO₂ will not continue to react and will be readily released into the medium. These values indicated that the generated molecules on the AM-TiO₂ surface will react actively till the generation of the CO molecule. Z1 displays strong E_{binding} positive values toward all T-M. However, due to the surface affinity

of AM-TiO₂ ($E_{\text{binding}} = 4734.587$ Kcal/mol), the CO molecules may aggregate at the surface; the molecules won't be released to the medium until AM-TiO₂ reaches CO saturation.

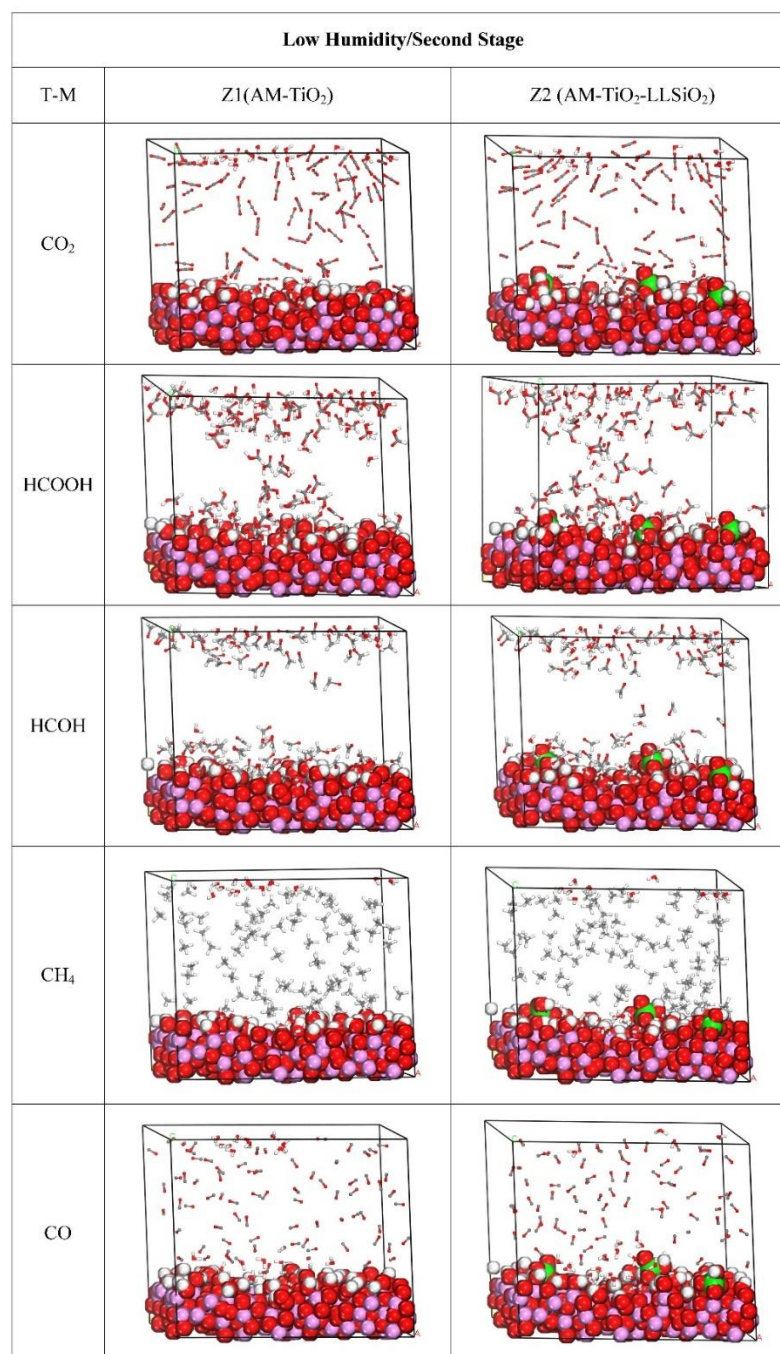


Figure 16. Low humidity simulation medium boxes for AM-TiO₂ and AM-TiO₂-LLSiO₂. C-gray, H-white, O-red, Ti-pink, and Si-green are the colors used to symbolize the atoms.

4.1.4 Simulated PCO₂R mechanism of AM-TiO₂-SiO₂/ITO-PET catalyst

The creation of CO on AM-TiO₂-SiO₂/ITO-PET may be carried out primarily by AM-TiO₂ because the electronic structure of Z1 is more kinetically favorable to produce CO, as shown by the evidence in *Figure 17*. Two locations simultaneously enhance the connection of the $\cdot\text{CO}_2^-$ radical due to the particular disordered arrangement of the AM-TiO₂ surface (Inset of *Figure 17*). The main mechanism is seen in *Figure 18* (a) on Z1, where photoreduction routes of CO₂ to get CO will be made simpler and quicker by the association of surface Ti atoms with C/O atoms of CO₂. Contrary to the crystalline surfaces of TiO₂, the AM-TiO₂ allows for the participation of two Ti atoms in the binding of the $\cdot\text{CO}_2^-$ radical. Following the production of CO, the molecule will be desorbed off the surface, leaving one oxygen there to wait for H⁺, which will either form OH \cdot with one H⁺ or water with two H⁺. The chemical routes to generate CH₄ on Z1 were also studied (*Figure 18*); however, this process is constrained by an energy barrier of 1.92 eV (*Figure 17*) between AM-VI and AM-VII. This transition can be explained by the fact that O atoms are more conducive to $\cdot\text{CH}_3$ production than Ti atoms.

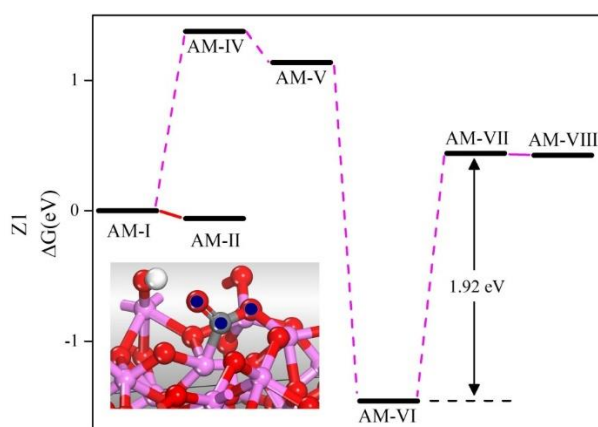


Figure 17. The ΔG profile of AM-TiO₂ catalyst. C-gray, H-white, O-red, and Ti-pink are the colors that depict the atoms.

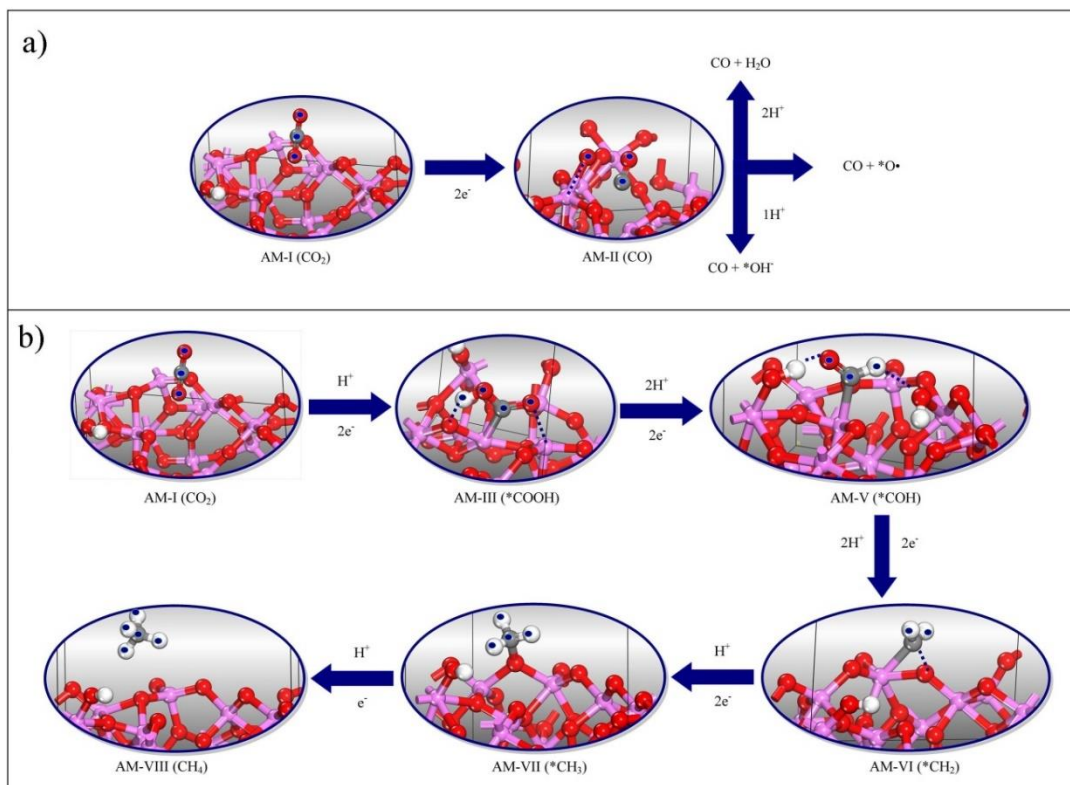


Figure 18. The proposed reaction pathway of the Z1. C-gray, H-white, O-red, and Ti-pink are the colors that represent the atoms.

The more kinetically efficient mechanism to produce CH_4 on Z2 is shown in Figure 19. This process is constrained by a 1.32 eV energy barrier between AM-SiO₂-V/AM-SiO₂-VI and AM-VII. The fundamental distinction between the states AM-SiO₂-V and AM-SiO₂-VI, which are connected to $\cdot\text{COH}$, is in the second-order forces that can be inferred. If $\cdot\text{COH}$ is close to $\cdot\text{OH}$, a hydrogen bond will form, but if it is close to Ti atoms, a van der Waals force will prevail. The transition from AM-SiO₂-V/AM-SiO₂-VI to AM-SiO₂-VII will need additional energy since $\cdot\text{COH}$'s oxygen double bond must be broken. This transition will also be facilitated by forces of the second order (Van der Waals and hydrogen bonds) (Figure 20). The majority of Z2's mechanism is aided by second-order links.

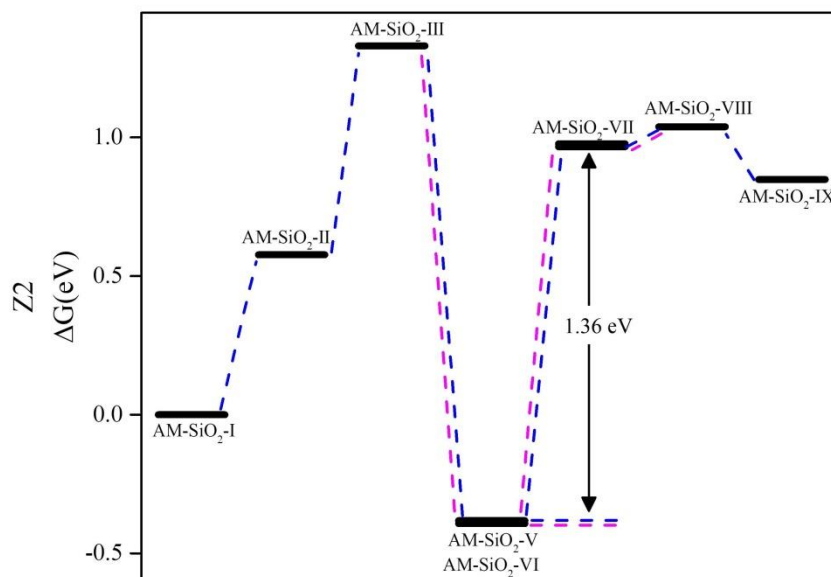


Figure 19. The ΔG profile of Z2.

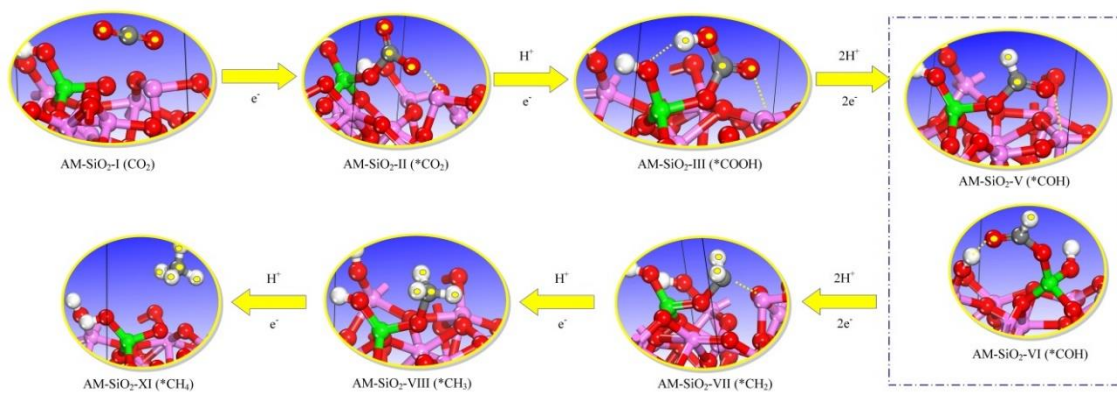


Figure 20. The proposed reaction pathway of the Z2. C-gray, H-white, O-red, Si-green, and Ti-pink are the colors that represent the atoms.

4.2 effect of substrate conductivity on AM-TiO₂-SiO₂ and P25-SiO₂ for water vapor PCO₂R

4.2.1 Characterization

4.2.1.1 XRD and FTIR

In *Figure 21* (a), the XRD patterns of AM-TiO₂-SiO₂ and P25-SiO₂ are displayed. In the XRD pattern of AM-TiO₂-SiO₂, only one wide peak could be identified, and neither the diffraction peaks associated with crystalline TiO₂ nor SiO₂ are present [103,104]. This verifies that both TiO₂ and SiO₂ exist in an amorphous phase. Moreover, the XRD pattern of P25-SiO₂ is in good accordance with the patterns in JCPDS Nos. 88-1175 (anatase) and 84-1286 (rutile), respectively[105–109]. Moreover, there is no SiO₂ peak (JCPDS Nos. 46-1045)[110] in the XRD pattern of P25-SiO₂ that might be associated with the amorphous structure of SiO₂ in this sample.

By using FTIR analysis, the existence of functional groups in the prepared catalysts was investigated, and the resulting spectra are displayed in *Figure 21* (b). Broad absorption bands for Ti-O-Ti, Si-O-Si, and Ti-O-Si stretches are present in both catalysts between 500 and 900 cm⁻¹[111–115]. Additionally, the O-H bending for Ti-OH, Si-OH, and water could be the cause of the absorption peaks at about 1630 cm⁻¹[116]. The stretching vibration of OH in surface-adsorbed water could be attributed to the broad bands over 3100 cm⁻¹ in both catalysts[112]. The chemicals used in the synthesis of catalysts may be the source of the other peaks in the spectra.



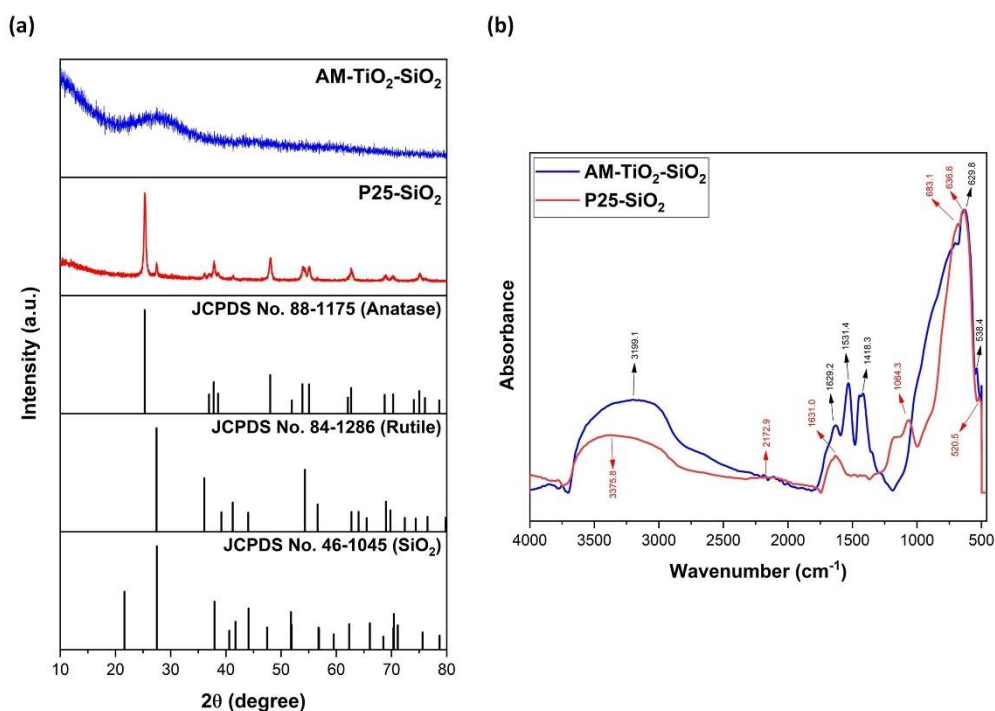


Figure 21. a) AM-TiO₂-SiO₂ and P25-SiO₂ XRD patterns, b) AM-TiO₂-SiO₂ and P25-SiO₂ FTIR spectra

4.2.1.2 UV-Vis DRS, Band gap, and band edge position

Figure 22 (a) depicts the UV-DRS spectra of AM-TiO₂-SiO₂ and P25-SiO₂. Each of the two catalysts exhibits considerable UV absorption intensities. Moreover, the band gap of AM-TiO₂-SiO₂ and P25-SiO₂ was calculated to be 2.93 eV utilizing Tauc's plot with an indirect transition procedure (Figure 22 (c)) [117]. The electrochemical method was employed to determine the flat-band potentials in order to further examine the catalyst's relative band structure. Using either the AM-TiO₂-SiO₂ or P25-SiO₂ spin-coated on ITO-glass, the electrochemical impedance measurements were carried out using an Autolab(R) model M280 fitted with a FRA module in a three-electrode cell. In addition, the flat-band potential of ITO-PET was also determined. As counter and reference electrodes, respectively, platinized titanium mesh and Ag/AgCl (KCl 3 M) were utilized. The solution was maintained at pH = 7 using a phosphate buffer of 0.1M concentration, and measurements were conducted between 1.1 and -1.1 V with a sinusoidal perturbation of 10 mV in the frequency range of 1kHz to 1Hz. Using Equation (4), the potentials recorded at pH= 7 by the Ag/AgCl

reference electrode were converted to the NHE (normal hydrogen electrode) scale at pH= 0.

$$E_{\text{RHE}} = E_{\text{Electrode}} + E_{\text{Ag/AgCl}} + 0.059 \text{ pH} \quad \text{Equation (4)}$$

$E_{\text{Electrode}}$ is the potential of the working electrode, $E_{\text{Ag/AgCl}}$ is the potential of the reference electrode, and E_{RHE} stands for relative hydrogen electrode potential[118]. In *Figure 22 (b)*, the Mott-Schottky plot is depicted. All catalysts' Mott-Schottky graphs show the characteristic positive slopes of n-type semiconductors[119]. Additionally, the computed band gaps were used to identify the valence band (VB) edges. In *Figure 22 (d)*, the energy levels are shown. Both oxidation and reduction of water over the catalysts are confirmed to be thermodynamically viable because for both catalysts, the CB edges are more negative than the typical reduction potential of a proton and the VB edges are more positive than the oxidation potential of water. Despite having a lesser potential for water oxidation, the AM-TiO₂-SiO₂ catalyst has a larger reduction potential than the P25-SiO₂. According to the CB position of ITO-PET, if the photocatalysts and ITO-PET (substrate) are in proper contact, excited electrons in the CB of the photocatalysts may be transferred to the CB of ITO-PET.

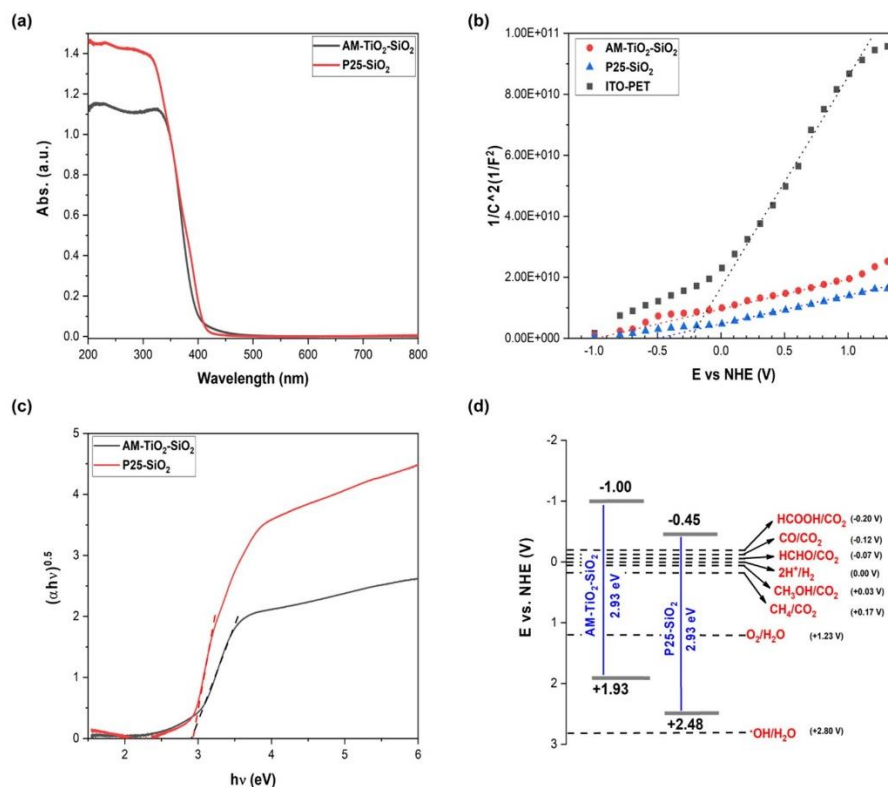


Figure 22. (a) UV-vis diffuse reflectance spectra of AM-TiO₂-SiO₂ and P25-SiO₂, (b) Mott-Schottky plots of AM-TiO₂-SiO₂, P25-SiO₂, and ITO-PET obtained at different frequencies, (c) Tauc's plot of the AM-TiO₂-SiO₂ and P25-SiO₂ catalysts, (d) The band edge positions of the AM-TiO₂-SiO₂ and P25-SiO₂ catalysts with respect to the water oxidation and reduction potentials.

4.2.1.3 Photoluminescence (PL) analysis

Separation and transfer of light-induced charge carriers are key aspects in defining the photocatalytic activity of the CO₂ reduction catalyst [120]. In this regard, steady-state photoluminescence (PL) spectroscopy was performed at an excitation wavelength of 325 nm; the findings are depicted in Figure 23. Figure 23 (a) depicts emission peaks at around 420 nm for both catalysts, which may be associated with the radiative recombination of electrons from the CB into holes in the VB. In addition, AM-TiO₂-SiO₂ contains an excitonic PL peak in the emission band 396 nm that may be associated with trapped defects above the CB edge, whereas P25-SiO₂ lacks this unique excitonic PL peak. Furthermore, the PL spectra of both catalysts contain several peaks above 425 nm, which may be the result of shallow and deep exciton traps [121,122]. The PL spectra of the catalysts were also recorded on various

substrates, and the resultant PL spectra are shown in *Figure 23* (b)-(c). The PL spectrum of P25-SiO₂ on Ti substrate exhibits a similar pattern to that of its powder, although with a change in intensity. Although the PL spectrum of AM-TiO₂-SiO₂ on the Ti substrate has a similar pattern to the powder's PL above the emission wavelength of 400 nm with a difference in intensity, emission peaks with high intensities below 400 nm are seen in *Figure 23* (b) that are absent in the powder's PL (*Figure 23* (a)). These emission peaks in the 350–400 nm region are attributed to radiative recombination from defect traps at energies greater than the AM-TiO₂-SiO₂ CB edge. The ITO-PET substrate itself, as well as the PL spectra of the catalyst-deposited films on it, are shown in *Figure 23* (c). All spectra showed two emission peaks at 365 and 382 nm, which are ascribed to the near band-edge emission of SnO₂ and In₂O₃, respectively[65]. Additionally, two bands at around 370 and 400 nm that were created by the C=O bond can be seen in the PL spectrum of the PET (*Figure 23* (d)), and the PL pattern of the AM-TiO₂-SiO₂ is similar to the PL pattern of the PET with a slight increase in intensity at about 400 nm. As an indication of the transition between the substrate and the P25-SiO₂ layer, the PL pattern of the P25-SiO₂-PET film (*Figure 23* (d)) differs from the PL pattern of the PET substrate. The light may excite both the substrate and the catalyst, according to the PL measurements shown in *Figure 23*.

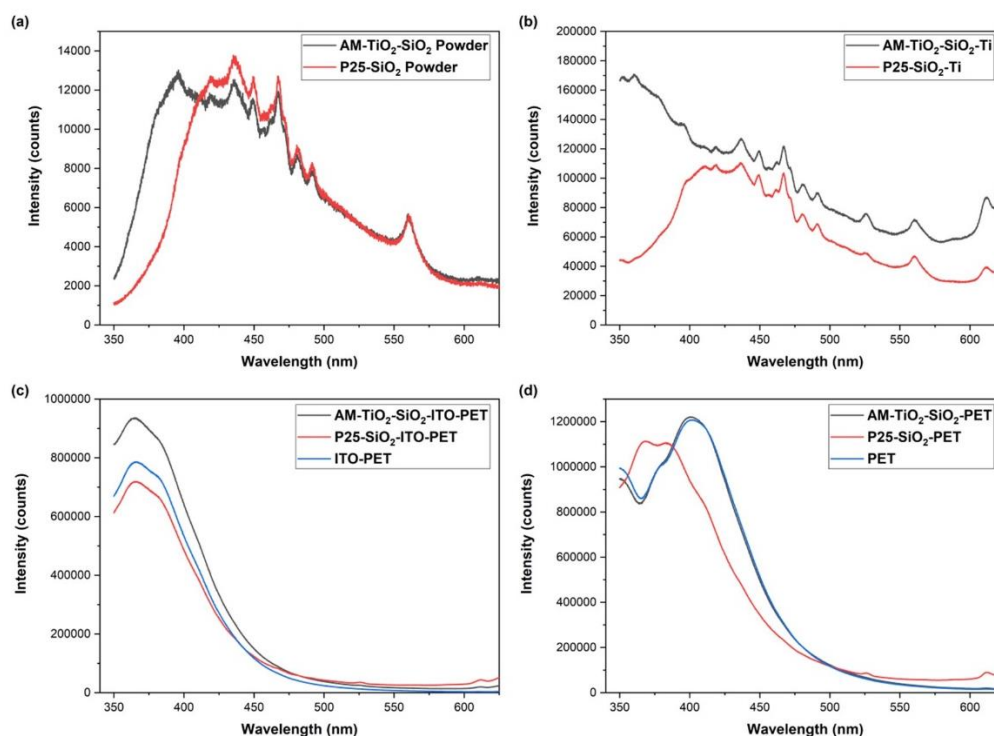


Figure 23. PL spectra of a) AM-TiO₂-SiO₂ and P25-SiO₂ powders, b) Catalysts on Ti substrate, c) ITO-PET substrate and catalyst films on the substrate, and d) PET substrate and catalyst film on the substrate.

4.2.1.4 Cyclic voltammetry and relation between the divergence from Mott-Schottky behavior and the dynamics of trapping and untrapping

We concentrated on the potential range where the surface capacitance deviates from the Mott-Schottky analytical linearity in order to better study the dynamics of the electron-traps on the catalyst surfaces. This divergence results from the "Trapping" of the electron by the surface energy levels within the forbidden zone, which happens when the surface is reduced and the Fermi level is pinched [123,124]. In Figure 24 (a), a deviation from linearity for $1/C^2$ begins at -0.07V Vs NHE, which is the potential region where a redox pair appears in the Cyclic voltammetry. Since no species in the solution can accept this electron at this potential, this redox process is attributed to the trapping and de-trapping signals. The sharp oxidation signal present between -0.6 and -0.7V is attributed to the transfer of electrons from the conduction band to the surface; the separation between this signal and the trapping one (-0.07V)

indicates that the conduction band and the trap have well-defined energy edges, meaning that there is no movement from the trap to the conduction band, forcing the electrons to be transferred to the solution or recombining from that lower energy level. In *Figure 24* (b), a more subtle deviation from the Mott-Schokty linearity is observed beginning at 0.09 V. In this case, a redox process is still present, but a more capacitive behavior of the electrode was observed. This behavior and the absence of a sharp signal between -0.6 and -0.7 V imply a more even distribution of the accumulated charge on the surface, as opposed to a few sites.

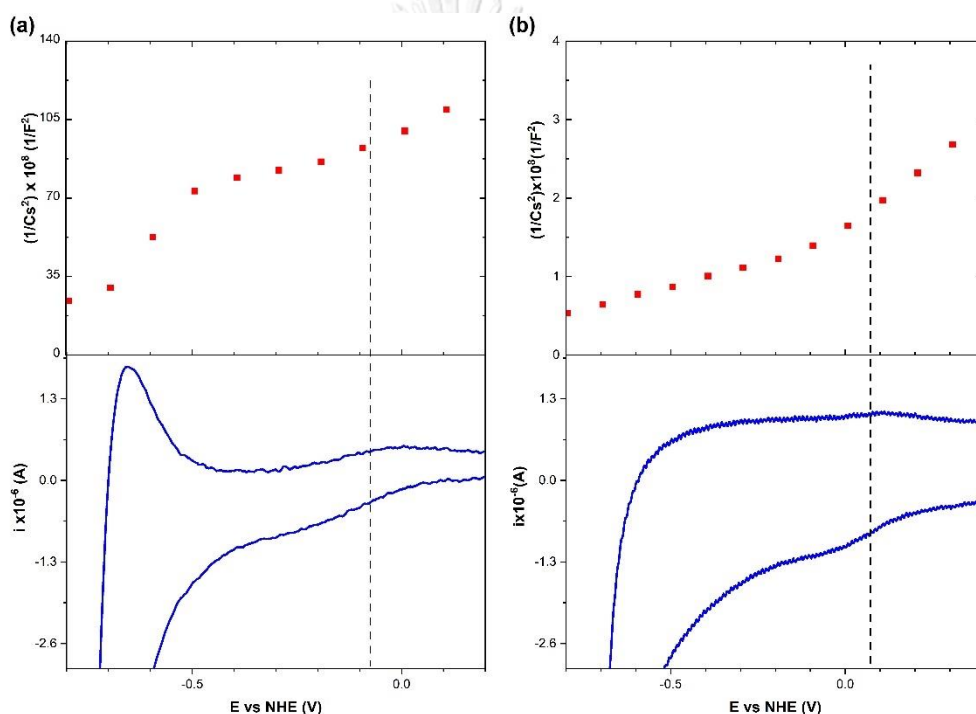


Figure 24. Mott-Schottky behavior divergence and trapping/untrapping dynamics by surface states for (a) P25-SiO₂-ITO-PET, and (b) AM-TiO₂-SiO₂-ITO-PET.

4.2.1.5 SEM/EDAX analysis of AM-TiO₂-SiO₂ and P25-SiO₂ catalysts

According to the SEM element mapping of the catalysts depicted in *Figure 25*, the component elements are evenly distributed. Carbon concentration is particularly low when low-temperature heat treatment is considered for catalyst synthesis (as shown in the inset tables in *Figure 25*).

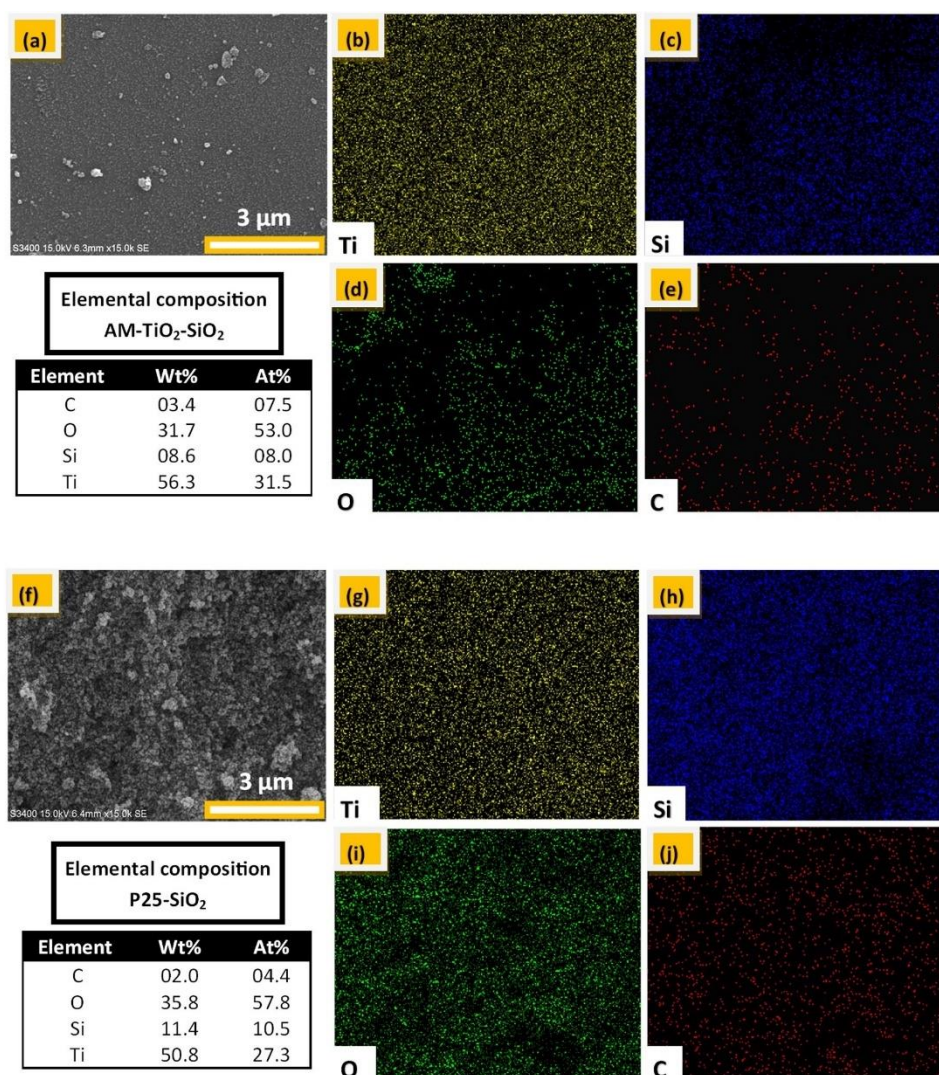


Figure 25. (a) – (e) SEM/EDAX images of AM-TiO₂-SiO₂, and (f) – (j) SEM/EDAX images of P25-SiO₂.

4.2.1.6 XPS analysis of synthesized AM-TiO₂-SiO₂ and P25-SiO₂ photocatalysts

The chemical states of the components in the produced photocatalysts were investigated using X-ray photoelectron spectroscopy, and the results are shown in Figure 26. The two peaks at 459.2 eV (Ti 2p_{3/2}) and 465.0 eV (Ti 2p_{1/2}) in the XPS spectra of Ti 2p in the AM-TiO₂-SiO₂ catalyst (Figure 26 (a)) show the presence of Ti⁴⁺[125,126]. The Ti XPS spectra in the P25-SiO₂ catalyst was also deconvoluted using the same method, yielding two peaks at 459.5 eV (Ti 2p_{3/2}) and 465.2 eV (Ti 2p_{1/2}) (Figure 26 (b))[127,128]. As a result, the oxidation state of Ti⁴⁺ in both catalysts was verified. Additionally, four peaks were fitted to the O 1s spectra of both

catalysts; the results are given in *Figure 26* (c) and (d). The overlapping oxygen contributions from Ti, Si, and surface hydroxide make the deconvolution of O 1s spectra more complex. The O 1s spectra of the two catalysts show four distinctive O 1s peaks. Strongly bonded oxygen atoms to Ti are responsible for the peak at about 530.5 eV, while the oxygen atom attached to Si is responsible for the peak at around 532.2 eV. The Si-O-Ti bond is thought to be responsible for the unresolved shoulder peak at around 531.5 eV[129–131]. Additionally, the surface hydroxyl groups are responsible for the peak at about 533.5 eV[132]. Additionally, a peak at around 103 eV that represents the Si-O-Si bond was fitted to the Si 2p XPS spectrum[133,134].

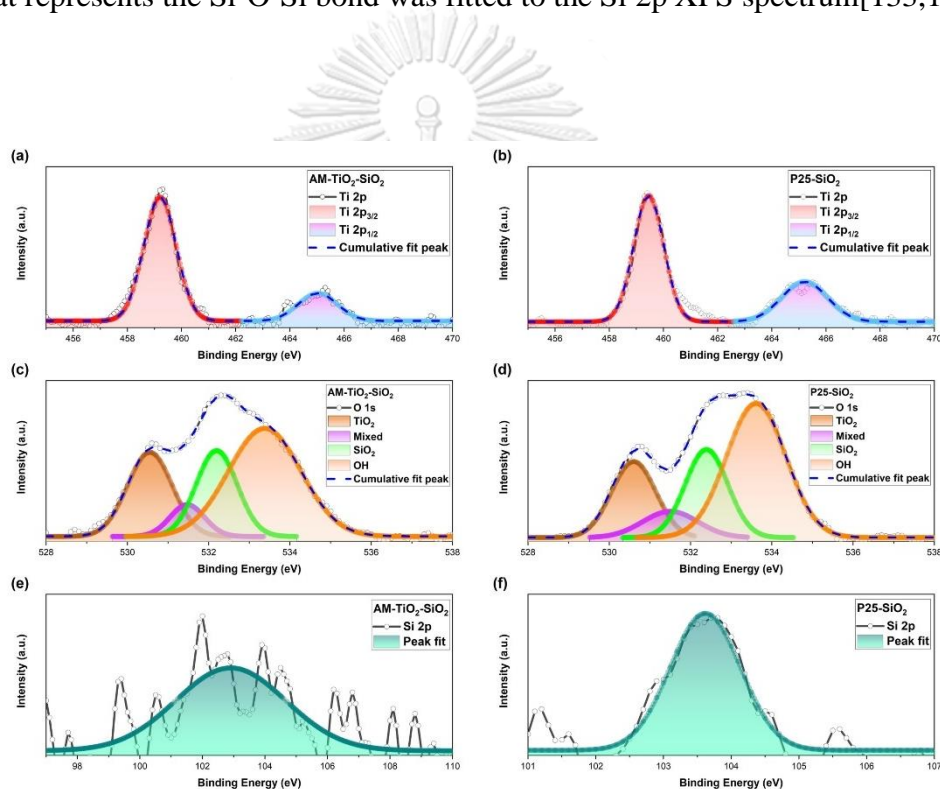


Figure 26. High-resolution XPS spectrum of Ti 2p, Si 2p, and O 1s in both AM-TiO₂-SiO₂ and P25-SiO₂ catalysts.

4.2.1.7 Open circuit potential decay (OCPD) and KPFM analysis

Using a commercial 1.75 ml R/T/A spectro-electrochemical cell (Redox.me) with a Pt wire as the counter electrode, Ag/AgCl as the reference electrode, and the catalyst film as the working electrode, OCPD measurements were carried out to determine the stability of the photo-generated electrons. A 1000W Xe Lamp was used to light the sample until the open circuit potential was steady (30 min). After then, the light was

turned off, and the open circuit potential was monitored until it stabilized (in the dark) (30 min). The findings are shown in *Figure 27*, where E_{FB} refers to the flat band potential, E_{eq} is the equilibrium potential, and E_{OCP} stands for the open circuit potential. The tests were conducted using 0.1M phosphate buffer (pH = 7) saturated with either N_2 or CO_2 . The electron transport is clearly dependent on both the substrate and the reactant in the solution, as seen in *Figure 27*. When CO_2 is present in the solution, electron transfer from AM-TiO₂-SiO₂-ITO-PET occurs more quickly than when the solution is purged with N_2 (*Figure 27* (a)). Unlike AM-TiO₂-SiO₂-ITO-PET, P25-SiO₂-ITO-PET showed quicker electron transfer in the absence of CO_2 (*Figure 27* (b)). In the absence of CO_2 in the solution, both catalysts on the Ti substrate demonstrate quicker electron transfer (*Figure 27* (c) and (d)). In the dark, the open circuit potential (OCP) of P25-SiO₂-Ti was seen to increase. This event may have been induced by the electron transfer from the substrate to the catalyst, which was unique to this catalyst on the Ti substrate. The findings of the KPFM study, which was employed to evaluate the catalysts' work functions, are displayed in *Figure 28* as average work function values, a work function histogram, and three-dimensional work function pictures. Because P25-SiO₂ has a lower gap between the CB energy and fermi level energy than AM-TiO₂-SiO₂, the electron transport from the substrate to the underlying catalyst may be easier. The distribution of the work function for P25-SiO₂ (*Figure 28* (c)) shows that specific parts of the film have lower energy barriers for electron transport from the substrate. In addition, the catalysts' thickness on the substrate was measured to be less than 3 μ m on average, as shown in *Figure 29*.

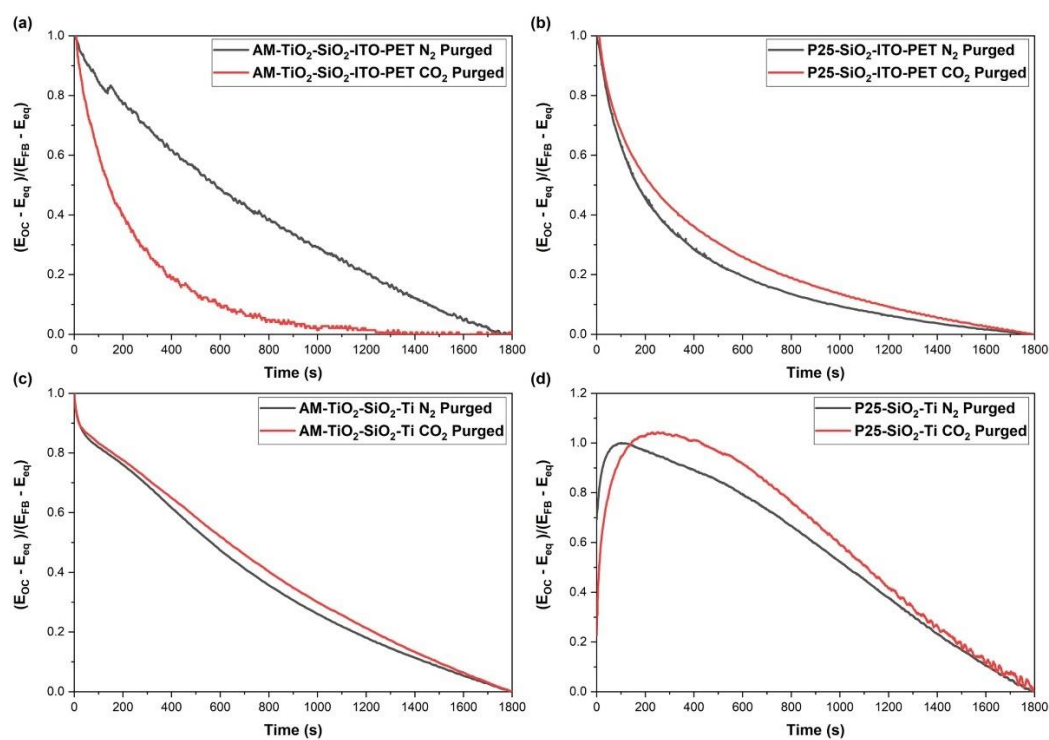


Figure 27. OCPD of AM-TiO₂-SiO₂ and P25-SiO₂ catalyst on ITO-PET and Ti substrates.

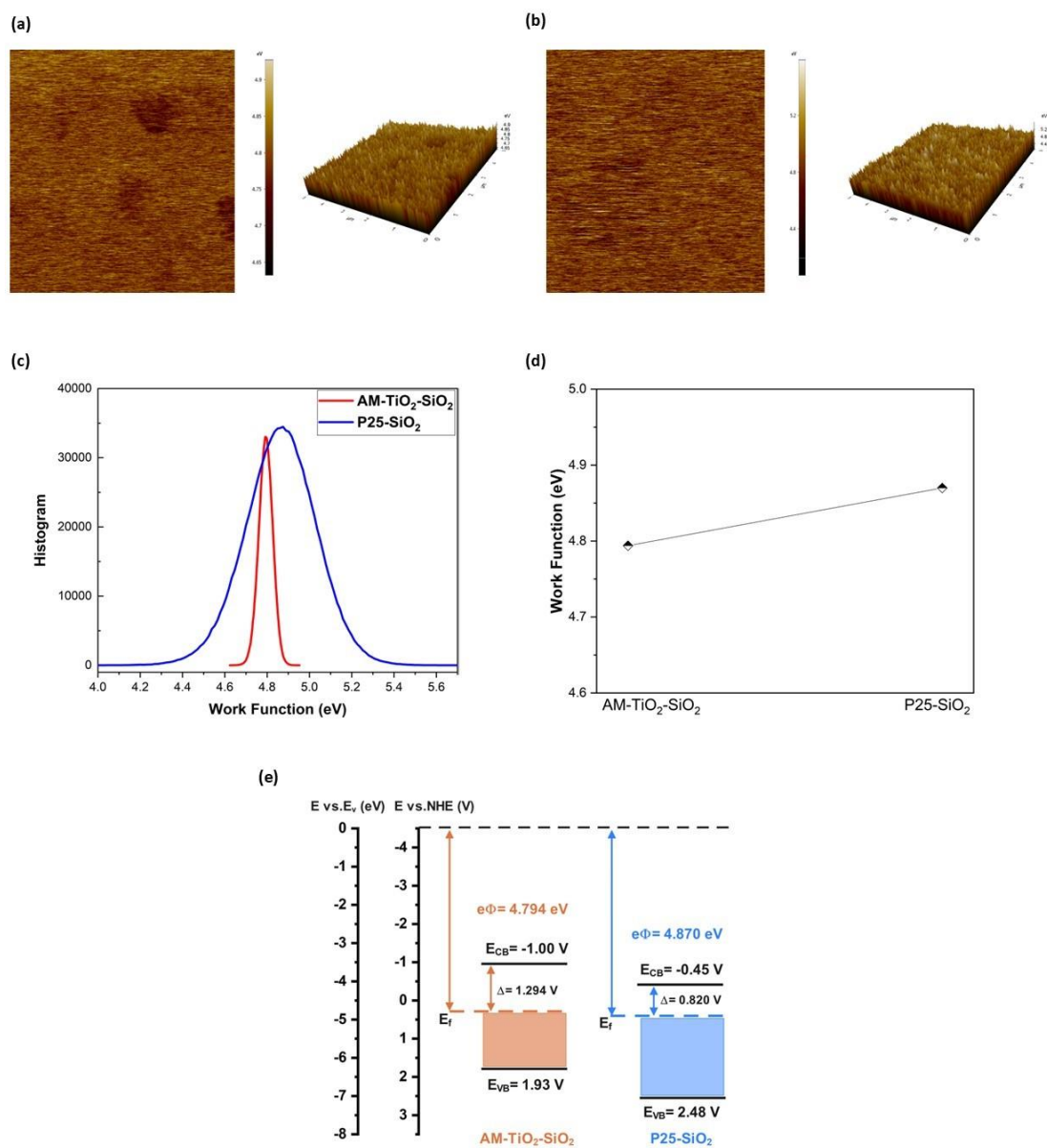


Figure 28. Work function images in 3D for (a) AM-TiO₂-SiO₂, and (b) P25-SiO₂, (c) histogram of work function, (d) average work function, (e) position of fermi level of catalysts (E_v = energy of vacuum, $e\Phi$ = average work function).

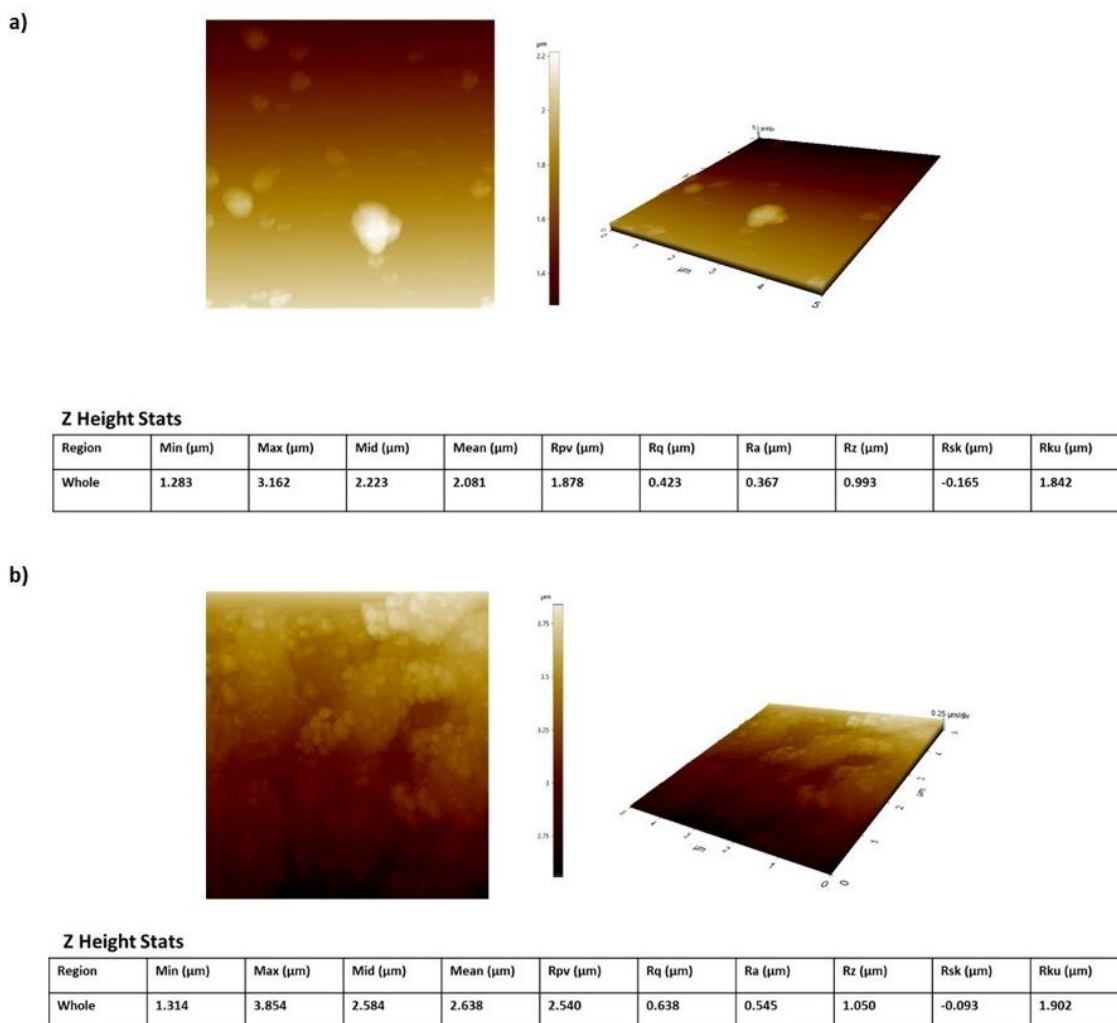


Figure 29. KPFM images and film thickness of a) AM-TiO₂-SiO₂-ITO-PET, and b) P25-SiO₂-ITO-PET.

4.2.2 PCO₂R results for catalysts on different substrates

The yield of products from the photocatalytic CO₂ reduction in the water vapor and batch reactor is depicted in *Figure 30*. According to the findings, catalysts coated on PET substrates had the lowest yield. When the identical catalysts were coated on the ITO-PET substrate, the CH₄ production yield for both catalysts rose. When the Ti substrate was applied, both AM-TiO₂-SiO₂ and P25-SiO₂ exhibited a considerable increase in CH₄ production. In addition to the considerable increase in CH₄ yield, carbon monoxide was detected in the products of the P25-SiO₂ catalyst. AM-TiO₂-

SiO₂ on a Ti substrate exhibited the highest CH₄ selectivity for both catalysts among all substrates. These results show the effect of substrate on the activity and selectivity of photocatalysts for CO₂ reduction. In addition, the stability of the catalysts has been a critical concern in CO₂ reduction. In this regard, the stability of AM-TiO₂-SiO₂ on a Ti substrate was investigated during four CO₂ reduction cycles; the results are depicted in *Figure 30* (c). In the stability test, a reduction in the CH₄ yield after the second cycle could be seen. In this regard, the surface affinity simulation in section 4.1.3 may explain the deactivation cause. In addition, films of P25 and AM-TiO₂ were made on PET and Ti substrates and examined for CO₂ reduction; the findings are provided in *Figure 31*. A similar improvement in production yield over the conductive substrate can be seen. Notably, CO was not detected for either the P25 catalyst or the AM-TiO₂ catalyst. Comparing the findings for P25-Ti and P25-SiO₂-Ti reveals that SiO₂ modification has altered the CO selectivity of the P25 photocatalyst. These findings also reveal that the yield of CH₄ production over AM-TiO₂-SiO₂-Ti is larger than that of AM-TiO₂-Ti, illustrating the influence of SiO₂.

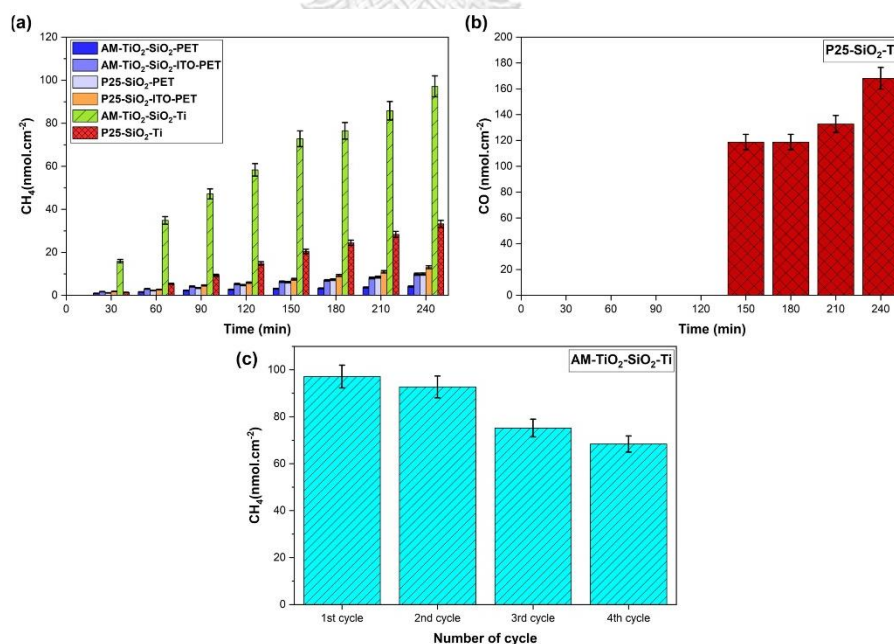


Figure 30. Yields of produced CH₄ and CO for catalysts on different substrates.

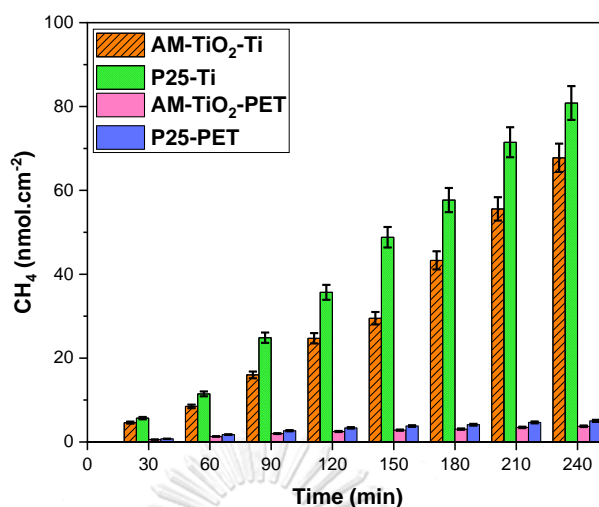


Figure 31. The yield of produced CH_4 for AM-TiO₂ and P25-TiO₂ on different substrates.

4.2.3 Discussion on the effect of various substrates in PCO₂R

By utilizing DFT to calculate the projected density of states (DOSs) of several substrates and catalyst systems, a deeper understanding of the electron transmission mechanism between the catalyst and substrate was attained. The findings are illustrated in Figure 32. Even though the estimated band gaps of the catalysts are smaller than the experimental results, the DOSs calculation was only used in this work to compare the probability of electron transfer between the substrate and the catalyst layer; therefore, this limitation would not impact the discussion regarding electron transfer between the substrate and the catalyst. Individual simulations of anatase and rutile phases modified with SiO₂ were conducted for the P25-SiO₂ catalyst. There are typically two routes for electron transfer at the metal and semiconductor interface: direct and indirect electron transfer (Figure 33). For the effective utilization of hot electrons in plasmonic photochemistry, thermalization and back-transfer processes compete with transfer processes at similar time scales, posing a difficult challenge. As demonstrated in Figure 32 (a) and (b), the Ti substrate exhibits an intense energy state in the middle of the band gap of both SiO₂-modified anatase and rutile. Due to the use of UVC light in photocatalytic tests, the formed hot

electrons may have sufficient energy to be transmitted either directly or indirectly to the CB of the overlayer catalysts. In addition to surface plasmons, the transferred electrons from the catalyst to the substrate may be excited back to the energy levels in the CB of the catalyst and used in the CO₂ reduction reaction (*Figure 33*). ITO is a conductive substrate, and similar to Ti, its DOSs have a continuous band structure (*Figure 32 (c) and (d)*). In this instance, the hot electrons may possess sufficient energy to transfer to the CB of the overlayered catalysts. By the experimental findings, the use of conductive substrates (ITO and Ti) increased the photocatalytic activity of the catalysts in comparison to the PET substrate. To compensate for the hot electrons consumed in the CO₂ reduction reaction, the CB of the catalyst could also transfer electrons to the substrate. The conductivity origin of ITO and Ti may explain the difference in the rise of the catalyst's activity in the CO₂ reduction reaction between the two conductive substrates. In contrast to Ti, which has no band gap, ITO has a direct band gap of up to 4 eV when it is deposited on a variety of substrates [135–139]. The defect energy states created by oxygen vacancies and Sn doping are what give ITO its conductivity. It has been demonstrated that O vacancy defects generally serve as electron traps [140,141]. The transferred electrons to the ITO might thus relax in the midgap energy states due to the oxygen vacancies. The electrons from these midgap energy levels would thus require more energy to be excited into the conduction band of the catalysts. Furthermore, the ITO's defects might make it easier for hot holes to thermalize electrons.

The electron-capture ability of PET polymer, in contrast to conductive substrates, may make it difficult for numerous photo-induced electrons to transfer from the catalyst to the substrate. The accumulation of transferred electrons to the PET substrate may create an electric field that prevents electron transmission from the catalyst to the PET substrate [142] due to the limited mobility of electrons in the PET substrate (PET is an almost electrical insulator [143]), and the electrons may be quenched by photo-induced holes (*Figure 33*). In the PL study, the maximum intensity of e⁻/hole recombination was recorded for the catalysts on the PET substrate. The DOSs of the PET is shown in *Figure 32 (e), and (f)*. In addition to non-continuous DOSs, the absence of surface plasmon resonance (SPR) in PET distinguishes PET from the other

two substrates. Therefore, substrates may function as electron collectors that supply electrons to the CB of the overlayers catalysts, where CO_2 reduction occurs.

The potential of each reaction in the CO_2 reaction process is represented in *Figure 33* (f) [144,145]. Following the CB edge position of each catalyst, as depicted in *Figure* (d), the CB edge of AM-TiO₂-SiO₂ is more negative than that of P25-SiO₂; consequently, electrons in the CB of AM-TiO₂-SiO₂ have a higher potential for driving the CO_2 reduction reaction. Comparing the PL spectra of each catalyst on a Ti substrate, as shown in *Figure 23* (b), the intensity of the PL spectrum in the wavelength range of 350 - 400 nm is multiple times greater for AM-TiO₂-SiO₂ than for P25-SiO₂, indicating that more electrons are radiatively recombining from higher energy levels than the CB edge of the catalyst. Higher energy electrons have a greater potential for deriving the CO_2 reduction reaction.

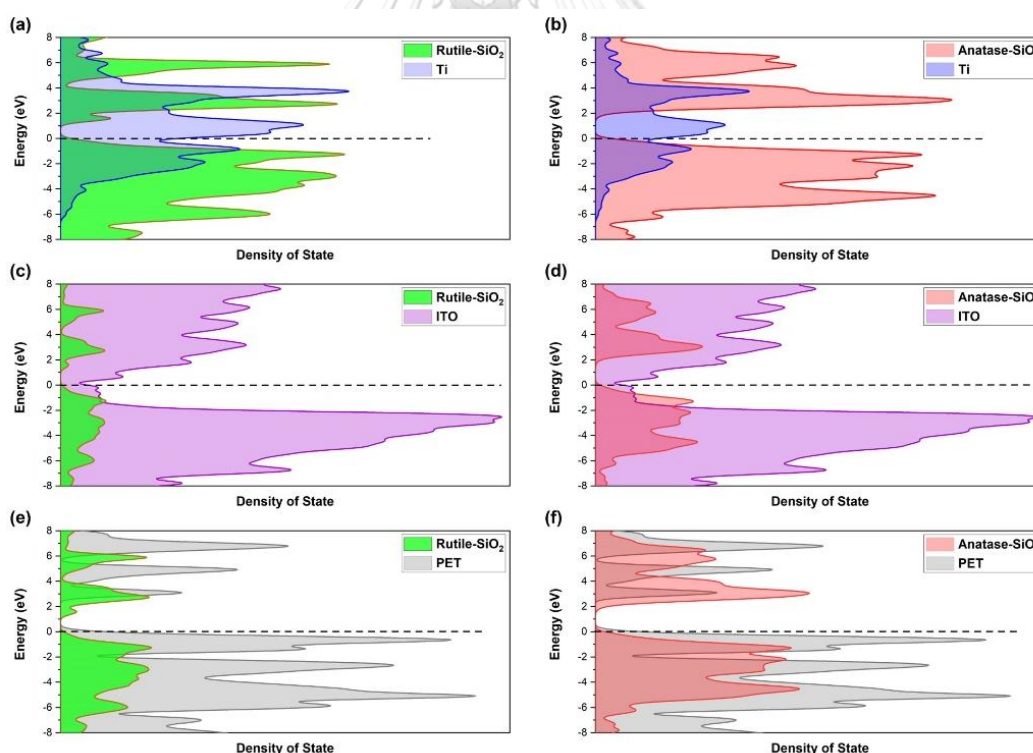


Figure 32. Projected density of states for different catalysts and substrates.

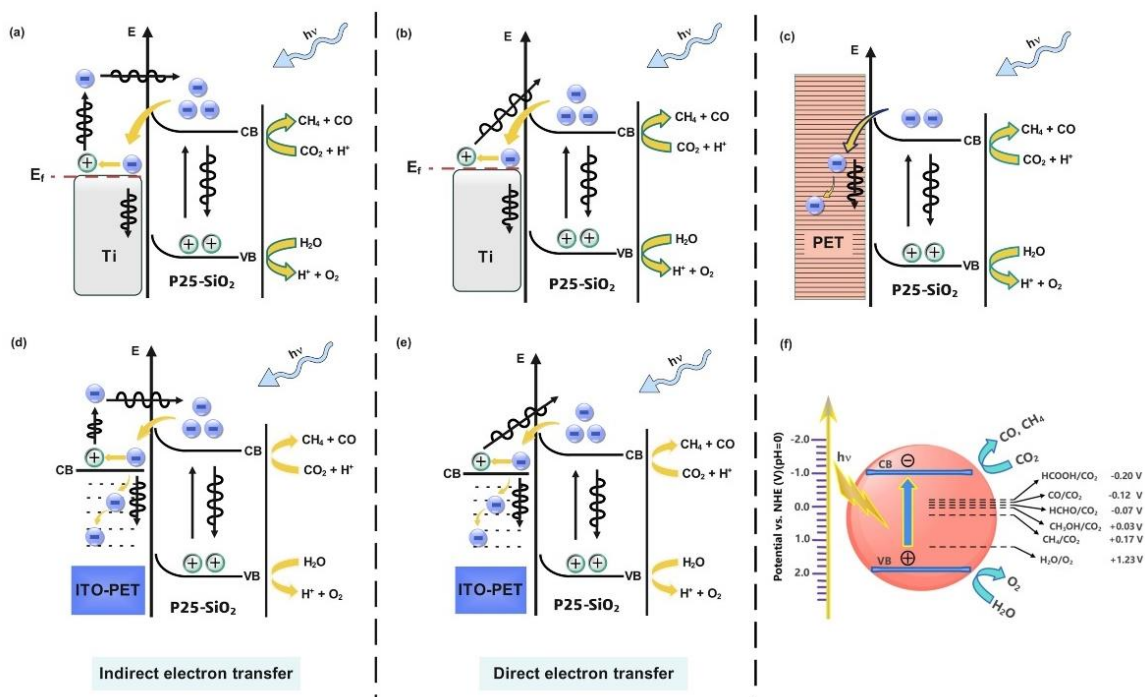


Figure 33. (a) – (e) proposes charge transfer mechanism between substrate and catalyst, (f) schematic representation of CO₂ reduction over photocatalyst.

4.3 Experimental and theoretical study on ITO thin films for PCO₂R

4.3.1 Characterization

4.3.1.1 UV-Vis DRS, PL, and band edge measurement

The catalyst's suitability for the intended reaction depends on the band gap energy and the position of the CB and valence band (VB) with respect to the reduction and oxidation potentials of a particular photocatalytic process. Figure 34 (a) shows the ITO-PET and ITO-Glass films' absorption spectra. Both films, obviously, only absorb in the UV spectrum. The catalysts' optical band gaps were computed using Tauc's relation (Equation (5)):

$$\alpha h\nu = \alpha_0(h\nu - E_g)^{1/2}$$

$$\text{Equation (5)}$$

where $h\nu$ is the energy of a photon, α_0 is a constant, and E_g is the bandgap [135,146,147]. The resulting graph is given in *Figure 34* (a). Therefore, it was calculated that the band gaps of the ITO-PET and ITO-Glass catalysts were 3.90 and 4.20 eV, respectively.

The photoluminescence (PL) spectra of the catalysts were recorded at an excitation wavelength of 300 nm in order to examine the charge transfer process; the resultant graphs are shown in *Figure 34* (b). Both catalysts exhibit a high PL peak at around 370 nm, although the intensity of this peak is substantially lower for ITO-Glass than for ITO-PET, indicating a more efficient $e^-/hole$ separation on ITO-Glass [148]. Section (4.2.1.2) describes the electrochemical impedance measurement setup for determining the CB band edge and the resulting Mott-Schottky plots are illustrated in *Figure 34* (c). One feature of n-type semiconductors is the positive slope in the Mott-Schottky. ITO-Glass has a smaller slope on the Mott-Schottky plot than ITO-PET, which indicates that there are more charge carriers in the ITO-Glass, as can be seen in *Figure 34* (c). Additionally, the Mott-Schottky plot's obtained potentials at pH = 7 by the Ag/AgCl reference electrode were converted to the NHE (normal hydrogen electrode) at pH= 0 [118], and the results are shown in *Figure 34* (d). Notably, the calculated band gap and the conduction band's measured position in *Figure 34* (c) were used to establish the valence band's position (VB). The CB edge is more negative in both catalysts than the proton's reduction potential, and the VB edge is more positive than the water's oxidation potential. Water may be reduced and oxidized over both catalysts, hence this is thermodynamically possible.

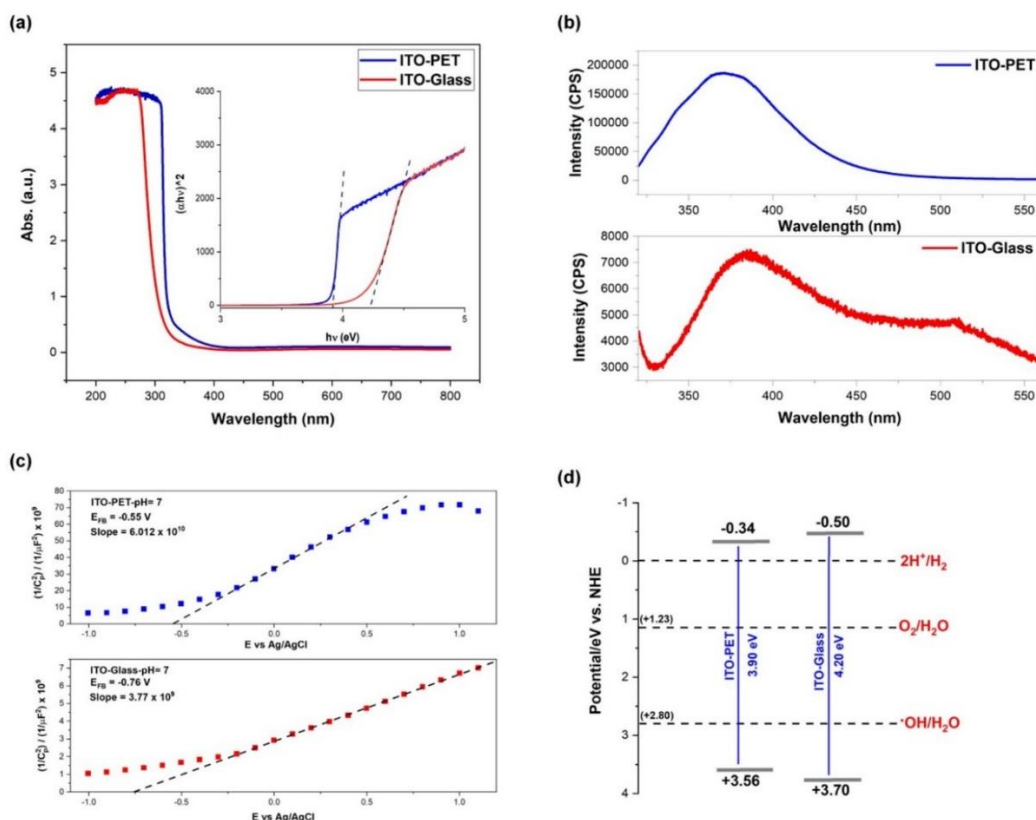


Figure 34. a) UV-Vis spectra with embedded Tauc's plot, b) PL spectra at the excitation wavelength of 300 nm, c) Mott-Schottky plots, and d) Schematic of the band structure for ITO-PET and ITO-Glass.

4.3.1.2 XRD

Figure 35 presents the X-ray diffraction patterns of the ITO-PET and ITO-Glass films. Since PET has a prominent peak in the area where the peaks of the ITO are situated, it was unable to determine the structure of the ITO on PET from the XRD pattern[149,150]. A cubic In_2O_3 structure may be seen in the XRD pattern of ITO on glass (PDF no. 06-0416)[151,152]. However, the XRD patterns of the ITO films did not reveal any SnO_2 -related XRD peaks.

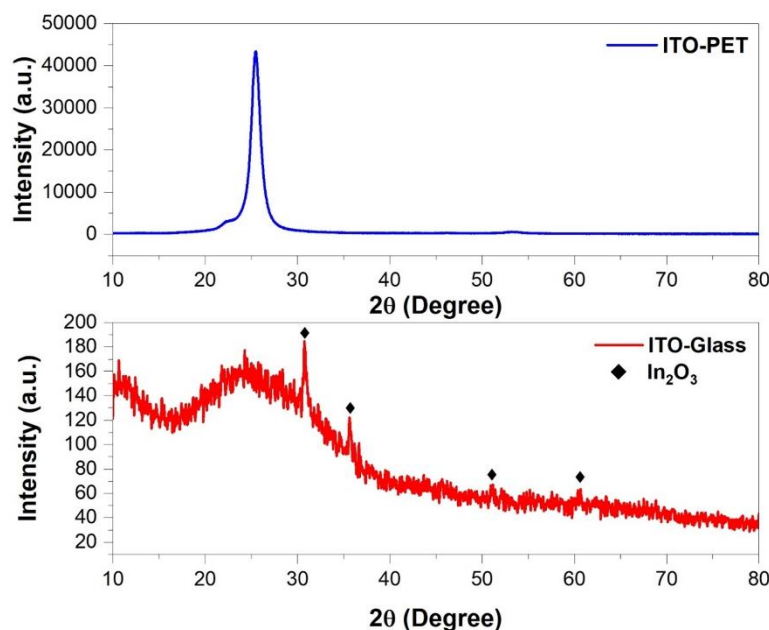


Figure 35. XRD patterns of ITO-PET and ITO-Glass films.

4.3.1.3 XPS analysis of ITO-Glass and ITO-PET films

XPS was used to investigate the oxidation state and chemical composition of the catalysts, and the results are shown in *Figure 36*. The ITO-PET In 3d spectra displays two distinct peaks at 444.49 and 452.02 eV (*Figure 36* (a)). These peaks correspond with In 3d_{3/2} and In 3d_{5/2}, respectively. These binding energies are within the normal range reported in the scientific literature for In³⁺ [66,153–156]. In addition, the binding energies at 486.86 eV and 495.30 eV in *Figure 36* (b) correlate to Sn 3d_{5/2} and Sn 3d_{3/2}, respectively, which indicate the oxidation state of Sn⁴⁺[156]. The O 1s spectrum (*Figure 36* (c)) was deconvoluted into four peaks, which were attributed to lattice oxygen (O_L), oxygen near the oxygen vacancy (O_v), surface oxygen (O_s), and adsorbed oxygen species (O_{ads}), respectively[65,157,158]. Similar deconvolution was used for the ITO-Glass In, Sn, and O spectra, and the resulting graphs are given in *Figure 36* (d)-(f). The In 3d spectrum (*Figure 36* (d)) exhibits two prominent peaks with binding energies of 444.00 and 451.60 eV, whereas the Sn 3d spectrum (*Figure 36* (e)) shows two peaks at binding energies of 486.04 and 494.43 eV. Furthermore, the four peaks from the deconvolution of the O 1s spectra are located at binding

energies of 530.27, 531.46, 532.34, and 533.88 eV. Also, the electron density of the components of the ITO-Glass catalyst was measured in situ using XPS (*Figure 36* (g)-(i)). When exposed to light (365 nm wavelength), small shifts towards positive binding energies in the In 3d and Sn 3d spectra (*Figure 36* (g) and (h)) suggest a reduction in electron density for these elements[159,160]. With light irradiation, there is a large rise in the intensity of the O 1s spectrum (*Figure 36* (i)) and a slight shift towards lower binding energies in the range of binding energies associated with the O_L and O_V , implying that electrons are transferred from In and Sn to oxygen.

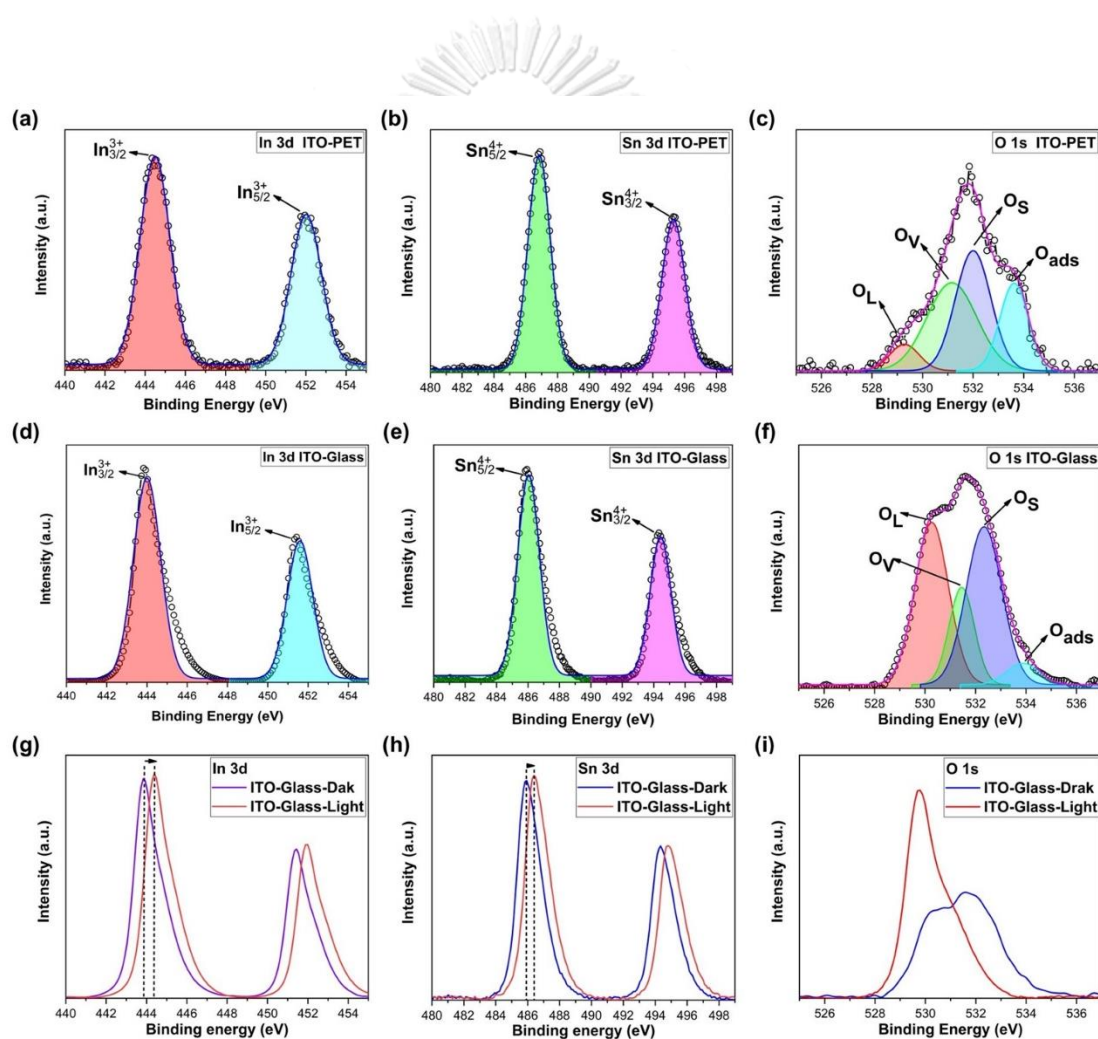


Figure 36. XPS spectra of a) In 3d, b)Sn 3d, and c) O 1s for ITO-PET, XPS spectra of d) In 3d, e)Sn 3d, and f) O 1s for ITO-Glass, and (g)-(i) high-resolution XPS for In 3d, Sn 3d, and O 1s of ITO-Glass under 365 nm light irradiation.

4.3.2 Photocatalytic CO₂ reduction on ITO-PET and ITO-Glass thin films

4.3.2.1 Batch reactor

Figure 37 (a) and (b) show, the yields of generated CH₄ and CO, respectively, from the photocatalytic reduction of CO₂. In the batch reactor, the rates of CH₄ and CO formation were 190±5% and 900±10% (μmol.g_{cat}⁻¹.hr⁻¹), respectively, whereas the rates of CH₄ and CO generation over the ITO-Glass were only slightly higher than those over the ITO-PET, coming in at 260±5% and 950±10% (μmol.g_{cat}⁻¹.hr⁻¹) respectively. Additionally, Figure 37 (c) shows the stability of both catalysts through five cycles (each cycle lasted for 4 hr). After each cycle, the catalyst was only withdrawn from the reactor without being washed. In addition, the reactor was thoroughly cleaned using a piranha solution. In the stability tests, just the production of CH₄ was recorded. CH₄ production was reduced by 43% and 52% from the first cycle to the fifth cycle for ITO-PET and ITO-glass, respectively. The system's specific binding density may be evaluated via MD simulation. The specific binding density of a system is the total of its intermolecular forces, such as Van der Waals and hydrogen bonds, and may be used to explain affinity trends[99]. To analyze the catalyst-medium interaction in this study, four different reaction environments (ENV) were created. The specifications of each ENV are shown in Table 2. The calculation of E_{binding} is explained in section 4.1.3.

Figure 38 displays the images of each ENV together with the quantitative value of E_{binding}. All of the ENVs have positive E_{binding}. More products will build up in the batch reactor's headspace over time, which might continually alter the reaction medium's characteristics. The affinity of the products for the catalyst's surface may make it difficult for reactants to reach the catalyst's active site, which would negatively impact the rate of reaction. Additionally, there is a significant buildup of CO due to the yield of CO synthesis being much higher than the yield of CH₄ production. Surface affinity might considerably increase in the presence of high amounts of CO close to the surface, as shown by E_{binding} of ENV-3, which would cause the catalyst to be deactivated. This may be viewed as a batch system

disadvantage. However, in a flow reactor, the reaction's products would be released continually from the reactor, and the medium's characteristics would practically remain constant. In order to compare the flow reactor with the batch system, we investigated the CO₂ reduction over both catalysts in a flow system.

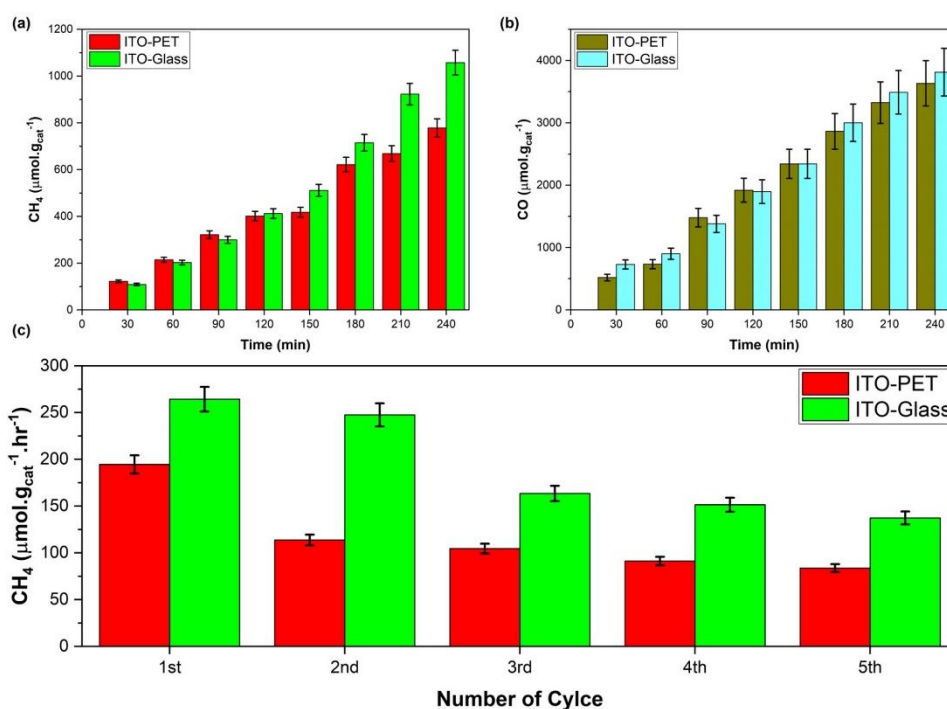


Figure 37. (a) and (b) CH₄ and CO yields from photocatalytic CO₂ reduction on ITO-PET and ITO-Glass, respectively. (c) ITO-PET and ITO-Glass stability during photocatalytic CO₂ reduction.

Table 2. The quantity and variety of molecules present in each environment for surface affinity trend simulations.

Environment	Number of target molecules			
	H ₂ O	CO ₂	CO	CH ₄
ENV-1	200	-	-	-
ENV-2	100	100	-	-
ENV-3	100	50	50	-
ENV-4	100	40	30	30

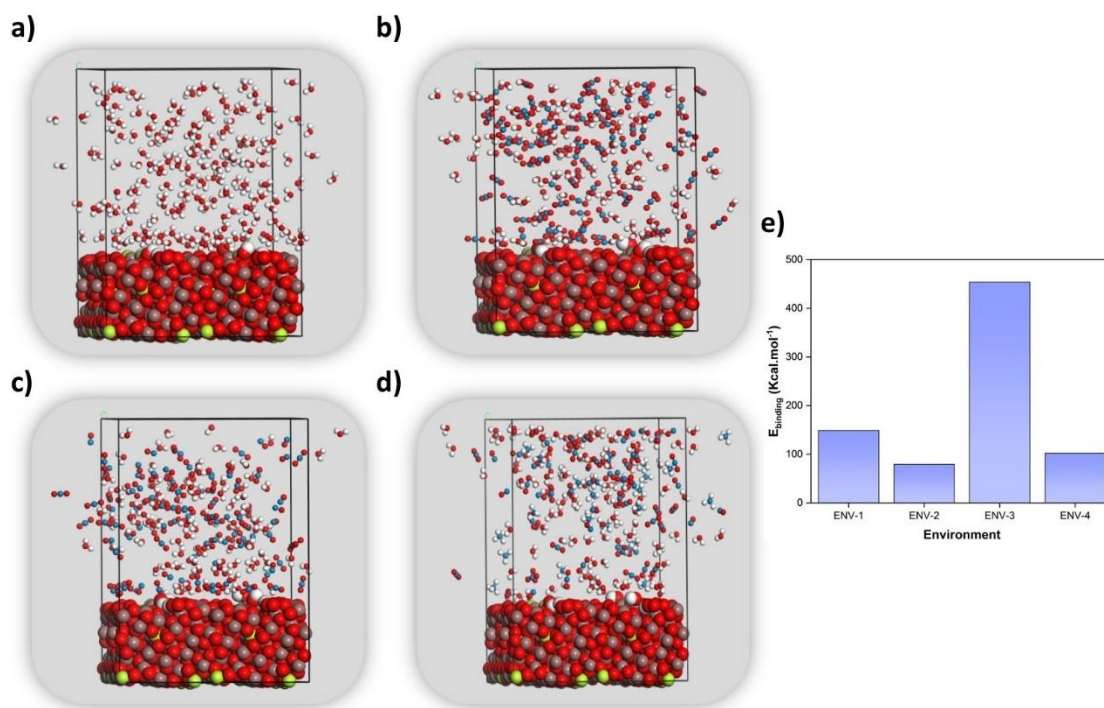


Figure 38. Images of simulation boxes used to compute $E_{binding}$ for the environments (a) ENV-1, (b) ENV-2, (c) ENV-3, (d) ENV-4, and (e) the environments' estimated $E_{binding}$.

4.3.2.2 Flow reactor

Figure 39 illustrates the results of the photocatalytic CO_2 reduction in the flow reactor. To minimize the effect of external mass transfer on the CO_2 reduction rate in the flow process, the CO_2 gas flow was raised from 6 to $10 \text{ ml}\cdot\text{min}^{-1}$ while the ratio of $(\text{CO}_2 \text{ flow rate})/(\text{area of the film})$ was maintained at $0.162 \text{ ml}\cdot\text{min}^{-1}\cdot\text{cm}^{-2}$. The results are depicted in Figure 40. As shown in Figure 40, increasing the CO_2 flow rate enhances the CH_4 generation yield on the ITO-Glass catalyst. However, the rate of CH_4 generation at 9 and $10 \text{ ml}\cdot\text{min}^{-1}$ is essentially the same (considering the error of measurement). Therefore, the experiments were conducted at a flow rate of $10 \text{ ml}\cdot\text{min}^{-1}$. Similar research was undertaken on the ITO-PET catalyst with similar results; hence, flow process studies were conducted for both catalysts under identical conditions. The formation rates of CH_4 and CO in the flow reactor were several times

greater than the batch reactor production rates. After 78 hours, the rates of CH_4 evolution for ITO-PET and ITO-Glass were $435 \pm 5\%$ and $600 \pm 5\%$ ($\mu\text{mol.g}_{\text{cat}}^{-1}.\text{hr}^{-1}$). Also, the production rates of CO rose to $2500 \pm 10\%$ and $2760 \pm 10\%$ ($\mu\text{mol.g}_{\text{cat}}^{-1}.\text{hr}^{-1}$) for ITO-PET and ITO-Glass in the flow reactor, respectively, as compared to the batch reactor. In addition to the observed increase in the production rates of reduction products, the catalysts in the flow reactor were more stable than in the batch reactor.

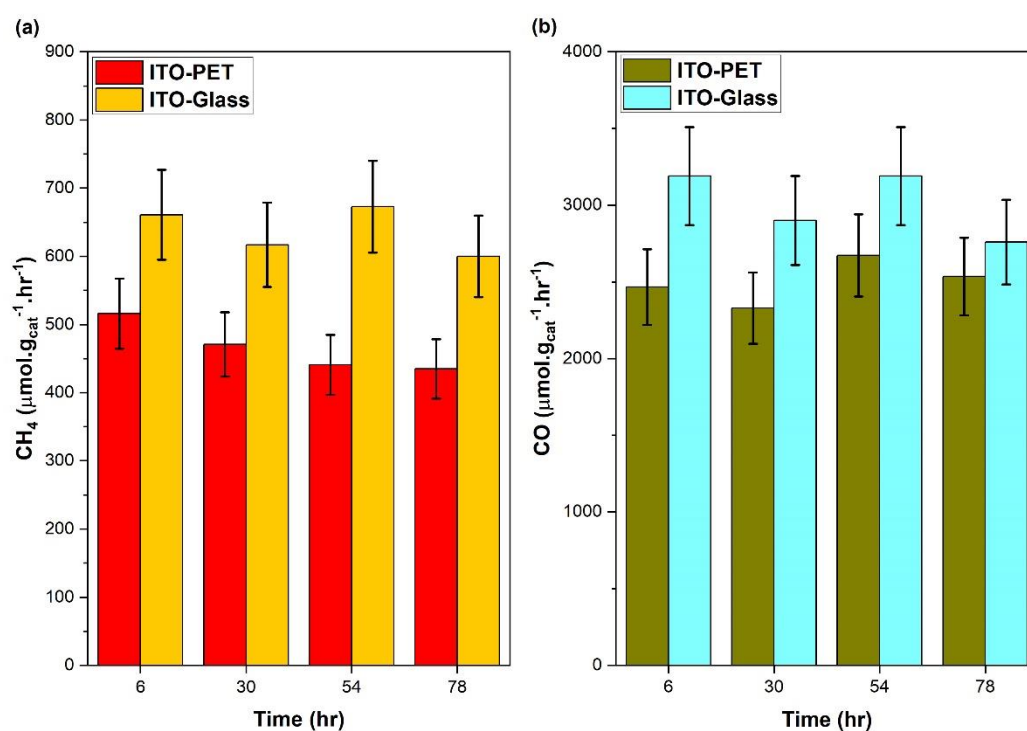


Figure 39. Yields of (a) CH_4 and (b) CO production from photocatalytic CO_2 reduction in the flow system.

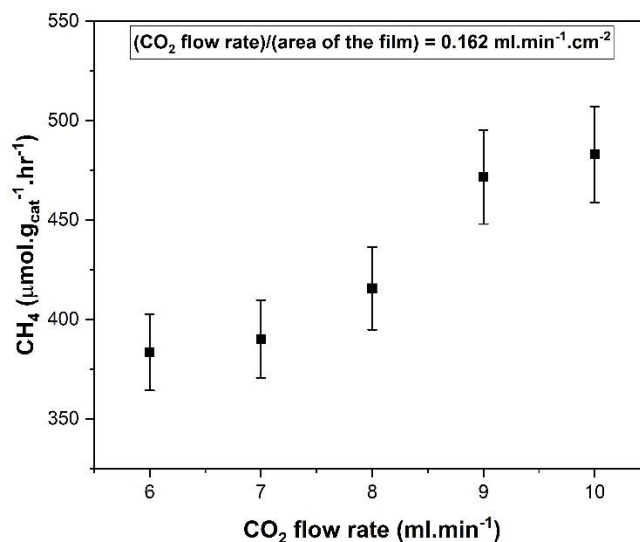


Figure 40. Study of external mass transfer effect on the rate of CO₂ conversion to CH₄ over ITO-Glass catalyst.

4.3.3 Simulation of CO₂ reduction mechanism on In₂O₃ and ITO

Each photocatalytic CO₂ reduction system has a distinct reduction reaction pathway that depends on the catalyst's properties, hence each system has to be studied independently. In light of this, we investigated a probable chemical route for CO₂ reduction on an ITO catalyst using DFT modeling. The findings were compared to simulation results computed for In₂O₃. Figure 41 (a) and (b) show the Gibbs free energy (ΔG) profiles of the CO₂ reduction processes on the oxygen vacancy (O_V) and lattice oxygen (O_L) of the In₂O₃ photocatalyst, respectively. Starting with the configuration of O-*C=O (Figure 41 (a) In-S1, $\Delta G = 0.206$ eV), the first hydrogenation process on O_L of In₂O₃ raises the ΔG value to 0.214 eV for conversion to O-*C-OH (Figure 41 (a) In-S2). Figure 41 (a), In-S3, O-*C-OH + e⁻ + H⁺ → CO + H₂O, the ΔG drops to -0.335 eV during the second hydrogenation step, enabling the exothermic generation of CO. The oxygen atom that is positioned between the two indium atoms is subsequently removed, leaving an oxygen vacancy in In₂O₃ (Figure 41 (b) In-O_V-S0). The CO₂ molecule is then present at the O_V site to create the intermediate O=C-O* (Figure 41 (b) In-O_V-*CO₂). Figure 41 (b) In-O_V-S1, O=C-O* + 2 e⁻ → CO, $\Delta G=0.160$ eV shows the endothermic process by which CO is

desorbed upon energy optimization. CO production at the O_V site is faster and requires less energy to overcome. Therefore, the decrease in the Gibbs energy suggests that CO production over O_V is more advantageous than O_L .

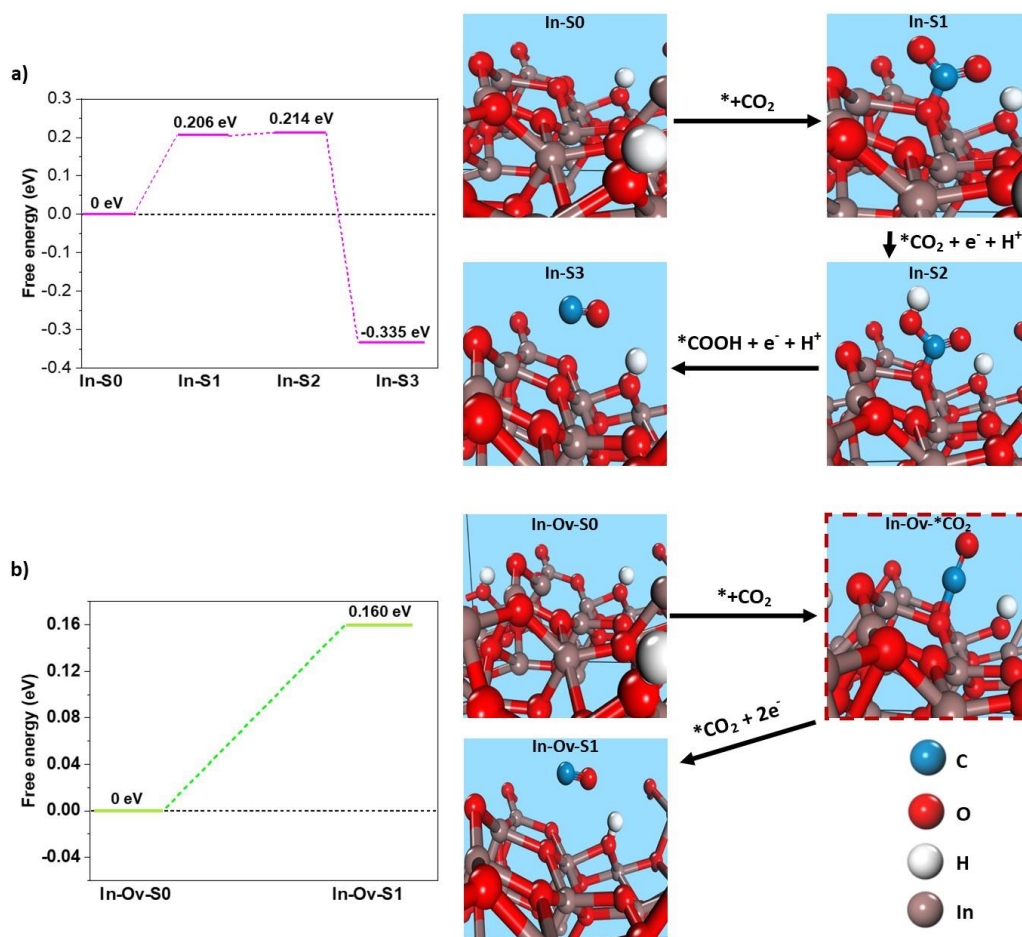


Figure 41. The ΔG profiles for CO_2 reduction on (a) lattice oxygen (O_L) of In_2O_3 , (b) oxygen vacancy (O_V) of In_2O_3 .

Additionally, the CO_2 reduction process on the ITO catalyst's O_V site remote from the Sn atom was studied; the Gibbs free energy profile is shown in Figure 42. By removing an oxygen atom from the space between two indium atoms, an O_V site is first created. In order to form $*O-C=O$ species, the CO_2 molecule is subsequently placed at the O_V site (Figure 42, ITO- O_V - $*CO_2$). Following energy optimization, the CO molecule is desorbed in an endothermic process, leaving the O_V site filled with

oxygen (Figure 42, ITO-O_V-1, O=C-O* + 2 e⁻ → CO, ΔG=0.032 eV). A comparison between the change in the Gibbs free energy for CO production from the O_V site of In₂O₃ (Figure 42 (b)) and the O_V site further from the Sn atom in ITO reveals that the CO₂ reduction into CO is more favorable on the ITO catalyst.

The O_V adjacent to the Sn atom in the ITO catalyst, as seen in Figure 43, is another reaction site. The obtained ΔG = -0.201 eV (Figure 43) by energy optimization implies that CO is formed in an exothermic process after CO₂ is placed on the O_V site. This study implies that the CO₂ molecule can be efficiently activated at the O_V site adjacent to the Sn atom, resulting in the production of CO.

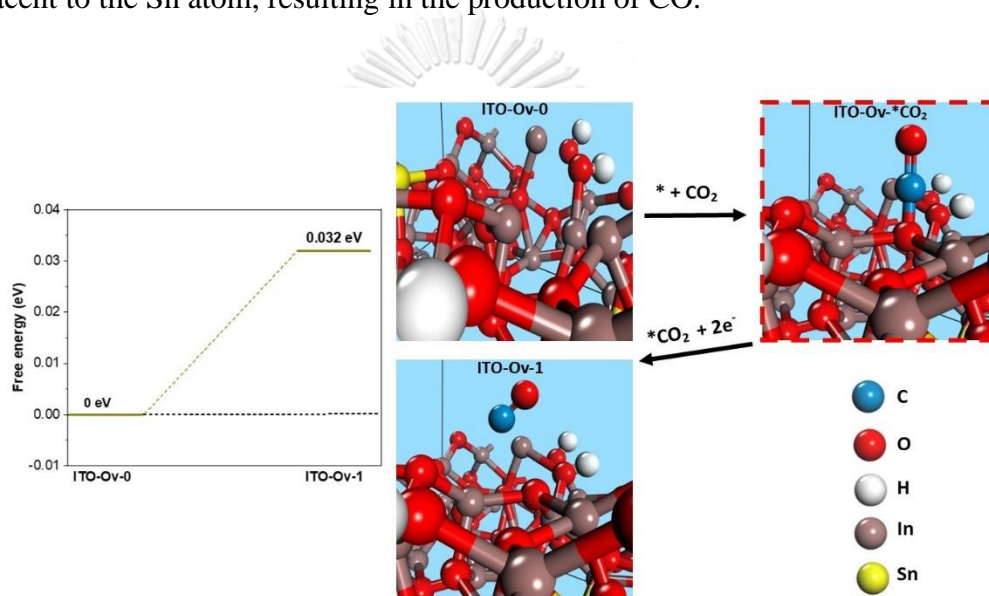


Figure 42. The ΔG profile of CO₂ reduction on O_V site between In atoms.

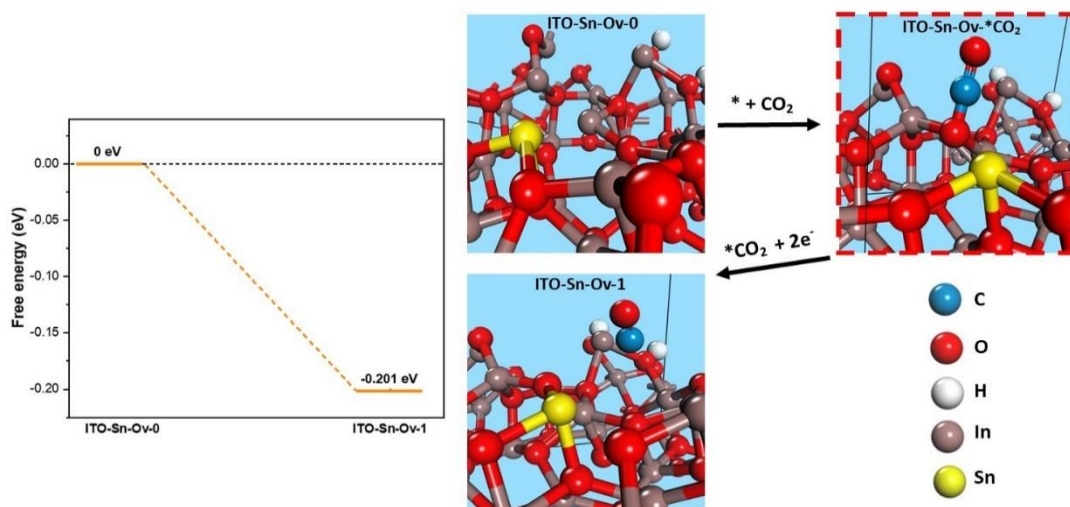


Figure 43. The ΔG profile of CO_2 reduction on O_V site between In atoms close to Sn atom.

The next reaction site examined was the OL next to the Sn atom (Figure 44). By transferring an e^- and an H^+ after establishing the $\text{O}^*-\text{C}=\text{O}$ configuration (Figure 44, ITO-Sn-1), it may be reduced to $\text{O}^*-\text{C}-\text{OH}$ (Figure 44, ITO-Sn-2, $\text{O}^*-\text{C}=\text{O} + e^- + \text{H}^+ \rightarrow \text{O}^*-\text{C}-\text{OH}$ $\Delta G=0.188$ eV). Two possible reaction pathways are shown for the reduction phase that follows. CO can be desorbed in the first pathway by the $\text{O}^*-\text{C}-\text{OH} + e^- + \text{H}^+ \rightarrow \text{CO} + \text{H}_2\text{O}$ reaction with $\Delta G = -0.290$ eV. (Figure 44, ITO-Sn-3I). In the second pathway, the transfer of $2e^-$ and 2H^+ might result in the formation of $\text{O}^*-\text{C}-\text{H}$ (Figure 44, ITO-Sn-3II, $\text{O}^*-\text{C}-\text{OH} + 2e^- + 2\text{H}^+ \rightarrow \text{O}^*-\text{C}-\text{H} + \text{H}_2\text{O}$ $\Delta G= -0.027$ eV). Comparing the ΔG values of ITO-Sn-3I and ITO-Sn-3II demonstrates that CO formation is more probable. The simulation on the second reaction pathway for the formation of CH_4 was continued. In the subsequent reduction stage, the transfer of an e^- and an H^+ led to the creation of $\text{HO}^*-\text{C}-\text{H}$ (Figure 44, ITO-Sn-4II, $\text{O}^*-\text{C}-\text{H} + e^- + \text{H}^+ \rightarrow \text{HO}^*-\text{C}-\text{H}$ $\Delta G=0.183$ eV). $\text{HO}^*-\text{C}-\text{H}$ may subsequently be converted to $^*\text{C}-\text{H}$ by an exothermic reaction with $\Delta G=-0.249$ eV (Figure 44, ITO-Sn-5II, $\text{HO}^*-\text{C}-\text{H} + e^- + \text{H}^+ \rightarrow ^*\text{C}-\text{H} + \text{H}_2\text{O}$). The sixth e^-/H^+ pair might attack the $^*\text{C}-\text{H}$ species, resulting in the synthesis of $^*\text{CH}_2$ species (Figure 44, ITO-Sn-6II, $^*\text{C}-\text{H} + e^- + \text{H}^+ \rightarrow ^*\text{C}-\text{H}_2$ $\Delta G=0.390$ eV). The reduction proceeded by transferring an additional e^-/H^+ pair to the $^*\text{CH}_2$ species (Figure 44, ITO-Sn-7II, $^*\text{CH}_2 + e^- + \text{H}^+ \rightarrow ^*\text{CH}_3$ $\Delta G=0.331$). Therefore, one CH_4 molecule might desorb from the surface of the catalyst by the

transfer of the eighth pair of e^-/H^+ . The simulation results demonstrate that while CH_4 synthesis over ITO is possible, it is less advantageous than CO formation. This might explain the ITO catalyst's impressive CO selectivity.



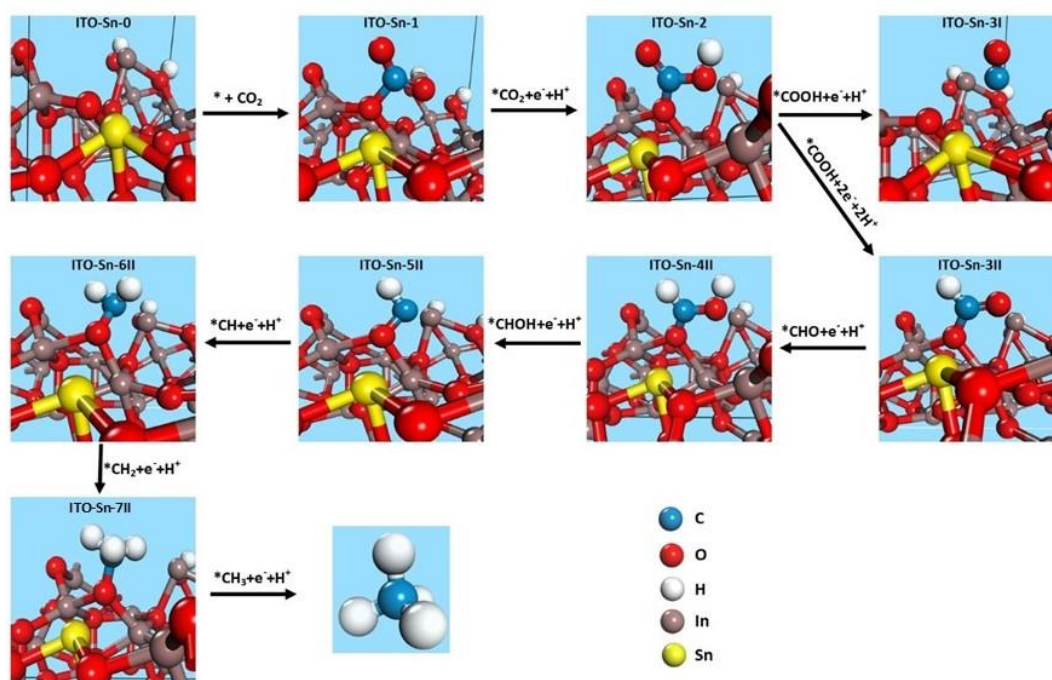
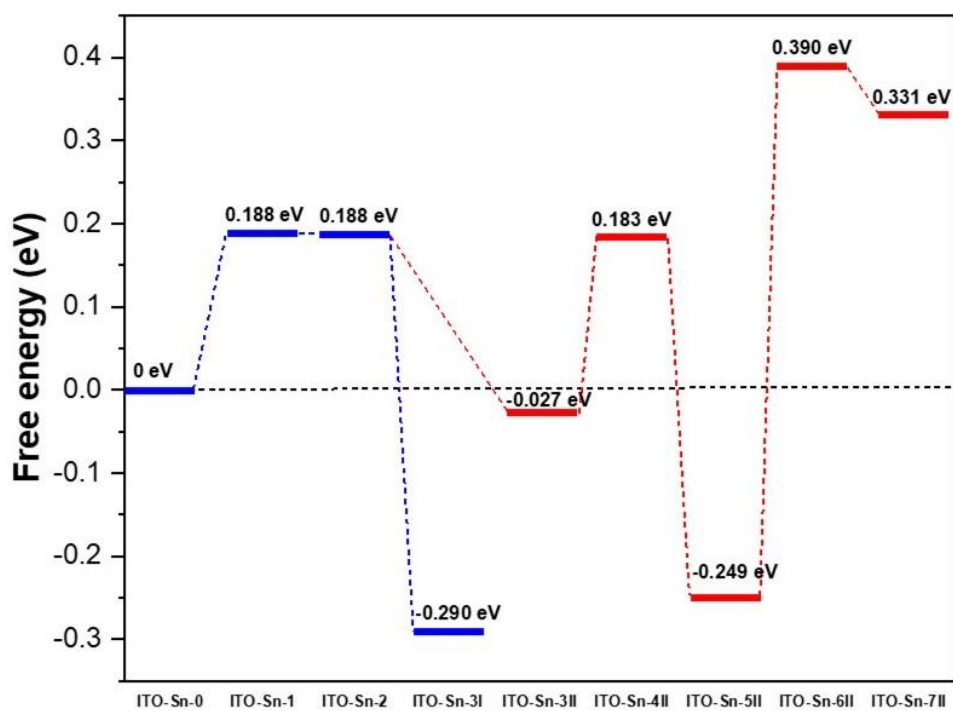


Figure 44. The ΔG profile for CO_2 reduction into CO and CH_4 on the O_L site close to Sn atom.

CHAPTER V:

CONCLUSIONS AND RECOMMENDATIONS

5.1 Conclusions

Although the substrate's conductivity has a substantial effect on the activity of the photocatalyst in the multielectron transfer reduction reaction, the substrate has no effect on the stability of the catalyst. Deactivation would result from the loss of oxygen vacancy or the strong attachment of products or by-products to the surface of the catalyst.

In the batch reactor, grand formation rates of $2650 \pm 5\%$, $530 \pm 5\%$, and $300 \pm 5\%$ ($\mu\text{mol.g}_{\text{cat}}^{-1}.\text{hr}^{-1}$) for CO, CH₄, and H₂ were obtained for the AM-TiO₂-SiO₂/ITO-PET photocatalyst, which are comparable to those reported for noble metal doped TiO₂ photocatalysts. Moreover, the production yield of $2760 \pm 10\%$ $\mu\text{mol.g}_{\text{cat}}^{-1}.\text{hr}^{-1}$ for ITO-Glass catalyst in the flow reactor setup indicates that this catalyst is highly active for CO₂ reduction into CO.

5.2 Recommendations

- The charge carrier transfer between the substrate and overlaid catalyst in thin films is dependent on the Schottky or Ohmic barrier formed between the two. It is proposed to investigate the influence of Schottky and Ohmic barriers on the catalyst's activity for the CO₂ reduction reaction.
- Depending on the thickness of the ITO thin film catalyst, the surface plasmons' wavelength can range from near ultraviolet to 800 nm. For photocatalytic CO₂ reduction in visible light, it is recommended to prepare ITO films of various thicknesses.
- The effect of the substrate in thin films on the adsorption characteristics of the overlying catalyst is significant but less studied. We recommend investigating

the effect of different substrates on the adsorption properties of the catalyst for CO₂ reduction.

- In disordered catalysts, the number of possible reaction pathways is indefinite, making simulations more time-consuming and less accurate. We recommend investigating the reaction mechanism using operando techniques, such as operando FTIR, to guide the simulation of the reaction mechanism.



REFERENCES



จุฬาลงกรณ์มหาวิทยาลัย
CHULALONGKORN UNIVERSITY

- [1] T. Pieter, R. Keeling, Earth System Research Laboratories. Trends in atmospheric carbon dioxide., Recent Mauna Loa CO₂. (2022). www.esrl.noaa.gov/gmd/ccgg/trends/.
- [2] D.M. D'Alessandro, B. Smit, J.R. Long, Carbon dioxide capture: Prospects for new materials, *Angew. Chemie - Int. Ed.* 49 (2010) 6058–6082. <https://doi.org/10.1002/anie.201000431>.
- [3] M. Aresta, A. Dibenedetto, A. Angelini, Catalysis for the valorization of exhaust carbon: From CO₂ to chemicals, materials, and fuels. technological use of CO₂, *Chem. Rev.* 114 (2014) 1709–1742. <https://doi.org/10.1021/cr4002758>.
- [4] A. Goepfert, M. Czaun, J.P. Jones, G.K. Surya Prakash, G.A. Olah, Recycling of carbon dioxide to methanol and derived products-closing the loop, *Chem. Soc. Rev.* 43 (2014) 7995–8048. <https://doi.org/10.1039/c4cs00122b>.
- [5] G. Centi, S. Perathoner, Opportunities and prospects in the chemical recycling of carbon dioxide to fuels, *Catal. Today.* 148 (2009) 191–205. <https://doi.org/10.1016/j.cattod.2009.07.075>.
- [6] J. Artz, T.E. Müller, K. Thenert, J. Kleinekorte, R. Meys, A. Sternberg, A. Bardow, W. Leitner, Sustainable Conversion of Carbon Dioxide: An Integrated Review of Catalysis and Life Cycle Assessment, *Chem. Rev.* 118 (2018) 434–504. <https://doi.org/10.1021/acs.chemrev.7b00435>.
- [7] G. Centi, E.A. Quadrelli, S. Perathoner, Catalysis for CO₂ conversion: A key technology for rapid introduction of renewable energy in the value chain of chemical industries, *Energy Environ. Sci.* 6 (2013) 1711–1731. <https://doi.org/10.1039/c3ee00056g>.
- [8] J. Low, B. Cheng, J. Yu, Surface modification and enhanced photocatalytic CO₂ reduction performance of TiO₂ : a review, *Appl. Surf. Sci.* 392 (2017) 658–686. <https://doi.org/10.1016/j.apsusc.2016.09.093>.
- [9] Y. Tachibana, L. Vayssieres, J.R. Durrant, Artificial photosynthesis for solar water-splitting, *Nat. Photonics.* 6 (2012) 511–518. <https://doi.org/10.1038/nphoton.2012.175>.
- [10] T. Zhang, W. Lin, Metal-organic frameworks for artificial photosynthesis and photocatalysis, *Chem. Soc. Rev.* 43 (2014) 5982–5993. <https://doi.org/10.1039/c4cs00103f>.
- [11] O. Ola, M.M. Maroto-Valer, Review of material design and reactor engineering on TiO₂ photocatalysis for CO₂ reduction, *J. Photochem. Photobiol. C Photochem. Rev.* 24 (2015) 16–42.

<https://doi.org/10.1016/j.jphotochemrev.2015.06.001>.

- [12] J.W. Wang, D.C. Zhong, T.B. Lu, Artificial photosynthesis: Catalytic water oxidation and CO₂ reduction by dinuclear non-noble-metal molecular catalysts, *Coord. Chem. Rev.* 377 (2018) 225–236. <https://doi.org/10.1016/j.ccr.2018.09.003>.
- [13] Y. Xia, K. Xiao, B. Cheng, J. Yu, L. Jiang, M. Antonietti, S. Cao, Improving Artificial Photosynthesis over Carbon Nitride by Gas–Liquid–Solid Interface Management for Full Light-Induced CO₂ Reduction to C₁ and C₂ Fuels and O₂, *ChemSusChem*. 13 (2020) 1730–1734. <https://doi.org/10.1002/cssc.201903515>.
- [14] J. Wu, Y. Huang, W. Ye, Y. Li, CO₂ Reduction: From the Electrochemical to Photochemical Approach, *Adv. Sci.* 4 (2017) 1–29. <https://doi.org/10.1002/advs.201700194>.
- [15] M. Cheng, S. Yang, R. Chen, X. Zhu, Q. Liao, Y. Huang, Copper-decorated TiO₂ nanorod thin films in optofluidic planar reactors for efficient photocatalytic reduction of CO₂, *Int. J. Hydrogen Energy*. 42 (2017) 9722–9732. <https://doi.org/10.1016/j.ijhydene.2017.01.126>.
- [16] E. Karamian, S. Sharifnia, On the general mechanism of photocatalytic reduction of CO₂, *J. CO₂ Util.* 16 (2016) 194–203. <https://doi.org/10.1016/j.jcou.2016.07.004>.
- [17] C.Y. Toe, Z. Zheng, H. Wu, J. Scott, R. Amal, Y.H. Ng, Photocorrosion of Cuprous Oxide in Hydrogen Production: Rationalising Self-Oxidation or Self-Reduction, *Angew. Chemie - Int. Ed.* 57 (2018) 13613–13617. <https://doi.org/10.1002/anie.201807647>.
- [18] C.Y. Toe, J. Scott, R. Amal, Y.H. Ng, Recent advances in suppressing the photocorrosion of cuprous oxide for photocatalytic and photoelectrochemical energy conversion, *J. Photochem. Photobiol. C Photochem. Rev.* 40 (2019) 191–211. <https://doi.org/10.1016/j.jphotochemrev.2018.10.001>.
- [19] X. Chang, T. Wang, J. Gong, CO₂ photo-reduction: Insights into CO₂ activation and reaction on surfaces of photocatalysts, *Energy Environ. Sci.* 9 (2016) 2177–2196. <https://doi.org/10.1039/c6ee00383d>.
- [20] S.N. Habisreutinger, L. Schmidt-Mende, J.K. Stolarczyk, Photocatalytic reduction of CO₂ on TiO₂ and other semiconductors, *Angew. Chemie - Int. Ed.* 52 (2013) 7372–7408. <https://doi.org/10.1002/anie.201207199>.
- [21] A. Vasileff, C. Xu, Y. Jiao, Y. Zheng, S.Z. Qiao, Surface and Interface

- Engineering in Copper-Based Bimetallic Materials for Selective CO₂ Electroreduction, *Chem.* 4 (2018) 1809–1831.
<https://doi.org/10.1016/j.chempr.2018.05.001>.
- [22] J. Fu, K. Jiang, X. Qiu, J. Yu, M. Liu, Product selectivity of photocatalytic CO₂ reduction reactions, *Mater. Today.* 32 (2020) 222–243.
<https://doi.org/10.1016/j.mattod.2019.06.009>.
- [23] L. Lopez, W.A. Daoud, D. Dutta, B.C. Panther, T.W. Turney, Effect of substrate on surface morphology and photocatalysis of large-scale TiO₂ films, *Appl. Surf. Sci.* 265 (2013) 162–168.
<https://doi.org/10.1016/j.apsusc.2012.10.156>.
- [24] C.S. Ryu, M.S. Kim, B.W. Kim, Photodegradation of alachlor with the TiO₂ film immobilised on the glass tube in aqueous solution, *Chemosphere.* 53 (2003) 765–771. [https://doi.org/10.1016/S0045-6535\(03\)00506-X](https://doi.org/10.1016/S0045-6535(03)00506-X).
- [25] M. Bideau, B. Claudel, C. Dubien, L. Faure, H. Kazouan, On the “immobilization” of titanium dioxide in the photocatalytic oxidation of spent waters, *J. Photochem. Photobiol. A Chem.* 91 (1995) 137–144.
[https://doi.org/10.1016/1010-6030\(95\)04098-Z](https://doi.org/10.1016/1010-6030(95)04098-Z).
- [26] H.D. Mansilla, C. Bravo, R. Ferreyra, M.I. Litter, W.F. Jardim, C. Lizama, J. Freer, J. Fernández, Photocatalytic EDTA degradation on suspended and immobilized TiO₂, *J. Photochem. Photobiol. A Chem.* 181 (2006) 188–194.
<https://doi.org/10.1016/j.jphotochem.2005.11.023>.
- [27] N. Serpone, E. Borgarello, R. Harris, P. Cahill, M. Borgarello, E. Pelizzetti, Photocatalysis over TiO₂ supported on a glass substrate, *Sol. Energy Mater.* 14 (1986) 121–127. [https://doi.org/10.1016/0165-1633\(86\)90070-5](https://doi.org/10.1016/0165-1633(86)90070-5).
- [28] B. Gao, P.S. Yap, T.M. Lim, T.T. Lim, Adsorption-photocatalytic degradation of Acid Red 88 by supported TiO₂: Effect of activated carbon support and aqueous anions, *Chem. Eng. J.* 171 (2011) 1098–1107.
<https://doi.org/10.1016/j.cej.2011.05.006>.
- [29] G. Xue, H. Liu, Q. Chen, C. Hills, M. Tyrer, F. Innocent, Synergy between surface adsorption and photocatalysis during degradation of humic acid on TiO₂/activated carbon composites, *J. Hazard. Mater.* 186 (2011) 765–772.
<https://doi.org/10.1016/j.jhazmat.2010.11.063>.
- [30] K. Tennakone, C.T.K. Tilakaratne, I.R.M. Kottegoda, Photocatalytic degradation of organic contaminants in water with TiO₂ supported on polythene films, *J. Photochem. Photobiol. A Chem.* 87 (1995) 177–179.
[https://doi.org/10.1016/1010-6030\(94\)03980-9](https://doi.org/10.1016/1010-6030(94)03980-9).

- [31] R.A. Damodar, T. Swaminathan, Performance evaluation of a continuous flow immobilized rotating tube photocatalytic reactor (IRTPR) immobilized with TiO₂ catalyst for azo dye degradation, *Chem. Eng. J.* 144 (2008) 59–66. <https://doi.org/10.1016/j.cej.2008.01.014>.
- [32] M.E. Fabiyi, R.L. Skelton, Photocatalytic mineralisation of methylene blue using buoyant TiO₂-coated polystyrene beads, *J. Photochem. Photobiol. A Chem.* 132 (2000) 121–128. [https://doi.org/10.1016/S1010-6030\(99\)00250-6](https://doi.org/10.1016/S1010-6030(99)00250-6).
- [33] D. Li, H. Zheng, Q. Wang, X. Wang, W. Jiang, Z. Zhang, Y. Yang, A novel double-cylindrical-shell photoreactor immobilized with monolayer TiO₂-coated silica gel beads for photocatalytic degradation of Rhodamine B and Methyl Orange in aqueous solution, *Sep. Purif. Technol.* 123 (2014) 130–138. <https://doi.org/10.1016/j.seppur.2013.12.029>.
- [34] N. Negishi, T. Sano, T. Hirakawa, F. Koiwa, C. Chawengkijwanich, N. Pimpha, G.R.M. Echavia, Photocatalytic detoxification of aqueous organophosphorus by TiO₂ immobilized silica gel, *Appl. Catal. B Environ.* 128 (2012) 105–118. <https://doi.org/10.1016/j.apcatb.2012.04.039>.
- [35] N.F. Zainudin, A.Z. Abdullah, A.R. Mohamed, Characteristics of supported nano-TiO₂/ZSM-5/silica gel (SNTZS): Photocatalytic degradation of phenol, *J. Hazard. Mater.* 174 (2010) 299–306. <https://doi.org/10.1016/j.jhazmat.2009.09.051>.
- [36] G. Plantard, V. Goetz, D. Sacco, TiO₂-coated foams as a medium for solar catalysis, *Mater. Res. Bull.* 46 (2011) 231–234. <https://doi.org/10.1016/j.materresbull.2010.11.011>.
- [37] G. Plesch, M. Gorbár, U.F. Vogt, K. Jesenák, M. Vargová, Reticulated macroporous ceramic foam supported TiO₂ for photocatalytic applications, *Mater. Lett.* 63 (2009) 461–463. <https://doi.org/10.1016/j.matlet.2008.11.008>.
- [38] D.E. Santiago, M.R. Espino-Estévez, G. V. González, J. Araña, O. González-Díaz, J.M. Doña-Rodríguez, Photocatalytic treatment of water containing imazalil using an immobilized TiO₂ photoreactor, *Appl. Catal. A Gen.* 498 (2015) 1–9. <https://doi.org/10.1016/j.apcata.2015.03.021>.
- [39] I. Levchuk, C. Guillard, F. Dappozze, S. Parola, D. Leonard, M. Sillanpää, Photocatalytic activity of TiO₂ films immobilized on aluminum foam by atomic layer deposition technique, *J. Photochem. Photobiol. A Chem.* 328 (2016) 16–23. <https://doi.org/10.1016/j.jphotochem.2016.03.034>.
- [40] H. Guo, M. Kemell, M. Heikkilä, M. Leskelä, Noble metal-modified TiO₂ thin film photocatalyst on porous steel fiber support, *Appl. Catal. B Environ.* 95

- (2010) 358–364. <https://doi.org/10.1016/j.apcatb.2010.01.014>.
- [41] I. Levchuk, M. Kralova, J.J. Rueda-Márquez, J. Moreno-Andrés, S. Gutiérrez-Alfaro, P. Dzik, S. Parola, M. Sillanpää, R. Vahala, M.A. Manzano, Antimicrobial activity of printed composite TiO₂/SiO₂ and TiO₂/SiO₂/Au thin films under UVA-LED and natural solar radiation, *Appl. Catal. B Environ.* 239 (2018) 609–618. <https://doi.org/10.1016/j.apcatb.2018.08.051>.
- [42] K. Nomura, H. Ohta, A. Takagi, T. Kamiya, M. Hirano, H. Hosono, Room-temperature fabrication of transparent flexible thin-film transistors using amorphous oxide semiconductors, *Nature*. 432 (2004) 488. <https://www.nature.com/articles/nature03090.pdf>.
- [43] K. Huo, B. Gao, J. Fu, L. Zhao, P.K. Chu, Fabrication, modification, and biomedical applications of anodized TiO₂ nanotube arrays, *RSC Adv.* 4 (2014) 17300–17324. <https://doi.org/10.1039/c4ra01458h>.
- [44] D. Zywitzki, H. Jing, H. Tüysüz, C.K. Chan, High surface area, amorphous titania with reactive Ti³⁺ through a photo-assisted synthesis method for photocatalytic H₂ generation, *J. Mater. Chem. A*. 5 (2017) 10957–10967. <https://doi.org/10.1039/c7ta01614j>.
- [45] J.S. Santos, M. Fereidooni, V. Marquez, M. Arumugam, M. Tahir, S. Praserthdam, P. Praserthdam, Single-step fabrication of highly stable amorphous TiO₂ nanotubes arrays (am-TNTA) for stimulating gas-phase photoreduction of CO₂ to methane, *Chemosphere*. 289 (2022). <https://doi.org/10.1016/j.chemosphere.2021.133170>.
- [46] M.M. Zhang, J.Y. Chen, H. Li, C.R. Wang, Recent progress in Li-ion batteries with TiO₂ nanotube anodes grown by electrochemical anodization, *Rare Met.* 40 (2021) 249–271. <https://doi.org/10.1007/s12598-020-01499-x>.
- [47] K. Wu, J. Chen, J.R. McBride, T. Lian, Efficient hot-electron transfer by a plasmon-induced interfacial charge-transfer transition, *Science* (80). 349 (2015) 632–635. <https://doi.org/10.1126/science.aac5443>.
- [48] Y. Zhang, S. He, W. Guo, Y. Hu, J. Huang, J.R. Mulcahy, W.D. Wei, Surface-Plasmon-Driven Hot Electron Photochemistry, *Chem. Rev.* 118 (2018) 2927–2954. <https://doi.org/10.1021/acs.chemrev.7b00430>.
- [49] W. Hou, S.B. Cronin, A review of surface plasmon resonance-enhanced photocatalysis, *Adv. Funct. Mater.* 23 (2013) 1612–1619. <https://doi.org/10.1002/adfm.201202148>.
- [50] R. Zakaria, N.A. a. M. Zainuddin, T.C. Leong, R. Rosli, M.F. Rusdi, S.W.

- Harun, I.S. Amiri, Investigation of surface plasmon resonance (SPR) in MoS₂- and WS₂-protected titanium side-polished optical fiber as a humidity sensor, *Micromachines*. 10 (2019). <https://doi.org/10.3390/mi10070465>.
- [51] S.K. Mishra, B.D. Gupta, Surface Plasmon Resonance-Based Fiber-Optic Hydrogen Gas Sensor Utilizing Indium-Tin Oxide (ITO) Thin Films, *Plasmonics*. 7 (2012) 627–632. <https://doi.org/10.1007/s11468-012-9351-7>.
- [52] M. Tahir, N.S. Amin, Advances in visible light responsive titanium oxide-based photocatalysts for CO₂ conversion to hydrocarbon fuels, *Energy Convers. Manag.* 76 (2013) 194–214. <https://doi.org/10.1016/j.enconman.2013.07.046>.
- [53] H. Abdullah, M.M.R. Khan, H.R. Ong, Z. Yaakob, Modified TiO₂ photocatalyst for CO₂ photocatalytic reduction: An overview, *J. CO₂ Util.* 22 (2017) 15–32. <https://doi.org/10.1016/j.jcou.2017.08.004>.
- [54] A.K. Kharade, S.M. Chang, Contributions of Abundant Hydroxyl Groups to Extraordinarily High Photocatalytic Activity of Amorphous Titania for CO₂ Reduction, *J. Phys. Chem. C*. 124 (2020) 10981–10992. <https://doi.org/10.1021/acs.jpcc.0c01548>.
- [55] A. Wang, S. Wu, J. Dong, R. Wang, J. Wang, J. Zhang, S. Zhong, S. Bai, Interfacial facet engineering on the Schottky barrier between plasmonic Au and TiO₂ in boosting the photocatalytic CO₂ reduction under ultraviolet and visible light irradiation, *Chem. Eng. J.* 404 (2021) 127145. <https://doi.org/10.1016/j.cej.2020.127145>.
- [56] H. Park, Y. Park, W. Kim, W. Choi, Surface modification of TiO₂ photocatalyst for environmental applications, *J. Photochem. Photobiol. C Photochem. Rev.* 15 (2013) 1–20. <https://doi.org/10.1016/j.jphotochemrev.2012.10.001>.
- [57] C.M. Malengreaux, S.L. Pirard, G. Léonard, J.G. Mahy, M. Herlitschke, B. Klobes, R. Hermann, B. Heinrichs, J.R. Bartlett, Study of the photocatalytic activity of Fe³⁺, Cr³⁺, La³⁺ and Eu³⁺ single-doped and co-doped TiO₂ catalysts produced by aqueous sol-gel processing, *J. Alloys Compd.* 691 (2017) 726–738. <https://doi.org/10.1016/j.jallcom.2016.08.211>.
- [58] M. Szkoda, K. Siuzdak, A. Lisowska-Oleksiak, Non-metal doped TiO₂ nanotube arrays for high efficiency photocatalytic decomposition of organic species in water, *Phys. E Low-Dimensional Syst. Nanostructures*. 84 (2016) 141–145. <https://doi.org/10.1016/j.physe.2016.06.004>.
- [59] D.N. Liu, G.H. He, L. Zhu, W.Y. Zhou, Y.H. Xu, Enhancement of

- photocatalytic activity of TiO₂ nanoparticles by coupling Sb₂O₃, *Appl. Surf. Sci.* 258 (2012) 8055–8060. <https://doi.org/10.1016/j.apsusc.2012.04.171>.
- [60] A. Romero-Morán, J.L. Sánchez-Salas, J. Molina-Reyes, Influence of selected reactive oxygen species on the photocatalytic activity of TiO₂/SiO₂ composite coatings processed at low temperature, *Appl. Catal. B Environ.* 291 (2021). <https://doi.org/10.1016/j.apcatb.2020.119685>.
- [61] D.S.C. Halin, M.M.A.B. Abdullah, N. Mahmed, S.N.A. Abdul Malek, P. Vitureanu, A.W. Azhari, Synthesis and Characterization of TiO₂/SiO₂ Thin Film via Sol-Gel Method, *IOP Conf. Ser. Mater. Sci. Eng.* 209 (2017). <https://doi.org/10.1088/1757-899X/209/1/012002>.
- [62] X. Fu, L.A. Clark, Q. Yang, M.A. Anderson, Enhanced Photocatalytic Performance of Titania-Based Binary Metal Oxides: TiO₂/SiO₂ and TiO₂/ZrO₂, *Environ. Sci. Technol.* 30 (1996) 647–653. <https://doi.org/10.1021/es950391v>.
- [63] J. Ba, D.F. Rohlfiing, A. Feldhoff, T. Brezesinski, I. Djerdj, M. Wark, M. Niederberger, Nonaqueous synthesis of uniform indium tin oxide nanocrystals and their electrical conductivity in dependence of the tin oxide concentration, *Chem. Mater.* 18 (2006) 2848–2854. <https://doi.org/10.1021/cm060548q>.
- [64] A. Solieman, M.K. Zayed, S.N. Alamri, N. Al-Dahoudi, M.A. Aegerter, Corundum nanostructure ITO film fabrication: An approach for physical properties assessment, *Mater. Chem. Phys.* 134 (2012) 127–132. <https://doi.org/10.1016/j.matchemphys.2012.02.040>.
- [65] S. Banerjee, S. Mandal, A.K. Barua, N. Mukherjee, Hierarchical indium tin oxide (ITO) nano-whiskers: Electron beam deposition and sub-bandgap defect levels mediated visible light driven enhanced photocatalytic activity, *Catal. Commun.* 87 (2016) 86–89. <https://doi.org/10.1016/j.catcom.2016.09.001>.
- [66] C. Donley, D. Dunphy, D. Paine, C. Carter, K. Nebesny, P. Lee, D. Alloway, N.R. Armstrong, Characterization of indium-tin oxide interfaces using X-ray photoelectron spectroscopy and redox processes of a chemisorbed probe molecule: Effect of surface pretreatment conditions, *Langmuir.* 18 (2002) 450–457. <https://doi.org/10.1021/la0111101t>.
- [67] X. Wang, L. Lu, B. Wang, Z. Xu, Z. Xin, S. Yan, Z. Geng, Z. Zou, Frustrated Lewis Pairs Accelerating CO₂ Reduction on Oxyhydroxide Photocatalysts with Surface Lattice Hydroxyls as a Solid-State Proton Donor, *Adv. Funct. Mater.* 28 (2018) 1–9. <https://doi.org/10.1002/adfm.201804191>.
- [68] H. Yu, S. Yan, P. Zhou, Z. Zou, CO₂ photoreduction on hydroxyl-group-rich mesoporous single crystal TiO₂, *Appl. Surf. Sci.* 427 (2018) 603–607.

<https://doi.org/10.1016/j.apsusc.2017.08.073>.

- [69] S. Couck, J.F.M. Denayer, G. V. Baron, T. Rémy, J. Gascon, F. Kapteijn, An amine-functionalized MIL-53 metal-organic framework with large separation power for CO₂ and CH₄, *J. Am. Chem. Soc.* 131 (2009) 6326–6327. <https://doi.org/10.1021/ja900555r>.
- [70] S. Sun, P. Song, J. Cui, S. Liang, Amorphous TiO₂ nanostructures: Synthesis, fundamental properties and photocatalytic applications, *Catal. Sci. Technol.* 9 (2019) 4198–4215. <https://doi.org/10.1039/c9cy01020c>.
- [71] H. Moradi, H. Azizpour, H. Bahmanyar, M. Mohammadi, M. Akbari, Prediction of methane diffusion coefficient in water using molecular dynamics simulation, *Heliyon.* 6 (2020) e05385. <https://doi.org/10.1016/j.heliyon.2020.e05385>.
- [72] J.A. Yuwono, P. Burr, C. Galvin, A. Lennon, Atomistic Insights into Lithium Storage Mechanisms in Anatase, Rutile, and Amorphous TiO₂ Electrodes, *ACS Appl. Mater. Interfaces.* 13 (2021) 1791–1806. <https://doi.org/10.1021/acsami.0c17097>.
- [73] Y. Tian, C. Shi, Y. Sun, C. Zhu, C.C. Sun, S. Mao, Designing micellar Nanocarriers with improved drug loading and stability based on solubility parameter, *Mol. Pharm.* 12 (2015) 816–825. <https://doi.org/10.1021/mp5006504>.
- [74] J.L.S. García, M.I.L. Bastarrachea, M. De Jesús Aguilar Vega, Aromatic polyamides density from molecular dynamics simulation, *Macromol. Symp.* 325–326 (2013) 120–124. <https://doi.org/10.1002/masy.201200036>.
- [75] Y. Liang, L. Chen, C. Ma, Kinetics and thermodynamics of H₂O dissociation and CO oxidation on the Pt/WC (0001) surface: A density functional theory study, *Surf. Sci.* 656 (2017) 7–16. <https://doi.org/10.1016/j.susc.2016.08.009>.
- [76] K. Hirao, H.S. Bae, J.W. Song, B. Chan, Koopmans'-Type Theorem in Kohn-Sham Theory with Optimally Tuned Long-Range-Corrected (LC) Functionals, *J. Phys. Chem. A.* 125 (2021) 3489–3502. <https://doi.org/10.1021/acs.jpca.1c01593>.
- [77] X. Zeng, X. Xiao, W. Zhang, C. Wan, H. Wang, Interfacial charge transfer and mechanisms of enhanced photocatalysis of an anatase TiO₂(0 0 1)-MoS₂-graphene nanocomposite: A first-principles investigation, *Comput. Mater. Sci.* 126 (2017) 43–51. <https://doi.org/10.1016/j.commatsci.2016.09.014>.
- [78] B. Xiong, Y. Yang, J. Liu, J. Ding, Y. Yang, Crystal orientation effects on the

- electrochemical conversion of CO₂ to syngas over Cu-M (M = Ag, Ni, Zn, Cd, and Pd) bimetal catalysts, *Appl. Surf. Sci.* 567 (2021) 150839. <https://doi.org/10.1016/j.apsusc.2021.150839>.
- [79] X.Y. Yu, S.Y. Wu, G.Q. Shen, L. Yan, Z.T. Wei, X.Y. Li, Density functional theory calculations of copper-doped rutile crystals: Local structural, electronic, optical, and electron paramagnetic resonance properties, *Magn. Reson. Chem.* 60 (2022) 104–112. <https://doi.org/10.1002/mrc.5190>.
- [80] M.K. Guediri, D. Chebli, A. Bouguettoucha, R. Bourzami, A. Amrane, Interfacial coupling effects on adsorptive and photocatalytic performances for photoresponsive graphene-wrapped SrTiO₃@Ag under UV–visible light: experimental and DFT approach, *Environ. Sci. Pollut. Res.* 29 (2022) 28098–28114. <https://doi.org/10.1007/s11356-021-17543-x>.
- [81] M.H. Samat, M.F.M. Taib, O.H. Hassan, N.H. Hussin, D.T. Mustaffa, N.K. Jaafar, R. Zakaria, M.Z.A. Yahya, A.M.M. Ali, Influence of Nd concentrations on the structural, electronic and optical properties of anatase TiO₂: A first-principles approach, *Comput. Condens. Matter.* 31 (2022) e00672. <https://doi.org/10.1016/j.cocom.2022.e00672>.
- [82] H. Ning, G. Wei, L. Zhao, Z. Meng, Z. Wang, Z. Lan, H. Liu, J. Guo, J. Deng, Effects of transition metal Ti and its compounds on hydrogen adsorption performance of Mg₁₇Al₁₂, *Int. J. Hydrogen Energy.* 47 (2022) 13900–13910. <https://doi.org/10.1016/j.ijhydene.2022.02.140>.
- [83] A. Farzaneh, M. Javidani, M.D. Esrafil, O. Mermer, Optical and photocatalytic characteristics of Al and Cu doped TiO₂: Experimental assessments and DFT calculations, *J. Phys. Chem. Solids.* 161 (2022) 110404. <https://doi.org/10.1016/j.jpcs.2021.110404>.
- [84] M.A. Henderson, W.S. Epling, C.H.F. Peden, C.L. Perkins, Insights into photoexcited electron scavenging processes on TiO₂ obtained from studies of the reaction of O₂ with OH groups adsorbed at electronic defects on TiO₂(110), *J. Phys. Chem. B.* 107 (2003) 534–545. <https://doi.org/10.1021/jp0262113>.
- [85] J. Zou, J. Gao, F. Xie, An amorphous TiO₂ sol sensitized with H₂O₂ with the enhancement of photocatalytic activity, *J. Alloys Compd.* 497 (2010) 420–427. <https://doi.org/10.1016/j.jallcom.2010.03.093>.
- [86] T. xu Liu, F. bai Li, X. zhong Li, TiO₂ hydrosols with high activity for photocatalytic degradation of formaldehyde in a gaseous phase, *J. Hazard. Mater.* 152 (2008) 347–355. <https://doi.org/10.1016/j.jhazmat.2007.07.003>.
- [87] Z. Wang, F. Zhang, Y. Yang, B. Xue, J. Cui, N. Guan, Facile postsynthesis of

- visible-light-sensitive titanium dioxide/mesoporous SBA-15, *Chem. Mater.* 19 (2007) 3286–3293. <https://doi.org/10.1021/cm062041l>.
- [88] E. Obuchi, T. Sakamoto, K. Nakano, F. Shiraishi, Photocatalytic decomposition of acetaldehyde over TiO₂/SiO₂ catalyst, *Chem. Eng. Sci.* 54 (1999) 1525–1530. [https://doi.org/10.1016/S0009-2509\(99\)00067-6](https://doi.org/10.1016/S0009-2509(99)00067-6).
- [89] Ștefan Neatu, J.A. Maciá-Agulló, P. Concepció, H. Garcia, Gold-copper nanoalloys supported on TiO₂ as photocatalysts for CO₂ reduction by water, *J. Am. Chem. Soc.* 136 (2014) 15969–15976. <https://doi.org/10.1021/ja506433k>.
- [90] R. Mechiakh, R. Gheriani, R. Chtourou, Preparation of nanocrystalline titanium dioxide (TiO₂) thin films by the sol-gel dip coating method, *J. Nano Res.* 16 (2012) 105–111. <https://doi.org/10.4028/www.scientific.net/JNanoR.16.105>.
- [91] B. Prasai, B. Cai, M.K. Underwood, J.P. Lewis, D.A. Drabold, Properties of amorphous and crystalline titanium dioxide from first principles, *J. Mater. Sci.* 47 (2012) 7515–7521. <https://doi.org/10.1007/s10853-012-6439-6>.
- [92] P. Jane Huang, H. Chang, C. Tih Yeh, C. Wen Tsai, Transformation of TiO₂ monitored by Thermo-Raman spectroscopy with TGA/DTA, *Thermochimica Acta.* 297 (1997) 85–92.
- [93] A. Niilisk, M. Moppel, M. Pärs, I. Sildos, T. Jantson, T. Avarmaa, R. Jaaniso, J. Aarik, Structural study of TiO₂ thin films by micro-Raman spectroscopy, *Cent. Eur. J. Phys.* 4 (2006) 105–116. <https://doi.org/10.1007/s11534-005-0009-3>.
- [94] A. Ennaoui, B.R. Sankapal, V. Skryshevsky, M.C. Lux-Steiner, TiO₂ and TiO₂-SiO₂ thin films and powders by one-step soft-solution method: Synthesis and characterizations, *Sol. Energy Mater. Sol. Cells.* 90 (2006) 1533–1541. <https://doi.org/10.1016/j.solmat.2005.10.019>.
- [95] J. Guo, D. Benz, T.T. Doan Nguyen, P.H. Nguyen, T.L. Thi Le, H.H. Nguyen, D. La Zara, B. Liang, H.T. (Bert. Hintzen, J.R. van Ommen, H. Van Bui, Tuning the photocatalytic activity of TiO₂ nanoparticles by ultrathin SiO₂ films grown by low-temperature atmospheric pressure atomic layer deposition, *Appl. Surf. Sci.* 530 (2020). <https://doi.org/10.1016/j.apsusc.2020.147244>.
- [96] B.S. Avinash, V.S. Chaturmukha, H.S. Jayanna, C.S. Naveen, M.P. Rajeeva, B.M. Harish, S. Suresh, A.R. Lamani, Effect of particle size on band gap and DC electrical conductivity of TiO₂ nanomaterial, *AIP Conf. Proc.* 1728 (2016). <https://doi.org/10.1063/1.4946477>.
- [97] L. Feng, H. Yang, F. Wang, Experimental and theoretical studies for corrosion

- inhibition of carbon steel by imidazoline derivative in 5% NaCl saturated Ca(OH)₂ solution, *Electrochim. Acta.* 58 (2011) 427–436.
<https://doi.org/10.1016/j.electacta.2011.09.063>.
- [98] G. Bahlakeh, B. Ramezanzadeh, A Detailed Molecular Dynamics Simulation and Experimental Investigation on the Interfacial Bonding Mechanism of an Epoxy Adhesive on Carbon Steel Sheets Decorated with a Novel Cerium-Lanthanum Nanofilm, *ACS Appl. Mater. Interfaces.* 9 (2017) 17536–17551.
<https://doi.org/10.1021/acsami.7b00644>.
- [99] N.A. Wazzan, I.B. Obot, S. Kaya, Theoretical modeling and molecular level insights into the corrosion inhibition activity of 2-amino-1,3,4-thiadiazole and its 5-alkyl derivatives, *J. Mol. Liq.* 221 (2016) 579–602.
<https://doi.org/10.1016/j.molliq.2016.06.011>.
- [100] Y. Shiraishi, N. Saito, T. Hirai, Adsorption-driven photocatalytic activity of mesoporous titanium dioxide, *J. Am. Chem. Soc.* 127 (2005) 12820–12822.
<https://doi.org/10.1021/ja053265s>.
- [101] H. Abdullah, M.M.R. Khan, H.R. Ong, Z. Yaakob, Modified TiO₂ photocatalyst for CO₂ photocatalytic reduction: An overview, *J. CO₂ Util.* 22 (2017) 15–32. <https://doi.org/10.1016/j.jcou.2017.08.004>.
- [102] A. Chaouiki, M. Chafiq, M. Rbaa, H. Lgaz, R. Salghi, B. Lakhrissi, I.H. Ali, S. Masroor, Y. Cho, New 8-Hydroxyquinoline-Bearing Quinoxaline Derivatives as Effective Corrosion Inhibitors for Mild Steel in HCl: Electrochemical and Computational Investigations, *Coatings.* 10 (2020) 811.
<https://doi.org/10.3390/coatings10090811>.
- [103] Q. Guo, D. Huang, X. Kou, W. Cao, L. Li, L. Ge, J. Li, Synthesis of disperse amorphous SiO₂ nanoparticles via sol–gel process, *Ceram. Int.* 43 (2017) 192–196. <https://doi.org/10.1016/j.ceramint.2016.09.133>.
- [104] L. Yue, R. Cheng, W. Ding, J. Shao, J. Li, J. Lyu, Compositing micropores constructed by amorphous TiO₂ and graphene for degrading volatile organic compounds, *Appl. Surf. Sci.* 471 (2019) 1–7.
<https://doi.org/10.1016/j.apsusc.2018.11.232>.
- [105] A.M. Pennington, A.I. Okonmah, D.T. Munoz, G. Tsilomelekis, F.E. Celik, Changes in Polymorph Composition in P25-TiO₂ during Pretreatment Analyzed by Differential Diffuse Reflectance Spectral Analysis, *J. Phys. Chem. C.* 122 (2018) 5093–5104. <https://doi.org/10.1021/acs.jpcc.7b10449>.
- [106] E. Han, K. Vijayarangamuthu, J. sang Youn, Y.K. Park, S.C. Jung, K.J. Jeon, Degussa P25 TiO₂ modified with H₂O₂ under microwave treatment to enhance

- photocatalytic properties, *Catal. Today*. 303 (2018) 305–312.
<https://doi.org/10.1016/j.cattod.2017.08.057>.
- [107] N.R.C. Fernandes MacHado, V.S. Santana, Influence of thermal treatment on the structure and photocatalytic activity of TiO₂ P25, *Catal. Today*. 107–108 (2005) 595–601. <https://doi.org/10.1016/j.cattod.2005.07.022>.
- [108] M.K. Hossain, A.A. Mortuza, S.K. Sen, M.K. Basher, M.W. Ashraf, S. Tayyaba, M.N.H. Mia, M.J. Uddin, A comparative study on the influence of pure anatase and Degussa-P25 TiO₂ nanomaterials on the structural and optical properties of dye sensitized solar cell (DSSC) photoanode, *Optik (Stuttg)*. 171 (2018) 507–516. <https://doi.org/10.1016/j.ijleo.2018.05.032>.
- [109] D.M. Tobaldi, R.C. Pullar, M.P. Seabra, J.A. Labrincha, Fully quantitative X-ray characterisation of Evonik Aeroxide TiO₂ P25[®], *Mater. Lett.* 122 (2014) 345–347. <https://doi.org/10.1016/j.matlet.2014.02.055>.
- [110] H. Shin, S.G. Kim, J.S. Park, H.S. Jung, K.S. Hong, H. Kim, Role of submicron residual fillers in improving optical reflectance of barrier rib glasses for plasma display panels, *J. Mater. Res.* 21 (2006) 1753–1758.
<https://doi.org/10.1557/jmr.2006.0205>.
- [111] A. Adamczyk, E. Długoń, The FTIR studies of gels and thin films of Al₂O₃-TiO₂ and Al₂O₃-TiO₂-SiO₂ systems, *Spectrochim. Acta - Part A Mol. Biomol. Spectrosc.* 89 (2012) 11–17. <https://doi.org/10.1016/j.saa.2011.12.018>.
- [112] S. Islam, N. Bidin, S. Riaz, S. Naseem, F.M. Marsin, Correlation between structural and optical properties of surfactant assisted sol-gel based mesoporous SiO₂-TiO₂ hybrid nanoparticles for pH sensing/optochemical sensor, *Sensors Actuators, B Chem.* 225 (2016) 66–73.
<https://doi.org/10.1016/j.snb.2015.11.016>.
- [113] J. Zou, J. Gao, H₂O₂-sensitized TiO₂/SiO₂ composites with high photocatalytic activity under visible irradiation, *J. Hazard. Mater.* 185 (2011) 710–716.
<https://doi.org/10.1016/j.jhazmat.2010.09.077>.
- [114] B. Mazinani, A.K. Masrom, A. Beitollahi, R. Luque, Photocatalytic activity, surface area and phase modification of mesoporous SiO₂-TiO₂ prepared by a one-step hydrothermal procedure, *Ceram. Int.* 40 (2014) 11525–11532.
<https://doi.org/10.1016/j.ceramint.2014.03.071>.
- [115] L.L. Yang, Y.S. Lai, J.S. Chen, P.H. Tsai, C.L. Chen, C.J. Chang, Compositional tailored sol-gel SiO₂-TiO₂ thin films: Crystallization, chemical bonding configuration, and optical properties, *J. Mater. Res.* 20 (2005) 3141–3149. <https://doi.org/10.1557/JMR.2005.0393>.

- [116] Z.Y. Shen, L.Y. Li, Y. Li, C.C. Wang, Fabrication of hydroxyl group modified monodispersed hybrid silica particles and the h-SiO₂/TiO₂ core/shell microspheres as high performance photocatalyst for dye degradation, *J. Colloid Interface Sci.* 354 (2011) 196–201. <https://doi.org/10.1016/j.jcis.2010.10.023>.
- [117] J.F. Guayaquil-Sosa, B. Serrano-Rosales, P.J. Valadés-Pelayo, H. de Lasa, Photocatalytic hydrogen production using mesoporous TiO₂ doped with Pt, *Appl. Catal. B Environ.* 211 (2017) 337–348. <https://doi.org/10.1016/j.apcatb.2017.04.029>.
- [118] S. Niu, S. Li, Y. Du, X. Han, P. Xu, How to Reliably Report the Overpotential of an Electrocatalyst, *ACS Energy Lett.* 5 (2020) 1083–1087. <https://doi.org/10.1021/acseenergylett.0c00321>.
- [119] R. Naeem, M.A. Ehsan, A. Rehman, Z.H. Yamani, A.S. Hakeem, M. Mazhar, Single step aerosol assisted chemical vapor deposition of p-n Sn(II) oxide-Ti(IV) oxide nanocomposite thin film electrodes for investigation of photoelectrochemical properties, *New J. Chem.* 42 (2018) 5256–5266. <https://doi.org/10.1039/c7nj04606e>.
- [120] S. Guo, H. Zhang, Y. Chen, Z. Liu, B. Yu, Y. Zhao, Z. Yang, B. Han, Z. Liu, Visible-Light-Driven Photoreduction of CO₂ to CH₄ over N,O,P-Containing Covalent Organic Polymer Submicrospheres, *ACS Catal.* 8 (2018) 4576–4581. <https://doi.org/10.1021/acscatal.8b00989>.
- [121] Y. Li, H. Zhang, Z. Guo, J. Han, X. Zhao, Q. Zhao, S.J. Kim, Highly efficient visible-light-induced photocatalytic activity of nanostructured AgI/TiO₂ photocatalyst, *Langmuir.* 24 (2008) 8351–8357. <https://doi.org/10.1021/la801046u>.
- [122] P. Babu, B. Naik, Cu-Ag Bimetal Alloy Decorated SiO₂@TiO₂ Hybrid Photocatalyst for Enhanced H₂ Evolution and Phenol Oxidation under Visible Light, *Inorg. Chem.* 59 (2020) 10824–10834. <https://doi.org/10.1021/acs.inorgchem.0c01325>.
- [123] D. Lincot, J. Vedel, Recombination and charge transfer at the illuminated n-CdTe/electrolyte interface. Simplified kinetic model, *J. Electroanal. Chem.* 220 (1987) 179–200. [https://doi.org/10.1016/0022-0728\(87\)85107-0](https://doi.org/10.1016/0022-0728(87)85107-0).
- [124] P. Allongue, H. Cachet, Band-Edge Shift and Surface Charges at Illuminated n-GaAs/Aqueous Electrolyte Junctions: Surface-State Analysis and Simulation of Their Occupation Rate, *J. Electrochem. Soc.* 132 (1985) 45–52. <https://doi.org/10.1149/1.2113788>.
- [125] M. Umer, M. Tahir, M.U. Azam, B. Tahir, M. Musaab, Self-doped Ti³⁺

- mediated TiO₂/In₂O₃/SWCNTs heterojunction composite under acidic/basic heat medium for boosting visible light induced H₂ evolution, *Int. J. Hydrogen Energy*. 44 (2019) 13466–13479.
<https://doi.org/10.1016/j.ijhydene.2019.04.020>.
- [126] J. Mu, B. Chen, M. Zhang, Z. Guo, P. Zhang, Z. Zhang, Y. Sun, C. Shao, Y. Liu, Enhancement of the visible-light photocatalytic activity of In₂O₃-TiO₂ nanofiber heteroarchitectures, *ACS Appl. Mater. Interfaces*. 4 (2012) 424–430.
<https://doi.org/10.1021/am201499r>.
- [127] L.H. Nie, C. Shi, Y. Xu, Q.H. Wu, A.M. Zhu, Atmospheric cold plasmas for synthesizing nanocrystalline anatase TiO₂ using dielectric barrier discharges, *Plasma Process. Polym.* 4 (2007) 574–582.
<https://doi.org/10.1002/ppap.200600212>.
- [128] A. Ajmal, I. Majeed, R.N. Malik, M. Iqbal, M.A. Nadeem, I. Hussain, S. Yousuf, Zeshan, G. Mustafa, M.I. Zafar, M.A. Nadeem, Photocatalytic degradation of textile dyes on Cu₂O-CuO/TiO₂ anatase powders, *J. Environ. Chem. Eng.* 4 (2016) 2138–2146. <https://doi.org/10.1016/j.jece.2016.03.041>.
- [129] G. Xie, L. Wang, Q. Zhu, L. Xu, K. Song, Z. Yu, Modification of SiO₂ Nanoparticle-Decorated TiO₂ Nanocomposites with Silane Coupling Agents for Enhanced Opacity in Blue Light-Curable Ink, *ACS Appl. Nano Mater.* 5 (2022) 9678–9687. <https://doi.org/10.1021/acsnm.2c01910>.
- [130] B.M. Reddy, I. Ganesh, E.P. Reddy, Study of dispersion and thermal stability of V₂O₅/TiO₂-SiO₂ catalysts by XPS and other techniques, *J. Phys. Chem. B*. 101 (1997) 1769–1774. <https://doi.org/10.1021/jp963091o>.
- [131] P. Ondračka, D. Nečas, M. Carette, S. Elisabeth, D. Holec, A. Granier, A. Goulet, L. Zajíčková, M. Richard-Plouet, Unravelling local environments in mixed TiO₂-SiO₂ thin films by XPS and ab initio calculations, *Appl. Surf. Sci.* 510 (2020). <https://doi.org/10.1016/j.apsusc.2019.145056>.
- [132] M. Hu, Z. Xing, Y. Cao, Z. Li, X. Yan, Z. Xiu, T. Zhao, S. Yang, W. Zhou, Ti³⁺ self-doped mesoporous black TiO₂/SiO₂/g-C₃N₄ sheets heterojunctions as remarkable visible-lightdriven photocatalysts, *Appl. Catal. B Environ.* 226 (2018) 499–508. <https://doi.org/10.1016/j.apcatb.2017.12.069>.
- [133] J. Cañón, A. V. Teplyakov, XPS characterization of cobalt impregnated SiO₂ and γ-Al₂O₃, *Surf. Interface Anal.* 53 (2021) 475–481.
<https://doi.org/10.1002/sia.6935>.
- [134] R. Matsumoto, Y. Nishizawa, N. Kataoka, H. Tanaka, H. Yoshikawa, S. Tanuma, K. Yoshihara, Reproducibility of XPS analysis for film thickness of

- SiO₂/Si by active Shirley method, *J. Electron Spectros. Relat. Phenomena*. 207 (2016) 55–59. <https://doi.org/10.1016/j.elspec.2015.12.008>.
- [135] R. Sarhaddi, N. Shahtahmasebi, M. Rezaee Rokn-Abadi, M.M. Bagheri-Mohagheghi, Effect of post-annealing temperature on nano-structure and energy band gap of indium tin oxide (ITO) nano-particles synthesized by polymerizing complexing sol-gel method, *Phys. E Low-Dimensional Syst. Nanostructures*. 43 (2010) 452–457. <https://doi.org/10.1016/j.physe.2010.08.028>.
- [136] H. Han, J.W. Mayer, T.L. Alford, Band gap shift in the indium-tin-oxide films on polyethylene naphthalate after thermal annealing in air, *J. Appl. Phys.* 100 (2006) 083715. <https://doi.org/10.1063/1.2357647>.
- [137] S.H. Brewer, S. Franzen, Calculation of the electronic and optical properties of indium tin oxide by density functional theory, *Chem. Phys.* 300 (2004) 285–293. <https://doi.org/10.1016/j.chemphys.2003.11.039>.
- [138] S. Li, X. Qiao, J. Chen, Effects of oxygen flow on the properties of indium tin oxide films, *Mater. Chem. Phys.* 98 (2006) 144–147. <https://doi.org/10.1016/j.matchemphys.2005.09.012>.
- [139] C.H.L. Weijtens, P.A.C. Van Loon, Influence of annealing on the optical properties of indium tin oxide, *Thin Solid Films*. 196 (1991) 1–10. [https://doi.org/10.1016/0040-6090\(91\)90169-X](https://doi.org/10.1016/0040-6090(91)90169-X).
- [140] K.K. Ghuman, L.B. Hoch, P. Szymanski, J.Y.Y. Loh, N.P. Kherani, M.A. El-Sayed, G.A. Ozin, C.V. Singh, Photoexcited Surface Frustrated Lewis Pairs for Heterogeneous Photocatalytic CO₂ Reduction, *J. Am. Chem. Soc.* 138 (2016) 1206–1214. <https://doi.org/10.1021/jacs.5b10179>.
- [141] T. Yan, N. Li, L. Wang, W. Ran, P.N. Duchesne, L. Wan, N.T. Nguyen, L. Wang, M. Xia, G.A. Ozin, Bismuth atom tailoring of indium oxide surface frustrated Lewis pairs boosts heterogeneous CO₂ photocatalytic hydrogenation, *Nat. Commun.* 11 (2020) 6095. <https://doi.org/10.1038/s41467-020-19997-y>.
- [142] H. Zhang, Y. Han, L. Yang, X. Guo, H. Wu, N. Mao, Photocatalytic Activities of PET Filaments Deposited with N-Doped TiO₂ Nanoparticles Sensitized with Disperse Blue Dyes, *Catalysts*. 10 (2020) 531. <https://doi.org/10.3390/catal10050531>.
- [143] H. Bin Zhang, W.G. Zheng, Q. Yan, Y. Yang, J.W. Wang, Z.H. Lu, G.Y. Ji, Z.Z. Yu, Electrically conductive polyethylene terephthalate/graphene nanocomposites prepared by melt compounding, *Polymer (Guildf)*. 51 (2010) 1191–1196. <https://doi.org/10.1016/j.polymer.2010.01.027>.

- [144] M. Tahir, B. Tahir, N.A. Saidina Amin, H. Alias, Selective photocatalytic reduction of CO₂ by H₂O/H₂ to CH₄ and CH₃OH over Cu-promoted In₂O₃/TiO₂ nanocatalyst, *Appl. Surf. Sci.* 389 (2016) 46–55.
<https://doi.org/10.1016/j.apsusc.2016.06.155>.
- [145] J. Ran, M. Jaroniec, S.Z. Qiao, Cocatalysts in Semiconductor-based Photocatalytic CO₂ Reduction: Achievements, Challenges, and Opportunities, *Adv. Mater.* 30 (2018) 1–31. <https://doi.org/10.1002/adma.201704649>.
- [146] P. Devi, J.P. Singh, Visible light induced selective photocatalytic reduction of CO₂ to CH₄ on In₂O₃-rGO nanocomposites, *J. CO₂ Util.* 43 (2021) 101376.
<https://doi.org/10.1016/j.jcou.2020.101376>.
- [147] D. Friedmann, R.A. Caruso, Indium Oxides and Related Indium-based Photocatalysts for Water Treatment: Materials Studied, Photocatalytic Performance, and Special Highlights, *Sol. RRL.* 5 (2021) 1–24.
<https://doi.org/10.1002/solr.202100086>.
- [148] X. Jin, Q. Guan, T. Tian, H. Li, Y. Han, F. Hao, Y. Cui, W. Li, Y. Zhu, Y. Zhang, In₂O₃/boron doped g-C₃N₄ heterojunction catalysts with remarkably enhanced visible-light photocatalytic efficiencies, *Appl. Surf. Sci.* 504 (2020) 144241. <https://doi.org/10.1016/j.apsusc.2019.144241>.
- [149] K. Choi, J. Jeong, J. Kang, D. Kim, J. Kuk, S. Na, D. Kim, S. Kim, H. Kim, Solar Energy Materials & Solar Cells Characteristics of flexible indium tin oxide electrode grown by continuous roll-to-roll sputtering process for flexible organic solar cells, *Sol. Energy Mater. Sol. Cells.* 93 (2009) 1248–1255.
<https://doi.org/10.1016/j.solmat.2009.01.015>.
- [150] J. Lee, H. Jung, J. Lee, D. Lim, K. Yang, J. Yi, W. Song, Growth and characterization of indium tin oxide thin films deposited on PET substrates, *Thin Solid Films.* 516 (2008) 1634–1639.
<https://doi.org/10.1016/j.tsf.2007.05.028>.
- [151] J.Y.Y. Loh, A. Mohan, A.G. Flood, G.A. Ozin, N.P. Kherani, Waveguide photoreactor enhances solar fuels photon utilization towards maximal optoelectronic – photocatalytic synergy, *Nat. Commun.* 12 (2021) 1–11.
<https://doi.org/10.1038/s41467-020-20613-2>.
- [152] Y. Zhihong, L. Yuqiong, X. Fan, Z. Zhiwei, X. Wei, Properties of indium tin oxide films deposited on unheated polymer substrates by ion beam assisted deposition, *Thin Solid Films.* 517 (2009) 5395–5398.
<https://doi.org/10.1016/j.tsf.2008.12.057>.
- [153] K. Wan, D. Wang, F. Wang, H. Li, J. Xu, X. Wang, J. Yang, Hierarchical

In₂O₃@SnO₂ Core-Shell Nanofiber for High Efficiency Formaldehyde Detection, *ACS Appl. Mater. Interfaces*. 11 (2019) 45214–45225. <https://doi.org/10.1021/acsami.9b16599>.

- [154] K.P. Sibin, N. Swain, P. Chowdhury, A. Dey, N. Sridhara, H.D. Shashikala, A.K. Sharma, H.C. Barshilia, Optical and electrical properties of ITO thin films sputtered on flexible FEP substrate as passive thermal control system for space applications, *Sol. Energy Mater. Sol. Cells*. 145 (2016) 314–322. <https://doi.org/10.1016/j.solmat.2015.10.035>.
- [155] M.J. Alam, D.C. Cameron, Optical and electrical properties of transparent conductive ITO thin films deposited by sol-gel process, *Thin Solid Films*. 377–378 (2000) 455–459. [https://doi.org/10.1016/S0040-6090\(00\)01369-9](https://doi.org/10.1016/S0040-6090(00)01369-9).
- [156] S. Marikkannu, C. Sanjeeviraja, S. Piraman, A. Ayeshamariam, Studies on the structural, optical, and electrical properties of jet-nebulized spray pyrolysis ITO thin films, *J. Mater. Sci. Mater. Electron*. 26 (2015) 2531–2537. <https://doi.org/10.1007/s10854-015-2718-8>.
- [157] N. Rui, Z. Wang, K. Sun, J. Ye, Q. Ge, C. jun Liu, CO₂ hydrogenation to methanol over Pd/In₂O₃: effects of Pd and oxygen vacancy, *Appl. Catal. B Environ*. 218 (2017) 488–497. <https://doi.org/10.1016/j.apcatb.2017.06.069>.
- [158] M.H. Ahn, E.S. Cho, S.J. Kwon, Effect of the duty ratio on the indium tin oxide (ITO) film deposited by in-line pulsed DC magnetron sputtering method for resistive touch panel, *Appl. Surf. Sci*. 258 (2011) 1242–1248. <https://doi.org/10.1016/j.apsusc.2011.09.081>.
- [159] Y. Bao, S. Song, G. Yao, S. Jiang, S-Scheme Photocatalytic Systems, *Sol. RRL*. 5 (2021) 1–13. <https://doi.org/10.1002/solr.202100118>.
- [160] J. Low, B. Dai, T. Tong, C. Jiang, J. Yu, In Situ Irradiated X-Ray Photoelectron Spectroscopy Investigation on a Direct Z-Scheme TiO₂/CdS Composite Film Photocatalyst, *Adv. Mater*. 31 (2019) 1–5. <https://doi.org/10.1002/adma.201802981>.

VITA

NAME Mohammad Fereidooni

DATE OF BIRTH 10 May 1991

PLACE OF BIRTH Fasa, Iran

HOME ADDRESS Room 513, 5th floor, The Cosy River residence, Soi 17, Charoen Nakhon Rd., Banglumpoolang, Khlongsan, Bangkok 10600

PUBLICATION M. Fereidooni, O. Núñez, V. Márquez, C.V. Paz, M. Salazar Villanueva, M. Zin Tun, P. Kanjanaboos, S. Praserthdam, P. Praserthdam, Effect of substrate conductivity on charge transfer and CO₂ photoreduction in water vapor over silica-modified TiO₂ films, Appl. Surf. Sci. (2022) 155595.
<https://doi.org/10.1016/j.apsusc.2022.155595>.

C.V. Paz, M. Fereidooni, P. Praserthdam, A.A. Santiago, S. Praserthdam, V. Marquez, Toward the understanding of surface phenomena involved in the photocatalytic performance of amorphous TiO₂/SiO₂ catalyst – A theoretical and experimental study, Appl. Surf. Sci. 588 (2022) 152920.
<https://doi.org/10.1016/j.apsusc.2022.152920>.